UNIVERSITY OF OKLAHOMA

GRADUATE COLLEGE

EEG/MEG SPARSE SOURCE IMAGING AND ITS APPLICATION IN EPILEPSY

A DISSERTATION

SUBMITTED TO THE GRADUATE FACULTY

in partial fulfillment of the requirements for the

Degree of

DOCTOR OF PHILOSOPHY

By

MIN ZHU
Norman, Oklahoma
2013

EEG/MEG SPARSE SOURCE IMAGING AND ITS APPLICATION IN EPILEPSY

A DISSERTATION APPROVED FOR THE
SCHOOL OF ELECTRICAL AND COMPUTER ENGINEERING

BY

_____
Dr. Lei Ding, Chair

_____
Dr. Meijun Zhu

_____
Dr. Andrew Fagg

_____
Dr. Joseph Havlicek

_____
Dr. Hong Liu

Acknowledgements

First and foremost, I would like to thank my advisor, Dr. Lei Ding, for his mentoring and caring over the past five and half years. Without his guidance, I would never achieve this. He is not only a mentor guiding me to this field, but also a friend to give me kind advices on my academic and career development.

I would also like to express my gratitude to all other committee members, Dr. Joseph Havlicek, Dr. Hong Liu, Dr. Andrew Fagg and Dr. Meijun Zhu, who have provided me with constructive suggestions on my research. I really appreciate Dr. Fagg and Dr. Havlicek for taking time and efforts in revising my dissertation to make it more readable.

Moreover, I would like to thank all my lab mates, Dr. Guofa Shou, Deepika Dasari, Ran Xiao, as well as Dr. Ke Liao and Jania Gonzalez. I really enjoyed working with them and had a great time. Special thanks go to my beloved fiancé, Ran Xiao. Together, we have been through thick and thin, and he is always there for me.

Finally, I would like to thank all my friends and my family for their undying supports, especially to my parents, Miaozheng Zhu and Ruqin Huang, as well as my host family in the U.S., Heidi James.

Table of Contents

Acknowledgements iv

List of Tables viii

List of Figures ix

Abstract xi

Chapter 1: Contributions and Outlines 1

Chapter 2: Background 7

2.1 Introduction to EEG/MEG 8

2.1.1 Genesis of EEG/MEG 8

2.1.2 Measuring of EEG/MEG 10

2.2 EEG/MEG Source Model 13

2.2.1 Equivalent Current Dipole Model 13

2.2.2 Distributed Current Density Model 14

2.3 Volume Conductor Model 16

2.4 The Forward and Inverse Problems 18

2.5 Regularizations 19

Chapter 3: Variation Based Sparse Source Imaging 23

3.1 Variation Based Sparse Source Imaging Method 24

3.2 Data Acquisition and Analysis 25

3.2.1 Patients and MEG Acquisition 25

3.2.2 Source Model and Volume Conductor Model 26

3.2.3 MEG Data Analysis 26

3.2.4 Evaluation Methods 28

3.4 Source Reconstruction Results 29
3.4.1 Comparisons of MNE, SSI and V-SSI 29
3.4.2 Localization of irritative zones in individual patients 30
3.4.3 Comparison of cortical sources at peaks, rising phases and entire spikes. 36
3.4.4 Reconstruction of cortical source dynamics 37
3.4.5 Comparison of surface MEGs and cortical source maps 44
3.5 Discussion and Summary 45
Chapter 4: Wavelet Based Sparse Source Imaging 48
4.1 The Face-based Surface Wavelet 49
4.1.1 Multi-resolution Model 49
4.1.2 Face-based Wavelet Transform 51
4.1.3 Wavelet-based Sparse Source Imaging 52
4.2 Performance Analysis Using Simulated Data 53
4.2.1 Simulation Protocol 53
4.2.2 Synthesis Performance 54
4.2.3 Vertex-based vs. Face-based Wavelets 56
4.3 Performance Analysis Using Experimental Data 57
4.3.1 Language Data 57
4.3.2 Epilepsy Data 59
4.4 Discussion and Summary 63
Chapter 5: Sparse Source Imaging Using Multiple Transforms 66
5.1 Variation and Wavelet Based Sparse Source Imaging 67
5.2 Performance Analysis Using Simulated Data 68

5.2.1 Simulation Protocol 68
5.2.2 Influence of the Hyper-parameter λ 70
5.2.3 Influence of the Wavelet Compression Level 72
5.2.4 Comparisons with ℓ_2-norm regularizations 73
5.2.5 Comparisons to Other ℓ_1-norm regularizations 75
5.2.6 Effects of Source Extent 76
5.2.7 Effects of Number of Sources 78
5.2.8 Sensitivity to SNR 80
5.3 Performance Analysis Using Experimental Data 80
5.3.1 Experiment Protocol 80
5.3.2 The Language Task 82
5.3.2 The Motor Task 84
5.4 Discussion and Summary 84
Chapter 6: Discussion and Conclusion 90
6.1 Transform Sparseness 90
6.2 Single Penalty vs. Multiple Penalties 92
6.3 Recovering Sources with Extent Information 94
6.4 Applications in Epilepsy 95
6.5 Limitations and Future Work 98
6.6 Conclusion 99
References 101
Appendix A: Analysis Matrices for Face-based Wavelets 110
Appendix B: Evaluation Metrics 111

List of Tables

Table 3.1 Diagnosis and pre-surgical evaluations 27

Table 3.2 Summary of reconstruction results 32

List of Figures

Figure 2.1 Structure of a typical neuron cell 8

Figure 2.2 Illustration of cortical generators of EEG/MEG signals 9

Figure 2.3 Illustration of EEG sensor layouts and recordings 11

Figure 2.4 Illustration of MEG sensors and recording environment 12

Figure 2.5 Illustration of CCD source model. 15

Figure 2.6 Illustration of BE volume conductor model 18

Figure 3.1 Comparison of MNE, SSI and V-SSI 30

Figure 3.2 Comparison of V-SSI sources and MRI lesions in Patient 1 31

Figure 3.3 Comparison of V-SSI sources, MRI lesions, and post-surgical MRI in Patient 2 33

Figure 3.4 Cortical sources from V-SSI in Patient 3 35

Figure 3.5 Patient 1: an example of stable cortical sources 37

Figure 3.6 Patient 1: an example of local propagation within temporal lobe 38

Figure 3.7 Patient 2: an example of propagation within the same hemisphere 39

Figure 3.8 Patient 3: an example of in-hemisphere propagation 41

Figure 3.9 Patient 3: an example of slow cross-hemisphere propagation 42

Figure 3.10 Patient 3: An example of fast cross-hemisphere propagation 43

Figure 3.11 Comparison of magnetic fields and V-SSI sources 44

Figure 4.1 One example of a multi-resolution model 50

Figure 4.2 Synthetic performance of the face-based wavelet analysis 55

Figure 4.3 Inverse performances of face-based and vertex-based wavelet methods 56

Figure 4.4 Comparison of face-based and vertex-based wavelet methods in language data 58

Figure 4.5 Reconstructed epileptic sources in Patient 1 60

Figure 4.6 Reconstructed epileptic sources in Patient 4 61

Figure 4.7 Reconstructed epileptic sources in Patient 3 62

Figure 5.1 Sensitivity of VW-SSI to the hyper-parameter λ. 71

Figure 5.2 Sensitivity of VW-SSI and W-SSI to wavelet compression levels. 73

Figure 5.3 Comparison of VW-SSI to ℓ_2-norm regularizations 74

Figure 5.4 Comparison of VW-SSI to other ℓ_1-norm regularizations 76

Figure 5.5 Performances with various source extents 77

Figure 5.6 Performance with different numbers of sources 79

Figure 5.7 Performances at different SNR levels 81

Figure 5.8 Estimated sources in a language task 83

Figure 5.9 Estimated sources in a motor task 85

Abstract

This dissertation is a summary of my Ph.D. work on the development of sparse source imaging technologies based on electroencephalography (EEG) and magneto-encephalography (MEG) and their application to noninvasively reconstruct brain activation from external surface measurements. Conventional sparse source imaging (SSI) methods using the ℓ_1-norm regularization to enforce sparseness in the original source domain leads to over-focused solutions and causes bias in estimating spatially extended brain sources. I address the over-focused issue in the ℓ_1-norm regularization technique framework by exploring sparseness in the transform domains. First, I apply a SSI method that uses the variation transform, i.e. V-SSI, on clinical MEG interictal recordings from partial epilepsy patients. Estimated epileptic sources by V-SSI are validated using clinical pre-surgical evaluation data and surgical outcomes. Second, I implement a novel face-based wavelet transform, which can efficiently compress brain activation signals into sparse representations on a multi-resolution cortical source model, into the SSI technology framework. The proposed wavelet-based SSI (W-SSI) demonstrates a significantly improved ability in inferring both brain source locations and extents as compared with conventional ℓ_2-norm regularizations in obtaining EEG/MEG inverse solutions and other SSI technologies. Furthermore, the face-based wavelet also indicates better performance than a previously reported vertex-based wavelet in W-SSI. I evaluate the W-SSI method and conduct the comparison studies using both simulations and real data collected from partial epilepsy patients. Lastly, I further propose the concept of using multiple transforms in the SSI technology framework and investigated a new SSI method by enforcing sparseness in both variation

and face-based wavelet domains, termed as VW-SSI. I conduct simulation studies, which demonstrate that VW-SSI has significantly better detection accuracies in both source locations and extents than conventional ℓ_2-norm regularizations and other SSI methods, including SSI, V-SSI, and W-SSI. I further validate the VW-SSI method using clinical MEG data from both language and motor experiments collected from epilepsy patients again to localize their important functional brain areas. The results indicate that VW-SSI provides a performance advantage in detecting neural phenomena that have been extremely difficult to recognize by other EEG/MEG inverse solutions. It thus suggests that the sparse source imaging technique is promising to serve as a non-invasive tool in assisting pre-surgical planning for partial epilepsy patients.

Chapter 1: Contributions and Outlines

The motivation for this dissertation is to assist the pre-surgical evaluation of epilepsy patients who are receiving surgical treatment. Around 50 million people worldwide suffer from epilepsy and about 30% among them are resistant to medication (World Health Organization, 2012). For those medically refractory epilepsy patients, surgical resection of epileptogenic zone (EZ) with brain tissues generating epileptic activity is an efficient treatment with minimum reoccurrences (Engel, 1993; Wiebe, et al., 2001; Spencer and Huh, 2008). An accurate estimation of the location and extent of the EZ is thus essential for a successful surgical treatment. In clinical practice, the "gold standard" in defining EZs for resection is electrocorticography (ECoG), which is an invasive technology with electrodes directly placed on the exposed surface of the human brain (Kuruvilla and Flink, 2003; Asano et al., 2009). However, ECoG is expensive and high-risk due to its invasiveness, limiting the number of candidates to receive the surgical treatment. Noninvasive electromagnetic measurements from scalp sensors, such as electroencephalography (EEG) and magnetoencephalography (MEG), are promising alternatives to localize EZs for surgery. Unfortunately, the spatial resolution of surface EEG and MEG is relatively low due to the limited number of sensors and the volume conduction effect (van den Broek et al., 1998). The source imaging technique has evolved in the last decades in order to improve the spatial resolution of EEG/MEG by inversely mapping surface measurements to their electrical origins in the cerebral cortex (Dale and Sereno, 1993; Hämäläinen and Ilmoniemi, 1994; Pascual-Marqui et al., 1994; Matsuura and Okabe, 1995; Tibshirani, 1996; Uutela et al., 1999; Darvas et al., 2004). Conventional source imaging methods based on ℓ_2-

norm regularization (Dale and Sereno, 1993; Hämäläinen and Ilmoniemi, 1994; Pascual-Marqui et al., 1994) or ℓ_1-norm regularization (Matsuura and Okabe, 1995; Tibshirani, 1996; Uutela et al., 1999) usually result in biases in estimating the source extent with either over-smoothed or over-focused distributions, which motivates me to develop a new source imaging approach with more accurate estimations for both source location and extent.

The primary contribution of this dissertation is the development of a sparse source imaging framework to address the over-focality issue in the ℓ_1-norm regularization framework via enforcing sparseness in transform domains, and thus to improve the reconstruction accuracy. The framework includes the numerical modeling of the cortical source space and the volume conductor, formulating the forward problem, exploring transform domains where electrical brain activations can be sparsely represented, and solving the inverse problem using proper and efficient solvers.

Another major contribution of this dissertation is that the sparse source imaging framework is further extended to handle multiple sparse transforms simultaneously. Variation and wavelet transforms are incorporated together in the same cost function to solve the EEG/MEG inverse problem. The benefit of using multiple transforms rather than a single one is that the hybrid might keep merits from both transforms and compensate their individual weaknesses.

The final contribution is the extensive evaluations of various sparse source imaging methods that have been developed using simulations and experimental data. Monte-Carlo simulations were adopted with 200 randomly located cortical sources. Sensitivity to possible effects, such as source extent, number of sources, measurement

noise, or selection of parameters, have been investigated. Multiple assessment criteria were adopted to evaluate the reconstruction performance from different aspects. The performances of those sparse source imaging methods have also been evaluated and validated using real MEG data of interictal epileptic activities or experimental tasks from epilepsy patients. Reconstructed sources underlying epileptic interictal spikes were compared to clinical data, such as diagnosis, magnetic resonance imaging (MRI) lesions, and resection areas during surgery. Detections of well-documented neural phenomena from MEG in the language or motor task have also been used to evaluate the performance of the proposed source imaging methods.

The following are brief descriptions chapter by chapter to help readers get the general structure of the dissertation.

Chapter 2: Backgrounds

In this chapter, I prepare readers with the background knowledge to understand EEG/MEG source imaging technology. The chapter starts with descriptions of EEG and MEG's cortical origins and current measurement techniques. Different numerical models are introduced to model the electrical cortical sources and the head volume conductor. The forward and inverse equations are then formulated to mathematically explain the relationships between the cortical current sources and the EEG/MEG measurements. A regularization scheme is introduced to solve the inverse problem, and several source imaging methods based on ℓ_2-norm or ℓ_1-norm regularization are briefly reviewed.

Chapter 3: Variation Based Sparse Source Imaging

In this chapter, I introduce a sparse source imaging algorithm that utilizes the sparse transform for the first time, i.e. variation based sparse source imaging (V-SSI), and present its applications in identifying epileptic sources of interical spikes from MEG data recorded in three epilepsy patients. Although V-SSI has been previously proposed and evaluated using simulations (Ding, 2009), this algorithm is evaluated and validated in clinical epilepsy data for the first time in this dissertation. Cortical sources estimated by V-SSI from multiple interictal spikes are statistically compared to clinical validations to indicate the recovery accuracy of V-SSI. Other source imaging methods are also performed for comparison. Typical spatio-temporal patterns are reconstructed to further investigate propagations of epileptic activities.

Chapter 4: Wavelet Based Sparse Source Imaging

In this chapter, a face-based wavelet transform is proposed to provide a sparse representation of cortical activations. The compression ability of this newly designed face-based wavelet is compared to a previously reported vertex-based wavelet using simulated cortical sources. Later, the face-based wavelet is implemented in the ℓ_1-norm regularization framework that leads to the development of a novel source imaging algorithm, i.e. wavelet based sparse source imaging (W-SSI). Both simulations and experimental recordings from epilepsy patients are utilized to evaluate the performance of the proposed approach with comparison to the vertex-based wavelet method.

Chapter 5: Sparse Source Imaging Using Multiple Transforms

In this chapter, I further extend the sparse source imaging approach from using a single transform to multiple transforms. Both variation and the face-based wavelet are

integrated in the ℓ_1-norm regularization framework to develop a new sparse source imaging algorithm, i.e. variation and wavelet based sparse source imaging (VW-SSI). To balance the preference between two transforms, a hyper-parameter is introduced. The proposed algorithm aims to improve the performance of the sparse source imaging technique by combining both advantages from variation and wavelet based methods and neutralizing their disadvantages at the same time. The performance of VW-SSI is evaluated using both simulations and real data from experimental recordings. The sensitivities of the proposed method to source configurations (e.g. source extent and number of sources) and parameter changes (e.g. the hyper-parameter, wavelet compression level) are investigated in simulations. VW-SSI is also applied to experimental MEG recordings in a language task and a motor task from an epilepsy patient. Sources recovered by VW-SSI are compared to some well-studied neural phenomena supported by references. Other source imaging algorithms are also performed for the purpose of comparison, including conventional ℓ_2-norm regularizations and ℓ_1-norm regularizations without or with single transform.

Chapter 6: Discussion

In this chapter, I summarize and discuss all the proposed methods and results from different angles. The reason to pursue the transform sparseness is discussed from the theoretic viewpoint, and the benefits of using the transform sparseness are supported by simulation and experimental results on real data. The benefits of using multiple transforms are also discussed by comparing the performance of VW-SSI to other SSI methods using single transforms. The capabilities of the proposed SSI methods with sparse transforms (single or multiple) in recovering extended brain sources as well as

inferring their extents are emphasized. The feasibility of applying those proposed SSI methods to identify epileptogenic zones and eloquent cortices for epilepsy surgery is also discussed based on the results. Meanwhile, limitations of the recent works are discussed and possible future works are proposed. At the end, all the work done in this dissertation is summarized in the conclusion.

Chapter 2: Background

Electroencephalography (EEG) and magnetoencephalography (MEG) are promising noninvasive neuroimaging tools to investigate electrical brain activities with an unsurpassed temporal resolution of milliseconds. However, EEG and MEG measured on the scalp are usually smeared and of low spatial resolution, due to the volume conduction effect (van den Broek et al., 1998). By taking advantage of recent technologies, the volume conduction effect can be tackled by numerically modeling the conduction profiles of head tissues. Moreover, EEG/MEG source imaging techniques have evolved in the last decades to improve the spatial resolution of EEG/MEG by inversely mapping the sensor signals (on the scalp) to their cortical origins (on the cerebral cortex).

In this chapter, the genesis of EEG/MEG signals is first described from tiny currents generated at the cellular level to net current flows at the macro level, in order to understand the neural mechanism of EEG/MEG. Current measuring technologies for EEG and MEG, including sensors and recording instruments, are briefly reviewed to understand the physical mechanisms in measuring EEG and MEG. Mathematical models of brain sources and the volume conductor are introduced from the simplest one to the most complex one. The relationship between EEG/MEG measurements and cortical sources can be derived by solving the EEG/MEG forward problem. With this relationship, cortical sources can thus be reconstructed from EEG/EMG by solving the inverse problem. Due to its ill-posedness nature, the inverse problem does not have a unique solution. Regularization schemes based on either the ℓ_2-norm or ℓ_1-norm are thus introduced to derive a solution with physical and/or physiological meaning.

2.1 Introduction to EEG/MEG

2.1.1 Genesis of EEG/MEG

Neurons are primary components of the human brain, responsible for processing and transmitting information through electrical or chemical signals. A typical neuron cell (Figure 2.1) consists of three parts: (1) dendrites, which are tree-like receivers collecting electrical or chemical stimuli from other cells; (2) the cell body, which is the main processor for generating electrical impulses; (3) the axon, which is a long nerve fiber conducting electrical impulses away from the cell body to other cells (Hämäläinen, et al., 1993; Iaizzo, 2013).

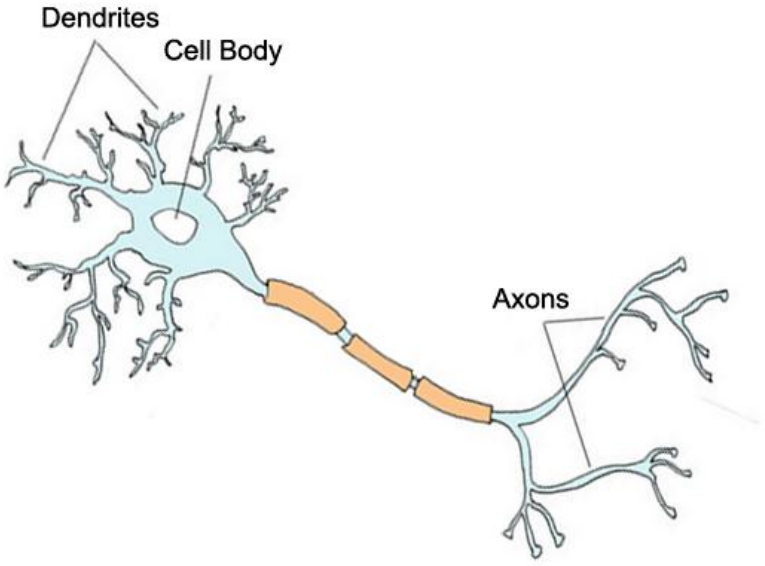

Figure 2.1 Structure of a typical neuron cell
A typical neuron cell consists of three parts, dendrites, the cell body and axons (adapted from Iaizzo, 2013, with permission).

The pyramidal cells are a principal group of cortical neurons with large apical dendrites assembled parallel along the cortical surface (Figure 2.2(a)) (Baillet et al., 2001). A pyramidal neuron is electrically excited when the apical dendritic membrane is

depolarized by stimuli from other neurons to generate excitatory postsynaptic potentials (EPSPs) (Figure 2.2(a)), and potential differences between dendrites and non-excited soma bodies consequently trigger an intracellular current flow sustaining the EPSPs. The intracellular current (also known as the primary current) imposes passive extracellular currents (also known as secondary currents) flowing in the volume conductor to form a closed current loop. Although both primary and secondary currents contribute to electrical potentials and magnetic fields measured on the scalp, the spatial organization of pyramidal cells with parallel arrangement allows the summation of currents with limited cancellations. Macro-columns of primary currents (Figure 2.2(b)) from tens of thousands of synchronously excited pyramidal cells are thus believed to be the main contributors for EEG and MEG signals. Empirical observations and invasive studies suggest that synchronously active neurons with a cortical coverage of at least $6cm^2$ are required in order to yield a net current that can be detected by EEG and MEG at the scalp (Cooper et al., 1965; Tao et al., 2005). EEG and MEG measurements are possibly originated from multiple activations from different brain areas (Figure 2.2 (c)).

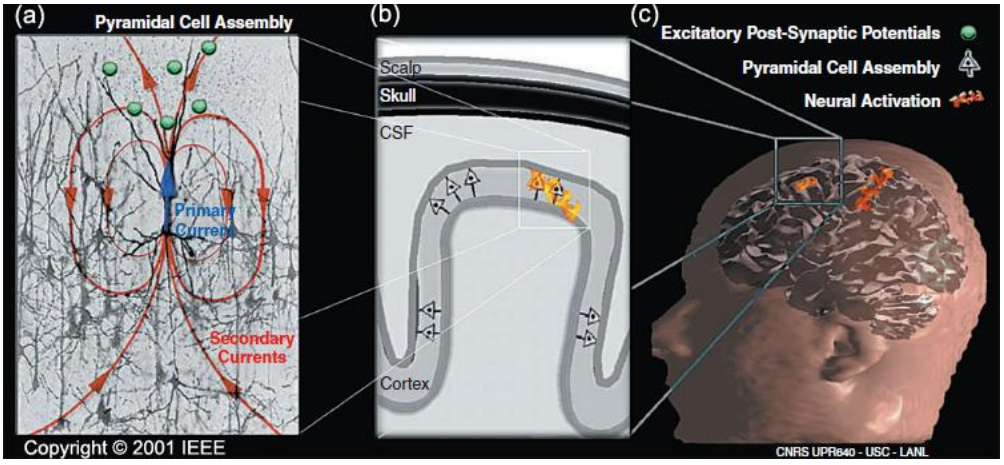

Figure 2.2 Illustration of cortical generators of EEG/MEG signals
(from Baillet et al., 2001, with permission). (a) Large pyramidal neuron cells assembly, and excited primary current and secondary currents. (b) Net currents from tens of thousands synchronously active neuron cells. (c) Networks of active cortical areas.

2.1.2 Measuring of EEG/MEG

While electrical brain activities were first observed in animals using paired electrodes placed on exposed cerebral hemispheres in 1875 (Haas, 2003), the first human brain EEG signals using noninvasive measures were not recorded until 1924 by the German physiologist Hans Berger (Haas, 2003). Although nowadays the measuring technologies of EEG have been much advanced since 1924, the physical principle is still the same. Generally speaking, EEG measures electrical potentials with electrodes placed on the scalp (Malmivuo and Plonsey, 1995). The placement of EEG electrodes usually follows the international 10-20 system located on the 10% and 20% intervals between two bony landmarks: nasion and inion (Figure 2.3(a)). Extra electrodes can be inserted into the half way points between 20% intervals to form an extended 10-20 system (Figure 2.3(b)). The locations and names of those electrodes have been standardized by the American Electroencephalography Society (Sharbrough et al., 1991). The number of EEG electrodes usually ranges from the tens, e.g., 21 electrodes in the international 10-20 system, to the hundreds. EEG electrodes are usually fixed on a cap or connected to each other as a net (see the sensor net in Figure 2.3(c) as an example). Liquid or gel conductive electrolyte is usually applied to electrodes before recording in order to reduce their impedances. The typical amplitude of EEG from human adults is around 10 to 200 microvolts (μV), which can be captured and digitized by the amplifier (see Figure 2.3(c) as an example). Figure 2.3(c) illustrates one EEG recording with one subject wearing a 128-channel EEG sensor net (Electrical Geodesics, Inc.).

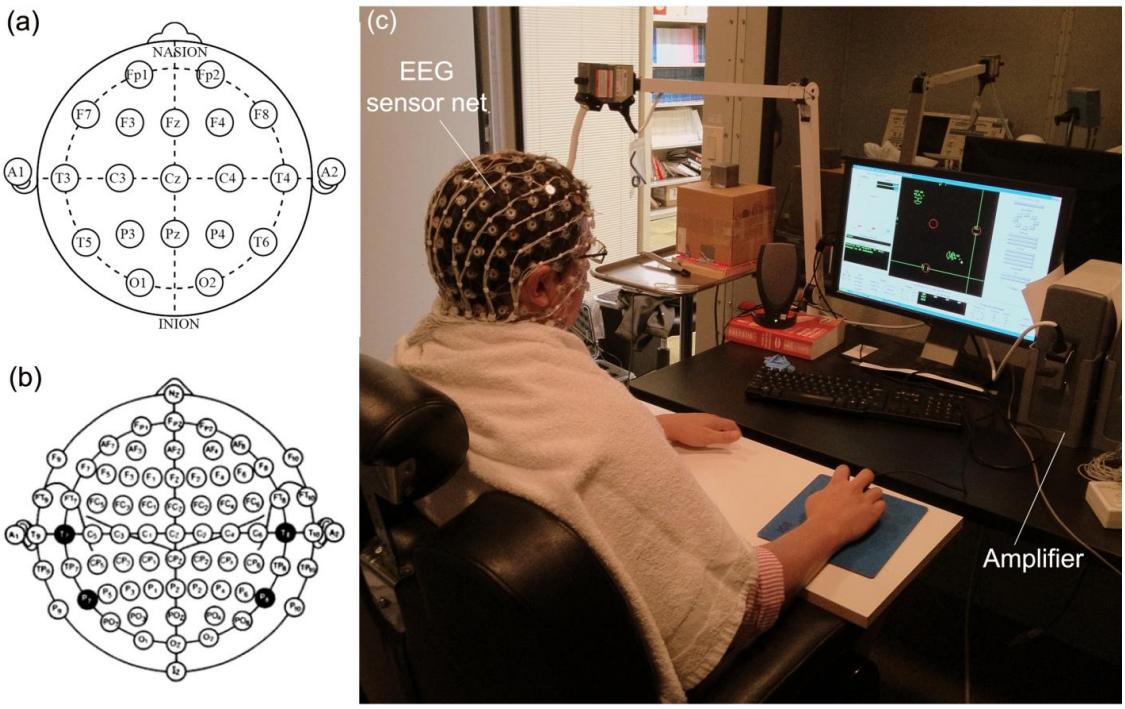

Figure 2.3 Illustration of EEG sensor layouts and recordings
(a) The international 10-20 system. A=ear lobe, F=frontal, C=central, T=temporal, P=parietal, O=occipital. (b) The extended 10-20 system (Copyright 1990 American Electroencephalography Society). (c) One subject is wearing a 128-channel EEG sensor net and the sensor net is connecting to the amplifier.

In contrast to EEG, the magnetic fields induced from neuronal currents are extremely weak, on the order of a billionth of the earth's magnetic field (Hämäläinen, et al., 1993; Baillet et al., 2001), requiring sophisticated detectors with sufficient sensitivities. In the late 1960s, with the invention of a supremely sensitive detector called the superconducting quantum interference device (SQUID), a physicist named David Cohen measured the first human magnetic fields at Massachusetts Institute of Technology in a magnetically shielded room (Cohen, 1972). Different from EEG sensors that are attached to the human scalp, the MEG sensor array (around 100 to 300 sensors) is usually mounted in a whole-head helmet spaced a little distance away from the human head surface (Figure 2.4(b)). This fact allows certain flexibilities in

designing different types of gradiometers, which are helpful to attenuate low-frequency artifacts in the vicinity of the head. Figure 2.4(a) gives examples of one magnetometer and three types of gradiometers. MEG signal acquisitions are usually conducted in a magnetically shielded room (Figure 2.4(c)) to shield external magnetic fields, such as the earth's magnetic field, and also to attenuate high-frequency radio waves.

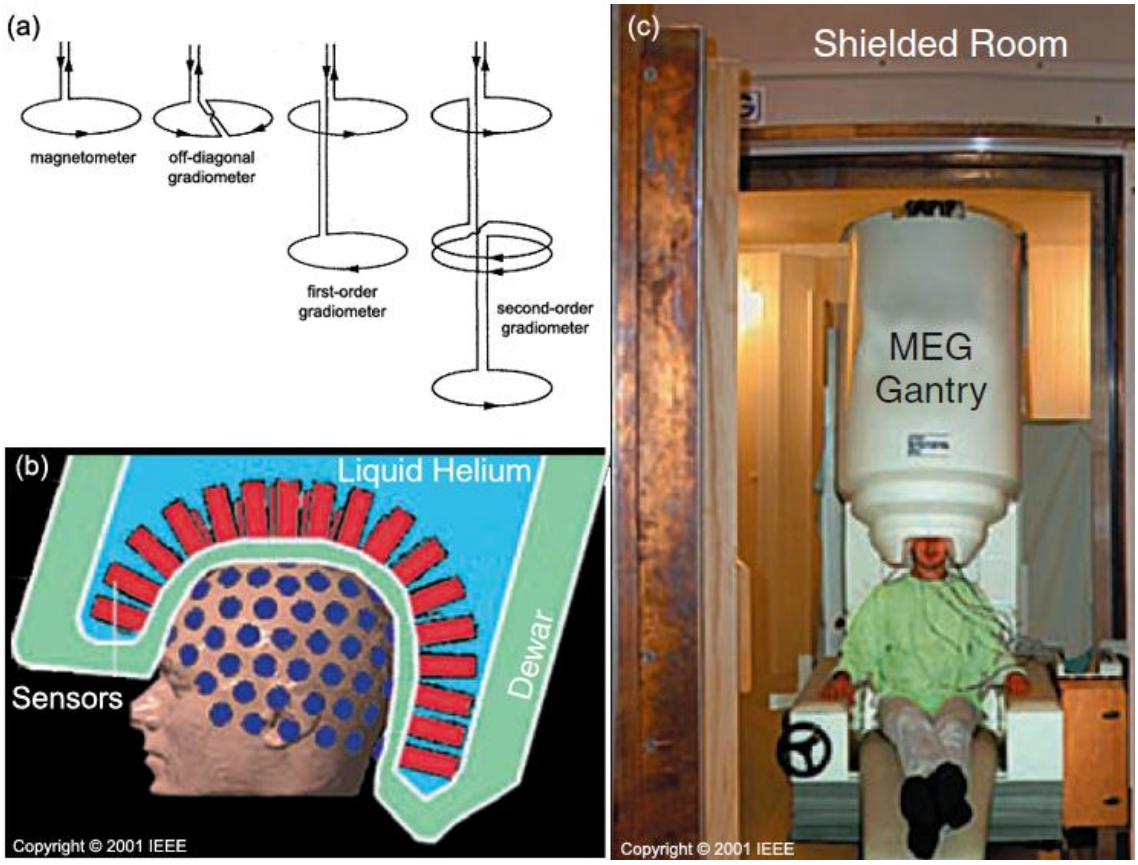

Figure 2.4 Illustration of MEG sensors and recording environment
(a) Different types of MEG magnetometer and gradiometers (from Hämäläinen, et al., 1993). (b) MEG sensors are bathed in low-temperature liquid helium in the dewar (Baillet et al., 2001, with permission). (c) A subject is sitting in the MEG scanner within a magnetic shield room (Baillet et al., 2001, with permission).

Both EEG and MEG have high sampling rates from 250Hz to 2KHz, allowing an excellent temporal resolution of milliseconds to inspect the dynamics of neural activity. However, the spatial resolution of EEG and MEG is limited due to small

number of sensors, e.g. tens to hundreds in EEG and hundreds in MEG. Moreover, the high impedance of the skull causes attenuation of electrical waveforms, resulting in smeared EEG measurements on the scalp, known as the volume conduction effect (van den Broek et al., 1998). Meanwhile, MEG is less affected by the volume conduct effect since head tissues and air are all permeable to magnetic signals (Cohen and Cuffin, 1983). Nevertheless, the spatial resolution of EEG and MEG has been improved by the recent developments in numerical modeling and source imaging techniques.

2.2 EEG/MEG Source Model

2.2.1 Equivalent Current Dipole Model

Many approaches use a mathematical dipole to model electrical brain activation (de Munck et al., 1988; Ebersole, 1994; Stefan et al., 2003; Ebersole and Hawes-Ebersole, 2007; Kaiboriboon et al., 2010). The equivalent current dipole (ECD) source model assumes that measured scalp potentials or magnetic fields are generated from a single or multiple dipoles. Each ECD is characterized by six parameters to infer its location, orientation and strength. These parameters are identified through a minimal least square fitting between the predicted measurements from assumed ECDs and the real measurements (de Munck et al., 1988). According to different freedoms of parameters, ECDs can be classified as fixed dipoles (fixed location and orientation), rotating dipoles (fixed location), and moving dipoles. Dipole localization techniques based on the ECD source model have been clinically applied in localizing focal epileptic sources using interictal and/or ictal activities (Ebersole, 1994; Stefan et al., 2003; Ebersole and Hawes-Ebersole, 2007; Kaiboriboon et al., 2010), and identifying eloquent cortices using evoked potentials or magnetic fields (Wood, 1982; Knowlton

and Shih, 2004; Doss et al., 2009). However, the ECD approach models the center of brain activation as an ideal point, which cannot provide information about the source extent. In order to infer the extent information of epileptic sources for surgical purposes, moving dipoles estimated from a time segment, e.g. the rising phase of interictal spikes (IISs) or initial seizure discharges, form a cluster that indicates the possible spatial extents of the epileptic sources (Bast et al., 2005; Kaiboriboon et al., 2010). However, whether ECD models with ideal point sources are suitable for extended sources is still under debate (de Munck et al., 1988; Merlet and Gotman, 1999; Kobayashi et al., 2005). In fact, the size of cortical activations required for generating potentials that are detectable at the scalp has been suggested to be at least 6 cm^2 *in vivo* (Cooper et al., 1965), and prominent EEG epileptic spikes usually require large areas of 10-30cm^2 (Tao et al., 2005). Moreover, estimated extents for epileptic sources or eloquent cortex from dipole clusters do not necessarily reflect the extents of sources since ECD fitting at each time point might be inaccurate for the reason discussed above, which causes errors in estimated clusters.

2.2.2 Distributed Current Density Model

Recognizing the limitation of the ECD approach, distributed current density (DCD) models have been developed to model spatially extended brain sources, in which the source space is defined as a set of distributed dipoles over the anatomical geometry of the human brain, e.g. a three dimensional (3D) brain volume (Pascual-Marqui et al., 1994; Ding et al., 2006; Ding and He, 2008) or a two dimensional (2D) cortical surface, i.e. cortical current density (CCD) models (Dale and Sereno, 1993). The locations of distributed dipoles have been constrained in a predefined 3D or 2D grid, and dipole

orientations can also be either defined by using two steps (Uutela et al., 1999; Ding and He, 2008) or aligned with anatomical structure, e.g. perpendicular to local cortical surfaces (Dale and Sereno, 1993; Ding, 2009). The DCD solutions with an "image" of dipole strengths distributed over the entire brain volume or the cortical surface thus make it straightforward to infer both location and extent of cortical sources. The extra information of source extent provided by the DCD solutions can further benefit the identification of epileptogenic zones for surgical treatment in partial epilepsy patients (Shirashi et al., 2005; Ding et al., 2007; Plummer et al., 2010).

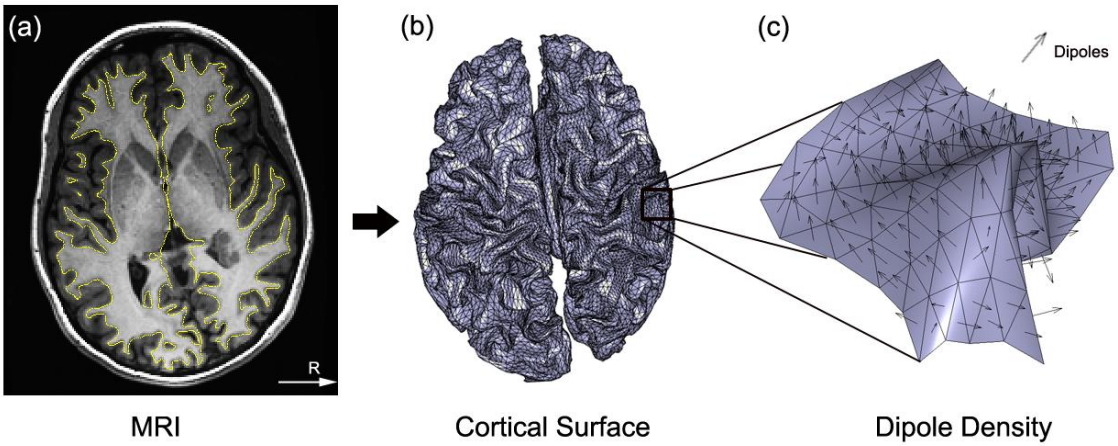

Figure 2.5 Illustration of CCD source model.
(a) Structural MRI of human head with yellow lines indicating the gray/white matter interface. (b) CCD model with a high-resolution triangular mesh representing the cortical surface. (c) Zoomed CCD model with each triangle element containing a unit dipole located in the center of triangle and perpendicular to the local surface.

The CCD model is one commonly used DCD model with distributed dipoles constrained on the thin sheet of the cerebral cortex where most neuron cell bodies and dendrites are concentrated. The orientations of dipoles are assumed perpendicular to the cortical surface because of the columnar organization of pyramidal cells (Figure 2.2(a)). Figure 2.5 gives one example of a CCD model. The cortical surface can be obtained by

segmenting the interface of gray/white matter from a structural MRI image (Figure 2.5(a)), and then tessellating the surface into a high density triangular mesh (Figure 2.5(b)). Each triangular element is represented by a unit dipole placed in the center of the triangle and oriented to be perpendicular to the local surface (Figure 2.5(c)). In the following studies, the CCD model is adopted as the source space with fixed dipole locations and orientations. The only parameters left to be estimated are the dipole strengths. The tessellation of the cortical surface is composed of around 10^3-10^4 triangular elements with area of about $3mm^2$ to represent the sophisticated structure of the human brain, so 10^3-10^4 dipole strengths need to be estimated.

2.3 Volume Conductor Model

In order to reconstruct cortical sources (e.g. equivalent current dipoles in ECD models or tens of thousands of distributed dipoles in DCD models) from scalp measured EEG/MEG, it is necessary to build a volume conductor model to describe conduction profiles of head tissues. Because of the layered structure of head tissues, e.g. scalp, skull, cerebrospinal fluid (CSF) and brain tissues, it is widely accepted to model the head volume conductor as three or four compartments with different conductivities (Hämäläinen and Sarvas, 1989; Fuchs et al., 2001; Vallaghè and Clerc, 2009).

The most classic head model is the three-layer spherical model (de Munck et al., 1988; Hämäläinen and Sarvas, 1989; Grech et al., 2008), in which scalp, skull and brain are modeled as three concentric symmetric spheres with isotropic and homogeneous conductivities (Figure 2.6(a)). With this spherical model, for a given current dipole located inside the most inner layer (i.e. the brain), potentials or magnetic fields measured on the scalp electrodes and sensors can be analytically calculated (de Munck

et al., 1988; Hämäläinen et al., 1993). However, the oversimplified assumption of the head structure as symmetric spheres omitting the realistic head geometry results in localization errors when studying cortical current sources arising from basal and temporal areas (Fuchs et al., 2001).

With advancements in imaging modalities and numerical modeling techniques, head models with realistic geometrical structure are able to be constructed by segmenting head tissues from high resolution magnetic resonance imaging (MRI) or X-ray computed tomography (CT). The finite element method (FEM) is adopted to model the anisotropic and inhomogeneous conductivities in real head tissues (Ramon et al., 2006; Wolters, 2007). However, due to the large computational demand, the FEM model suffers from computer memory constraints and computational difficulties. The boundary element method (BEM) model, with several realistically shaped enclosed surfaces, forms compartments of head tissues with isotropic and homogeneous conductivities (Hämäläinen and Sarvas, 1989; He et al., 1999; Fuchs et al., 2001). Figure 2.6(b) gives one example of the BEM head model containing three compartments, i.e. the scalp, skull and brain, which are segmented from the subject's structural MRI and tessellated into triangular meshes. As an alternative between the oversimplified spherical model and the high computational demands of the FEM model, the BEM model keeps the realistic shape of the head but at the same time it is not computationally expensive. Thus, a three-compartment BEM model is adopted as the volume conductor in the following studies.

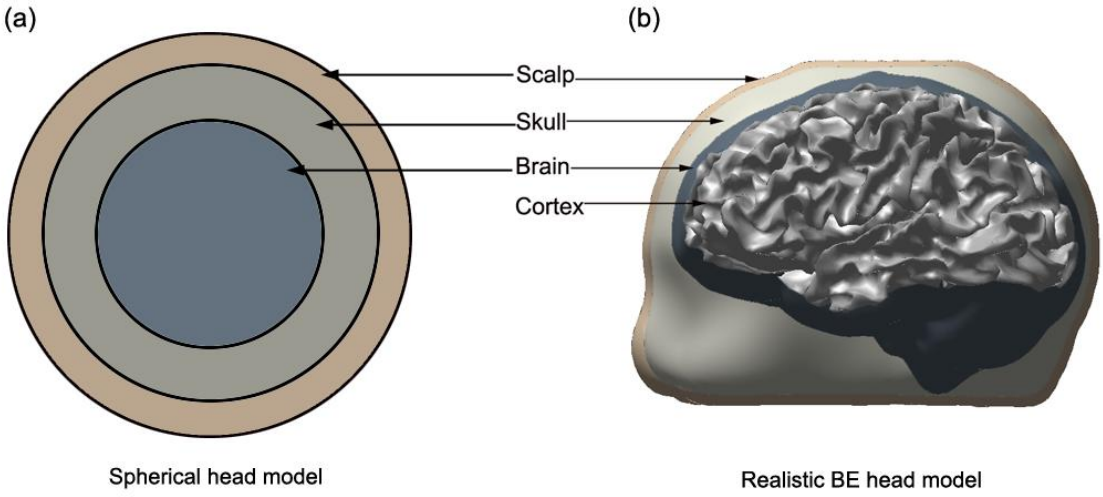

Figure 2.6 Illustration of BE volume conductor model
(a) three-layer spherical head model. (b) three-compartment BE head model.

2.4 The Forward and Inverse Problems

According to the quasi-static approximation of Maxwell's equations, cortical current sources inside the brain and potentials or magnetic fields measured on the scalp are linearly correlated (Baillet et al., 2001). The forward problem is to predict EEG/EMG measurements from known cortical sources (Hämäläinen and Sarvas, 1989; Hämäläinen et al., 1993; Mosher et al., 1999), while the inverse problem is to reconstruct cortical sources from measured EEG/MEG on the scalp (Hämäläinen and Sarvas, 1989; Baillet et al., 2001; Grech et al., 2008).

If the CCD model is adopted as the source space containing N distributed dipoles with fixed locations and orientations, given a cortical current density $\vec{S}$ with N dipole strengths, the potentials or magnetic fields measured at M sensors (denoted by $\vec{\phi}$) can be derived from a simple linear equation (Nunez, 1981)

$$\vec{\phi} = \mathbf{A}\vec{s} + \vec{n}, \tag{2.1}$$

where vector $\vec{n}$ (M×1) denotes measurement noise. The linear relationship between current sources and measurements is contained in the forward matrix $\mathbf{A} = \left(\vec{a}_1, \vec{a}_2, \cdots, \vec{a}_N\right)$ (M×N), also known as the lead field, in which each column $\vec{a}_j$ ($j = 1, 2, \cdots, N$) corresponds to a set of EEG/MEG measurements generated from one unit dipole in the CCD model. The lead field matrix can be derived by solving the EEG/MEG forward problem.

However, solving the inverse problem to reconstruct the cortical sources $\bar{s}$ from a set of EEG/MEG measurements $\vec{\phi}$ in Equation (2.1) is highly underdetermined, due to the tremendous unbalanced numbers between the sources to be estimated (around 10^3~10^4 dipole strengths) and limited EEG/MEG measurements (around 10^2 sensors). Thus, Equation (2.1) may have an infinite number of solutions for a given set of measurements.

2.5 Regularizations

In order to search for a unique solution to the EEG/MEG inverse problem, regularization is a widely accepted strategy by introducing priors. Commonly used priors can be classified into two types: (a) anatomical (or spatial) priors, such as constraining dipole locations and orientations with cortical local geometries (Baillet et al., 2001; Phillips et al., 2002); (b) functional priors, which can be data driven using Bayesian theory (Trujillo-Barreto et al., 2008; Wipf and Nagarajan, 2009) or most generally based on neurophysiological assumptions, such as minimum overall energy of sources (ℓ_2-norm) (Hämäläinen and Ilmoniemi, 1994), maximal sparseness of sources (ℓ_1-norm) (Matsuura and Okabe, 1995; Uutela et al., 1999; Ding and He, 2008) or

smoothness in temporal transitions (Baillet and Garnero, 1997; Ou et al., 2009). The regularized inverse problem can thus be generally expressed as a constrained optimization problem (Adde et al., 2005; Ding, 2009)

$$\min\ L(\vec{s}) \quad \text{subject to } \left\|\vec{\phi} - \mathbf{A}\vec{s}\right\|_2 < \beta, \tag{2.2}$$

where $\left\|\vec{\phi} - \mathbf{A}\vec{s}\right\|_2$ is the data fitting term. $L(\vec{s})$ is known as the regularization term, or model term, which is introduced with prior assumptions about the source distributions. In Equation (2.2), β denotes the regularization parameter which balances the preference on the model term or the data fitting term. The details on how to estimate the regularization parameter β will be described in Section 3.1.

The ℓ_2-norm regularization is based on searching for a unique solution with minimum energy. Minimum norm estimate (MNE) (Hämäläinen and Ilmoniemi, 1994; Fuchs et al., 1999; Pascual-Marqui, 1999) is the most popular ℓ_2-norm based regularization with the model term $L(\vec{s}) = \left\|\vec{s}\right\|_2$, where $\left\|\vec{s}\right\|_2 = \sqrt{\sum_i s_i^2}$. However, it has been shown that MNE cannot reconstruct deep sources due to its preference for shallow and week sources (Baillet and Garnero, 1997; Silva et al., 2004; Grech et al., 2008), which leads to the development of its variants. For example, the weighted MNE (wMNE) (Phillips et al., 2002; Grech et al., 2008) introduces a depth compensation matrix **M** into the model term according to $L(\vec{s}) = \left\|\mathbf{M}\vec{s}\right\|_2$, and low-resolution brain electromagnetic tomography (LORETA) (Pascual-Marqui et al., 1994) further integrates a Laplacian matrix **L** as a local spatial smoother into the model term according to $L(\vec{s}) = \left\|\mathbf{LM}\vec{s}\right\|_2$. Although ℓ_2-norm regularization can be solved efficiently by linear operators (Grech et al., 2008), they belong to the class of quadratic regression problems

(Hoerl and Kennard, 1970), which assume Gaussian distributed source fields (Uutela et al., 1999) and usually produce over-smoothed estimations (Pascual-Marqui et al., 1994; Vega-Hernández et al., 2008). The nature of smoothness makes them not suitable for estimating source extents from early sensory brain responses and focal epilepsy, in which sources are known to be compact (Allison et al., 1989; Oishi et al., 2002).

Other regularizations utilizing non-quadratic regression schemes, such as the ℓ_1-norm (Tibshirani, 1996; Uutela et al., 1999; Ding and He, 2008) or ℓ_p-norm ($0<p\leq 1$) using iterative approaches (Gorodnitsky and Rao, 1997; Han, et al., 2007; Xu et al., 2007), have demonstrated sparse solutions to address the smoothness issue. However, iterative approaches, e.g. focal underdetermined system solver (FOCUSS) (Gorodnitsky and Rao, 1997), usually require initialization to start and cannot guarantee convergence in finite iterations. Most of ℓ_1-norm regularizations constrain the source itself, i.e. $L(\vec{s}) = \|\vec{s}\|_1$, where $\|\vec{s}\|_1 = \sum_i |s_i|$, including the selective minimum-norm method (Matsuura and Okabe, 1995), minimum current estimate (MCE) (Uutela et al., 1999), least absolute shrinkage selection operator (LASSO) (Tibshirani, 1996), and sparse source imaging (SSI) (Ding and He, 2008), which are based on the assumption of super-Gaussian distributed source fields (Uutela et al., 1999). This assumption leads to over-focused solutions, which do not reflect accurate source extents either (Chang et al., 2010; Ding et al., 2011).

The utilization of ℓ_1-norm regularization in solving the underdetermined EEG/MEG inverse problem can be treated as an application of compressive sensing (CS) theory (Donoho, 2006), which states that a signal can be recovered exactly from highly under sampled measurements using the ℓ_1-norm regularization if the signal is

sparse or compressible enough (Candès et al., 2006). The over-focused solutions in conventional ℓ_1-norm regularizations imply that the cortical source itself may not be sparse enough for the CS theory. It has been further shown that the sparseness condition can be extended to transform domains (Candès and Romberg, 2007). The question is whether we can find a transform domain where the cortical current activity is sufficiently sparse; then a better reconstruction accuracy can be achieved using the ℓ_1-norm regularization.

Chapter 3: Variation Based Sparse Source Imaging

The idea of transform sparseness in solving EEG/MEG inverse problem was first reported by Ding in 2009 using a variation transform, which computes variations between neighboring elements. Its objective function mainly penalizes boundaries between active and inactive cortical areas using ℓ_1-norm minimization and thus enforces them as sparse features. Previous simulation study (Ding, 2009) has suggested that this variation based sparse source imaging (V-SSI) method is able to reconstruct extended cortical sources with high accuracies, which is of particular importance in estimating the location and extent of epileptogenic zones (EZs) (i.e. the cortical areas responsible for the generation of epileptic discharges) to perform brain resections for partial epilepsy patients (Engel, 1993; Rosenow and Lüders, 2001).

In this chapter, the V-SSI technique is applied for the first time to clinical MEG recordings of epileptic interictal spikes (IISs) to identify irritative zones (IZs) (i.e. an alternative zone to define EZ) for medically refractory epilepsy patients. Total of 108 IISs were selected from three epilepsy patients by experienced doctors to perform V-SSI source analysis. Cortical patch sources are formed from the rising phases of IISs, spike peaks or entire spikes to estimate the location and extent of IZs and validated using pre-surgical evaluations, such as clinical diagnosis, MRI lesions or resection areas when possible. Other source imaging methods, i.e. MNE and classic SSI, are also performed for the purpose of comparison. The spatio-temporal dynamics of the reconstructed cortical sources are further used to investigate propagation patterns for epileptic activities. The results of this chapter have already been published in the Journal of Clinical Neurophysiology in 2013 (Zhu, et al., 2013c).

3.1 Variation Based Sparse Source Imaging Method

In the CCD model meshed with triangles (see Section 2.2.2 for details), the linear variation operator is defined to calculate variations between two neighboring triangles which share the same edge (Ding, 2009):

$$\mathbf{V}=\begin{bmatrix} v_{11} & v_{12} & \cdots & v_{1N} \\ v_{21} & v_{22} & \cdots & v_{2N} \\ \vdots & \vdots & \ddots & \vdots \\ v_{P1} & v_{P2} & \cdots & v_{PN} \end{bmatrix} \quad \begin{cases} v_{ij}=1; v_{ik}=-1; & \text{if elements } j,k \text{ share the same edge } i \\ v_{ij}=0; & \text{otherwise} \end{cases}, \quad (3.1)$$

where P is the total number of triangular edges in the CCD model. If cortical current densities have uniform distributions or can be approximately represented by uniform distributions (Cottereau et al., 2007), large variations as sparse features often occur on boundaries between active and inactive areas that can be used to identify source extents (Ding, 2009). Thus, variations, as sparse representations of the cortical current density, are then implemented into Equation (2.2) with the ℓ_1-norm of variations as the model term (Ding, 2009) according to

$$\min \left\| \mathbf{V}\vec{s} \right\|_1 \quad \text{subject to} \quad \left\| \vec{\phi} - \mathbf{A}\vec{s} \right\|_2 < \beta \quad (3.2)$$

where **V** is the variation transform matrix defined in Equation (3.1) and definitions for $\vec{s}$, $\vec{\phi}$, and **A** are all as the same as in Equation (2.1). In Equation (3.2), β is the regularization parameter, estimated by the discrepancy principle (Morozov, 1966). If assuming Gaussian white noise with variance σ^2, $(1/\sigma^2)\|n\|_2^2$ has the χ_M distribution with M degree of freedom, i.e., χ_M^2. In practice, β is selected as the upper bound of the confidence interval $[0,\beta]$ that integrates to 0.99 probabilities. In the analysis of real MEG data, noise variance is estimated using the 20th percentile data of the lowest

powers in the selected IISs (Fuchs et al., 1998).

Since the optimization problem in Equation (3.2) is convex, it can be reformulated into a second-order cone program (SOCP) (Lobo et al., 1998) by introducing intermediate parameters, yielding

$$\min_{\vec{s}} \sum_{i=1}^{P} f_i \quad \text{subject to } \vec{n} = \vec{\phi} - \mathbf{A}\vec{s};\ \|\vec{n}\|_2 \le \beta;\ \left\| \sum_{j=1}^{N} v_{ij} s_j \right\|_2 \le f_i \quad i = 1, 2, \cdots, P \tag{3.3}$$

where v_{ij} are elements in the variation transform matrix **V**. Intermediate parameters f_i (non-negative) are introduced as upper bounds for the ℓ_1-norms of the variations. N is the number of the triangles in the CCD model and P is the number of triangular edges. The SOCP problem can be solved by using the Interior Point Method (Boyd and Vandenberghe, 2004), which is integrated in a Matlab package named Self-Dual-Minimization (SeDuMi) (Sturm, 1999). The reason to use SeDuMi is that it is an efficient solver for optimization problems with linear and quadratic constraints by exploring sparseness, which is consistent with our assumption of sparseness.

3.2 Data Acquisition and Analysis

3.2.1 Patients and MEG Acquisition

Three patients (two females and one male, Table 3.1) with medically refractory focal epilepsy were studied using a protocol approved by the Institutional Review Board of the University of Oklahoma Health Science Center, OK and United Hospital, St. Paul, MN. The clinical studies took place at the MEG/MSI Center at the Minnesota Epilepsy Group, St. Paul, MN. Each patient received a whole head three-dimensional (3D) MRI scan with standard epilepsy protocol. 3D axial T1-weighted structural MRI images were obtained from a GE 3 Tesla scanner using a SPGR sequence (TR=7ms,

TE=3ms, FOV=24×24cm, slice thickness=1.4mm). High density MEG was recorded using a whole head, 148-channel Magnes WH2500 neuromagnetometer array (4-D Neuroimaging, San Diego, CA, USA) for 10 to 20 minutes in a magnetically shielded room. The sampling rate for MEG recording was 508.63 Hz. A band-pass filter from 1 Hz or 3 Hz to 70 Hz was applied.

3.2.2 Source Model and Volume Conductor Model

BEM head models were obtained by segmenting the surfaces of the scalp, skull and brain from anatomical MRI data for each patient, using the BrainSuite software (Shattuck et al., 2002). Each surface was tessellated into a mesh of about 3000 triangles. The conductivities of these three major tissues were set as 0.33/Ω.m, 0.0165/ Ω.m, and 0.33/Ω.m respectively (Lai et al., 2005). Cortical surfaces were derived by segmenting the interface between gray and white matter using the same software and triangulated into high-resolution meshes (~50000 triangles) to build the CCD model. Head surfaces were digitized by the Polhemus fast-track headshape digitization kit with around 2000 samples. Precise co-registration between MEG sensors and BE and CCD models was achieved first by aligning fiducial points (left and right preauricular points and nasion) from MRI data and MEG coils, and further refined by fitting segmented scalp surfaces from MRI onto digitized head surfaces.

3.2.3 MEG Data Analysis

Clinical MEG recordings of IISs and abnormal MRI lesions were visually identified and marked by experienced epileptologists from the MEG/MSI Center. The epileptologists were blind to source analysis results when working on MRI data to

Table 3.1 Diagnosis and pre-surgical evaluations

Pt.	Sex	Age	Diagnosis	MRI	Operation	Pre-op Seizure Freq	follow-up
1	F	21	Medically refractory complex partial seizure; extensive cortical developmental disorder	cortical developmental disorder with multiple heterotopia at right temporal	No surgery was performed due to the extensiveness of the lesion	Simple partial seizure daily, complex partial seizure monthly	
2	F	11	Medically refractory epilepsy; Tuberous sclerosis complex	Multiple cortical and subcortical tubers, bilaterally; Subependymal nodules	Right frontal temporal topectomy	Daily seizure since 2 months of age	Seizure free first year, and one seizure in two years with anti-epileptic medicine
3	M	6	Medically refractory complex partial seizure; Landau-Kleffner syndrome	Normal	Multiple subpial transection in other institution	Daily multiple seizure	

identify lesions and persons who performed source analysis were blind to clinical diagnosis results and surgical outcomes. IISs without artifacts (e.g., heartbeat, muscle movement, or eye blink) were chosen for source analysis (24, 55, and 29 IISs for three patients respectively) (Table 3.2). Averaged signal-to-noise ratio (SNR) in IISs, calculated using amplitude ratio (Bast et al., 2006), was about 3.4 over all patients (Patient 1: 3.4, Patient 2: 2.5, and Patient 3: 4.2). Source analysis by V-SSI was performed on the MEG data of each IIS at about 60 milliseconds, including rising and descending phases of IIS, which is consistent with the typical duration of IISs in epilepsy (Adjouadi et al., 2005). This computation resulted in 30 snapshots of reconstructed CCD maps for each IIS and a total of about 700, 1600, and 900 CCD maps in the three patients, respectively. A statistical analysis was conducted on these CCD maps to identify cortical areas that were frequently activated. First, each CCD map was thresholded at a certain ratio of its maximum value. The ratio was selected by inspecting the histogram of dipole moments over the CCD model, which varied in different IISs while was fixed within each IIS. Then, the active frequency (AF) of each triangular element in CCD was defined as the percentage of being active in CCD maps from all IISs in a patient and was calculated in three different IIS durations: peaks, rising phases, and entire spikes (Table 3.2), since IIS sources might change over time (Kaiboriboon et al., 2010). Finally, cortical areas, formed by a group of triangular elements of active frequencies over a certain value (10% was used in the present study), were considered as potential sources responsible for the generation of IISs.

3.2.4 Evaluation Methods

Cortical areas derived from the above analysis were further divided into cortical

patch sources according to their locations and active frequencies and compared with pre-surgical evaluation data, e.g., MRI lesions (Patient 1 and Patient 2), surgical resection areas (Patient 2), and pathologic data (Patient 3), to assess the performance of V-SSI. At each IIS, if the thresholded CCDs had a spatial overlap of more than 50% with a cortical patch source, one is counted for detection of the corresponding patch source. The detection rate (DR) of each cortical patch source was calculated as the ratio between the number of IISs that detected for the cortical patch source and the total number of IISs in a patient. DRs were also evaluated at IIS peaks, rising phases, and entire spikes. The difference among cortical sources from three IIS durations in defining IZs was compared. Source reconstructions from MNE, SSI, and V-SSI were also compared.

3.4 Source Reconstruction Results

3.4.1 Comparisons of MNE, SSI and V-SSI

Figure 3.1 illustrates an example of reconstructed cortical current densities by MNE, SSI, and V-SSI from Patient 1. It can be observed that the reconstructed current density by MNE is diffused over the right temporal and posterior inferior frontal lobes and the reconstructed current density by SSI is very sparse and focused on a few spots over the similar areas. Meanwhile, the reconstructed current density by V-SSI is continuously distributed and confined within the temporal lobe (Figure 3.1(a)). After thresholding (Figure 3.1(c-d)), while all three methods indicate sources on the right temporal lobe, current densities from MNE and SSI are discontinuous and more spatially scattered as compared with those from V-SSI, which makes them not reliable in evaluating source extents. Furthermore, the results from V-SSI are more robust to

threshold values than MNE and SSI. Different ratios (30% or 60%) only produce about 25% size reduction in V-SSI results, but 94% in MNE and 84% in SSI.

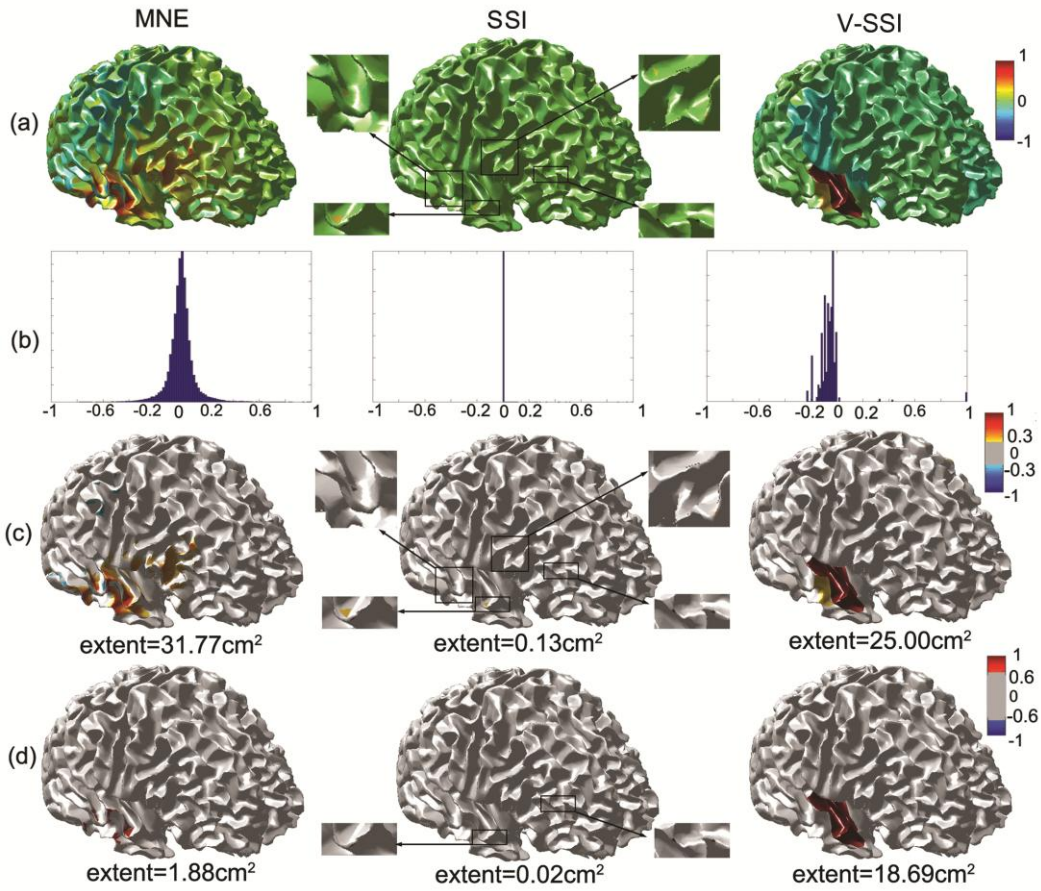

Figure 3.1 Comparison of MNE, SSI and V-SSI
(a) Reconstructed CCD maps without thresholding (dipole amplitudes are normalized to individual maxima. Positive: outflow current; Negative inflow currents. (b) Histograms of amplitudes of dipoles in CCD maps from MNE, SSI, and V-SSI. (c)-(d) CCD maps thresholded at 30% and 60% of individual maxima.

3.4.2 Localization of irritative zones in individual patients

Patient 1 (21 years old, female) had daily simple partial seizures and monthly complex partial seizures (Table 3.1). Pre-surgical diagnosis showed that she had extensive cortical development disorder of the right temporal and parietal regions (Table 3.1) and the MRI lesions indicate multiple heterotopias in the posterior and

middle temporal lobes and the parietal lobe near the lateral fissure (Figure 3.2(c)). Cortical areas of high AFs (Figure 3.2(a)) at three IIS phases all suggest extended MEG sources on the right temporal lobe. Five cortical patch sources within the right temporal lobe (RT1, RT2, and RT3), right frontal lobe (RF1), and left parietal lobe (LP1) are identified. RT1 of the highest AF (about 50%) (Table 3.2), which is located on the right superior temporal lobe and extends into the deep right lateral fissure, is overlapped with MRI lesions (Figure 3.2(d)). Both RT2 and RT3 have AFs ranging from 10% to 20% in three IIS phases and are in the neighboring areas of the MRI lesions (RT2: anterior right temporal lobe and RT3: the posterior temporal lobe). RF1 exceeds 10% AF only during IIS peaks (AF: ~16%) and locates on the right posterior inferior frontal lobe. LP1 is a focal source on the left central sulcus (AF: ~10%-20%).

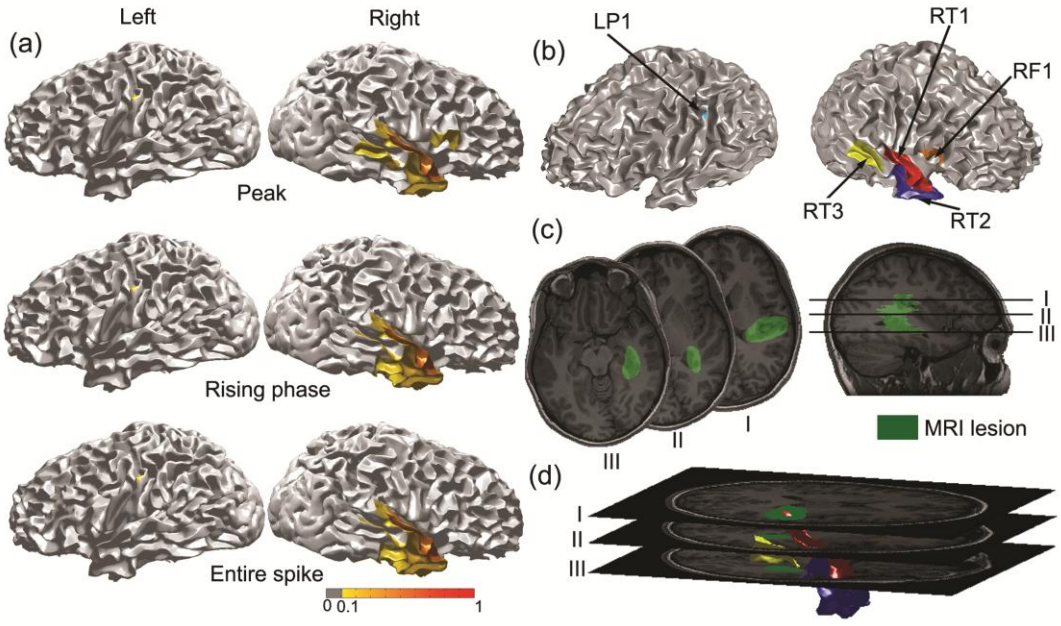

Figure 3.2 Comparison of V-SSI sources and MRI lesions in Patient 1
(a) Frequency maps (AF>10%) at IIS peaks, rising phases, and entire spikes. (b) Cortical patch sources, color-coded and denoted as RT1, RT2, RT3, RF1, and LP1, were identified from frequency maps. (c) Axial views of MRI with lesions (green) marked by experienced epileptologists. (d) Co-registered display of MRI and sources RT1, RT2, and RT3.

Table 3.2 Summary of reconstruction results

MEG			Reconstruction results									MRI lesions	
Pt.	Dura-tion (min)	# of IIS	Source patch	Location		Active frequency (threshold at 10%)			Detection rate			Location	
				side	lobe	Peak	Rising phase	Entire spike	Peak	Rising phase	Entire spike	side	lobe
1	20	24	*RT1*	R	LS	48.98%	45.50%	46.47%	11(45.83%)	16(66.67%)	20(83.33%)	R	LS
			RT2	R	ant. T	12.93%	20.96%	19.65%	4(16.67%)	12(50.00%)	14(58.33%)	R	ant. T
			RT3	R	post. MT	16.43%	11.50%	12.16%	3(12.50%)	11(45.83%)	12(50.00%)	R	MT
			RF1	R	inf. F	16.26%	-	-	3(12.50%)	5(20.83%)	8(33.33%)		
			LP1	L	CS	12.50%	23.21%	23.42%	5(20.83%)	9(37.50%)	15(62.50%)		
			Others						8(33.33%)	4(16.67%)	4(16.67%)		
2	20	55	*RF1*	R	ant. LF	23.32%	16.75%	18.15%	14(25.45%)	28(50.91%)	34(61.82%)	R	ant. LF
			RF2	R	MF	-	-	10.06%	8(14.55%)	26(47.27%)	30(54.55%)	R	CS
			RP1	R	CS	22.80%	15.36%	14.14%	14(25.45%)	24(43.64%)	28(50.91%)	R	LS
			RP2	R	LS	10.61%	16.70%	13.28%	4(7.27%)	24(43.64%)	29(52.73%)	L	inf. P
			LF1	L	MF	-	12.88%	10.30%	1(1.82%)	19(34.55%)	24(43.64%)		
			Others						21(38.18%)	6(10.91%)	3(5.45%)		
3	10	29	*LF1*	L	inf. F	53.27%	24.58%	37.58%	17(58.62%)	20(68.97%)	27(93.10%)		
			LF2	L	sup. F	-	17.82%	15.44%	2(6.90%)	11(37.93%)	15(51.72%)		
			LF3	L	sup. F	11.37%	-	11.23%	4(13.79%)	7(24.14%)	17(58.62%)		
			LF4	L	MF	10.25%	-	-	2(6.90%)	9(31.03%)	12(41.38%)		
			LP1	L	post.LS	78.28%	45.59%	47.30%	25(86.21%)	26(89.66%)	27(93.10%)		
			Others						9(31.03%)	5(17.24%)	0(0.00%)		

L = Left, R = right, ant = anterior, post = posterior, inf = inferior, LS = lateral sulcus, CS = central sulcus, T = temporal, P = parietal, MT = middle temporal, MF = middle frontal, LF = lateral frontal, IIS = interictal spike. Italic fonts: cortical sources consistent with presurgical evaluations. Others: IISs that suggest no sources supported by MRI lesions in first two patients and language-related areas in LKS in third patient (i.e., no sources marked by italic fonts).

The detection rate data (Table 3.2) suggest that the source overlapped with the MRI lesions (RT1) is most frequently active, at 45.83% for IIS peaks, 66.67% within rising phases, and 83.33% in entire spikes. During rising phases, two sources (RT2 and RT3) from the neighboring areas of MRI lesions have higher DRs than other two sources (LP1 and RF1). While there is a slight DR increase for RT2 and RT3 in entire spikes as compared with rising phases, such increases for LP1 and RF1 are more significant. Data from IIS rising phases and entire spikes show significant simultaneous activations of multiple sources in individual IISs (thus total DR is >100%), which implies possible dynamic connections among them. In total, 20 out of 24 IISs have source(s) of RT1, RT2, RT3, or their combinations (Table 3.2) that suggests the IZs are located around MRI lesions.

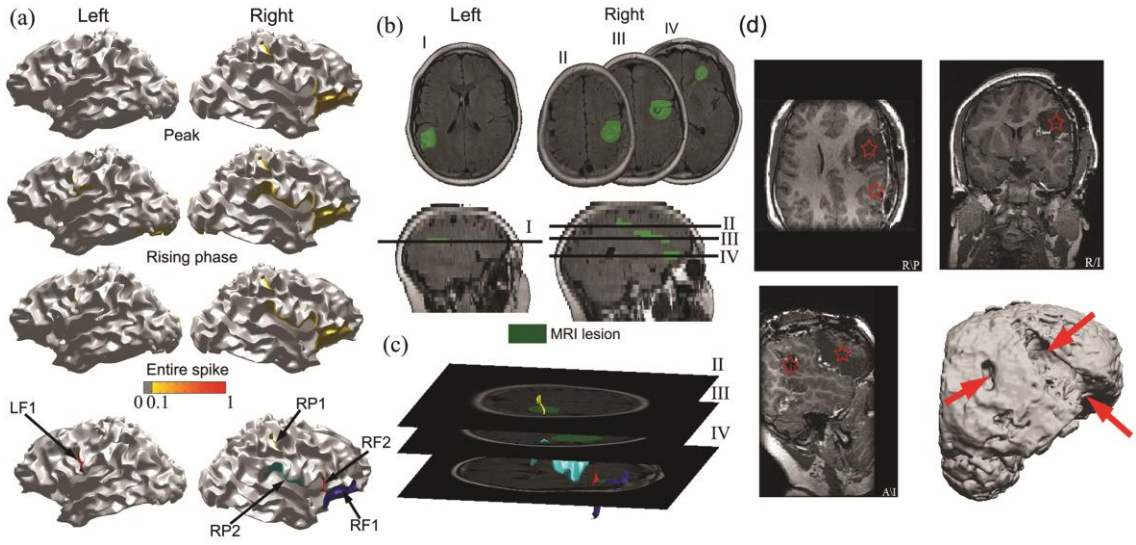

Figure 3.3 Comparison of V-SSI sources, MRI lesions, and post-surgical MRI in Patient 2

(a) Frequency maps (AF>10%) at IIS peaks, rising phases and entire spikes. Cortical patch sources were color-coded and denoted as RF1, RF2, RP1, RP2 and LF1. (b) Axial and sagittal views of MRI with lesions (green) marked by experienced epileptologists. (c) Co-registered display of MRI and sources RF1, RF2, RP1, and RP2. (d) Post-surgical MRI and rendered cortical surface showing resection areas (red stars).

Patient 2 (11 years old, female) had daily seizures since two months of age (Table 3.1). Frequency maps at three IIS phases all indicate multiple cortical patch sources within frontal (RF1, RF2, and LF1) and parietal (RP1 and RP2) lobes on both hemispheres (Figure 3(a)). RF1, RF2, RP1 and RP2 have relatively higher AFs than other sources (Table 2). RF1 is at the anterior portion of the right inferior frontal lobe; RF2 is in the middle of right inferior frontal lobe; RP1 is located on the right central sulcus at the juncture of frontal and parietal lobes; and RP2 appears on the right joint region of the frontal and parietal cortices close to the right temporal fissure. A left-hemisphere source (LF1) appears on the posterior middle frontal lobe that seems mirrored from RP2. The bilateral distribution of IIS sources is consistent with the clinic diagnosis that the patient had multiple cortical and subcortical tubers bilaterally distributed in the frontal and parietal cortices (Table 3.1) and MRI data that indicated multiple subependymal nodules located at the anterior and medial sections of the right frontal cortex and the medial section of the left parietal cortex (Figure 3.3(b)).

Both RF1 and RP1 are overlapped with MRI lesions (Figure 3.3(c)), which have relatively higher AFs and DRs (Table 3.2) than other sources during IIS peaks, while RF2 and RP2 from the neighboring areas of MRI lesions have similar DRs as RF1 and RP1 in IIS rising phases and entire spikes. The DRs of LF1 are slightly lower than all other sources. DRs of individual sources in this patient are generally lower than Patient 1, which suggests that multiple sources from different locations might be responsible for the generation of IISs. This is consistent with the known presence of extensive brain lesions and multiple brain resections. The patient received a right frontal temporal lobectomy, and after surgery, she became seizure free for the first year and had only one

seizure in the first two years while remaining on antiepileptic medication (Table 3.1). The cortex surface rendered from the post-surgery MRI data indicates multiple resection areas on the right frontal and temporal areas (Figure 3.3(d)), consistent with areas covered by RF1, RF2, RP1, and RP2. Data from IIS rising phases and entire spikes indicate significant simultaneous activation of multiple sources in individual IISs, similar as in Patient 1. In total, 52 out of 55 IISs in this patient have source(s) of RF1, RF2, RP1, RP2, or their combinations (Table 3.2) that suggests the IZs are located around MRI lesions.

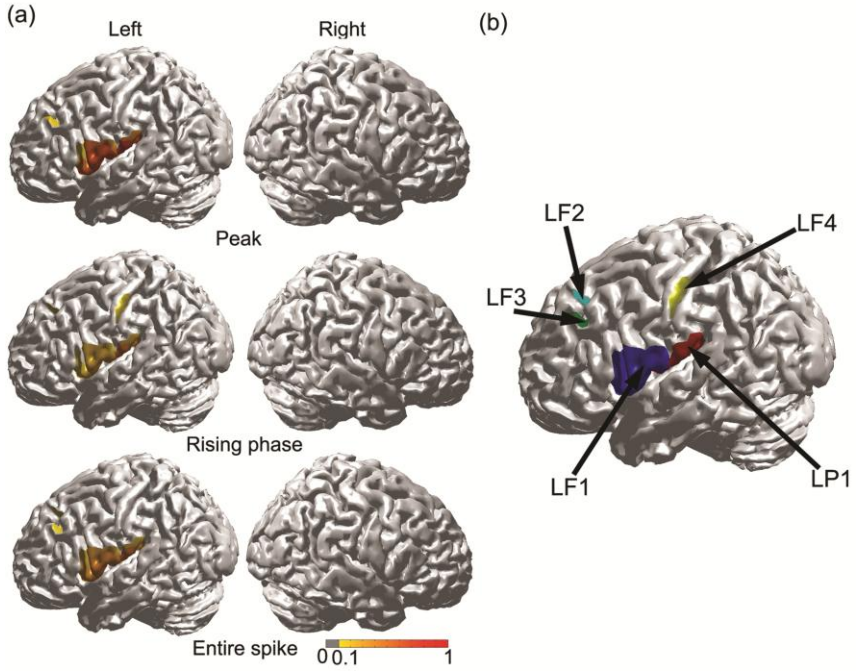

Figure 3.4 Cortical sources from V-SSI in Patient 3
(a) Frequency maps (AF>10%) at IIS peaks, rising phases, and entire spikes.
(b) Cortical patch sources were color-coded and denoted as LF1, LF2, LF3, LF4, and LP1 from frequency maps.

Patient 3 (6 years old, male) had multiple partial seizures every day (Table 3.1). Reconstructed CCD maps from three IIS phases all suggested dominant activity on the adjacent cortical areas to the left lateral fissure (i.e., LF1 and LP1) (Figure 3.4). While

LP1 is located on the posterior section of left lateral fissure, LF1 covers the anterior section of left lateral fissure. There are also sources superiorly neighboring LF1 and LP1 toward the left motor area (LF4) and frontal area (LF2 and LF3). AFs of LF1 and LP1 are much higher than other sources (Table 3.2). The pre-surgical evaluation indicated that this patient has a Landau-Kleffner syndrome (LKS) (Landau and Kleffner, 1957; Rotenberg and Pearl, 2003), characterized by the development of aphasia, associated seizure disorders and abnormal EEG/MEG (Knowlton and Shih, 2004). The seizure focus for LKS patients is likely located on the intra-sylvian cortex (Paetau et al., 1999), which is consistent with LF1 and LP1 in this patient. Specifically, the spatial extent of LF1 covers the Broca's area (associated with language reproduction and comprehension) and LP1 covers part of Wernick's area (associated with auditory processing) (Figure 3.4(b)). This patient had a normal MRI. The detection rates for both LF1 and LP1 are significantly higher than others (Table 3.2). Furthermore, the activations of LF1 and LP1 are almost simultaneous in all IISs as suggested by over 93% detections in entire spikes. Every IIS has a source of LF1 and LP1 or their combinations (Table 3.2) that suggests the area near the left sylvian fissure is the most likely IZ for this patient.

3.4.3 Comparison of cortical sources at IIS peaks, rising phases, and entire spikes

Active frequencies for the sources that are overlapped or close to MRI lesions exhibit small variations during different IIS phases, such as RT1, RT2, and RT3 in Patient 1 and RF1, RF2, RP1, and RP2 in Patient 2 (*italics* in Table 3.2). In Patient 3, active frequencies of sources suggesting IZs (both LF1 and LP1) are higher during IIS peaks than rising phases and entire spikes, which are caused by the dominant and

consistent activations in these areas especially when the strength of activity is enhanced during IIS peaks. These observations suggest that possible IZs are actively involved in the initiation and evolution of IISs through their courses. Meanwhile, the detection rate data (Table 3.2) indicate that sources suggesting possible IZs are not identified in over 34% of IIS peaks (averaged in three patients), while these sources are missed in only about 15% of IISs during rising phases.

3.4.4 Reconstruction of cortical source dynamics

Figures 3.5 and 3.6 illustrate two examples of source dynamics from two different IISs in Patient 1. Figure 3.5 shows a source that is localized and distributed

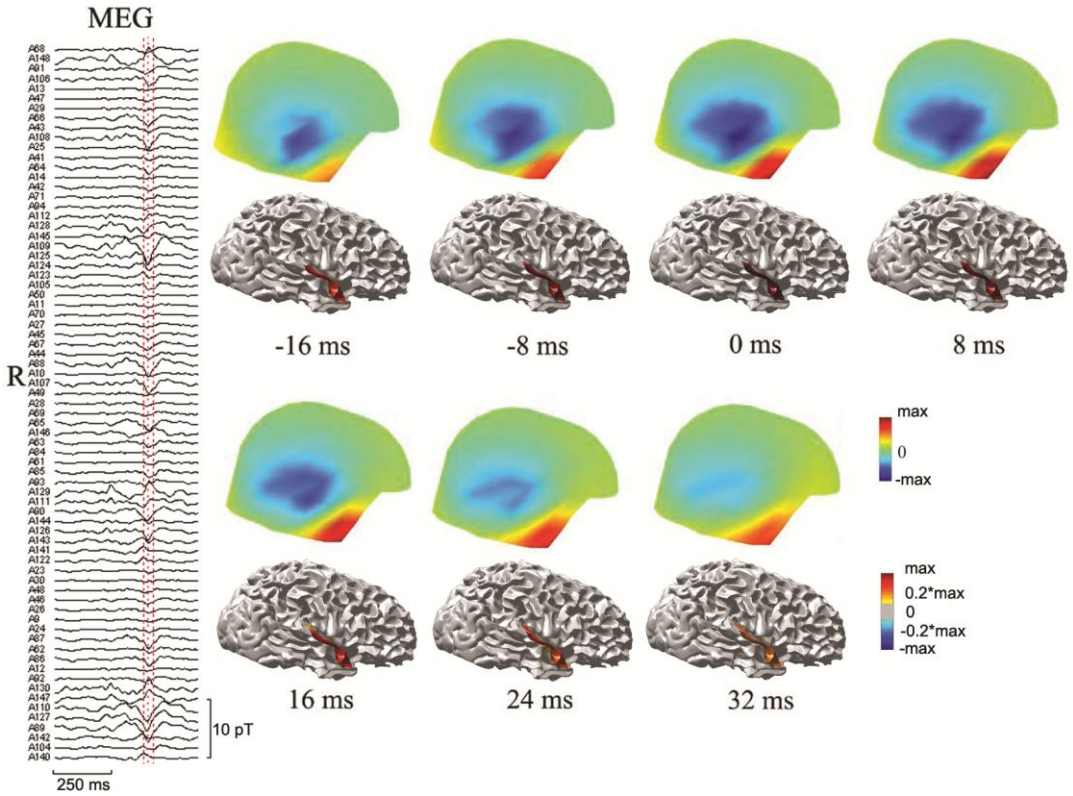

Figure 3.5 Patient 1: an example of stable cortical sources
Left: IIS MEG waveforms from the right hemisphere. Right: magnetic fields and reconstructed CCD maps from -16 ms to 32 ms (between left and right dashed lines for the duration of IIS and the dashed line in the middle marks the IIS peak as 0 ms).

similarly as RT1 (Figure 3.2(b)). While it remained unchanged in location, its strength was first enhanced at -16 ms, reached the maximum at 0 ms, and then slowly decreased after 8 ms. Figure 3.6 shows another example from the same patient, which indicates a dynamic pattern of propagation. A source with outward currents (RT1 area) first appeared on the right lateral fissure at -24 ms, accompanied by smaller inward currents (RT2 area). While the inward currents weakened after -16 ms, the outward currents were slowly enhanced and reached maximum between 0 ms and 8 ms. The source started to shift to the tip of the right temporal cortex (from RT1 to RT2) at 16 ms and mostly propagated down to the RT2 area with reduced strength at 24 ms. This example illustrates causal dynamic patterns between RT1 and RT2.

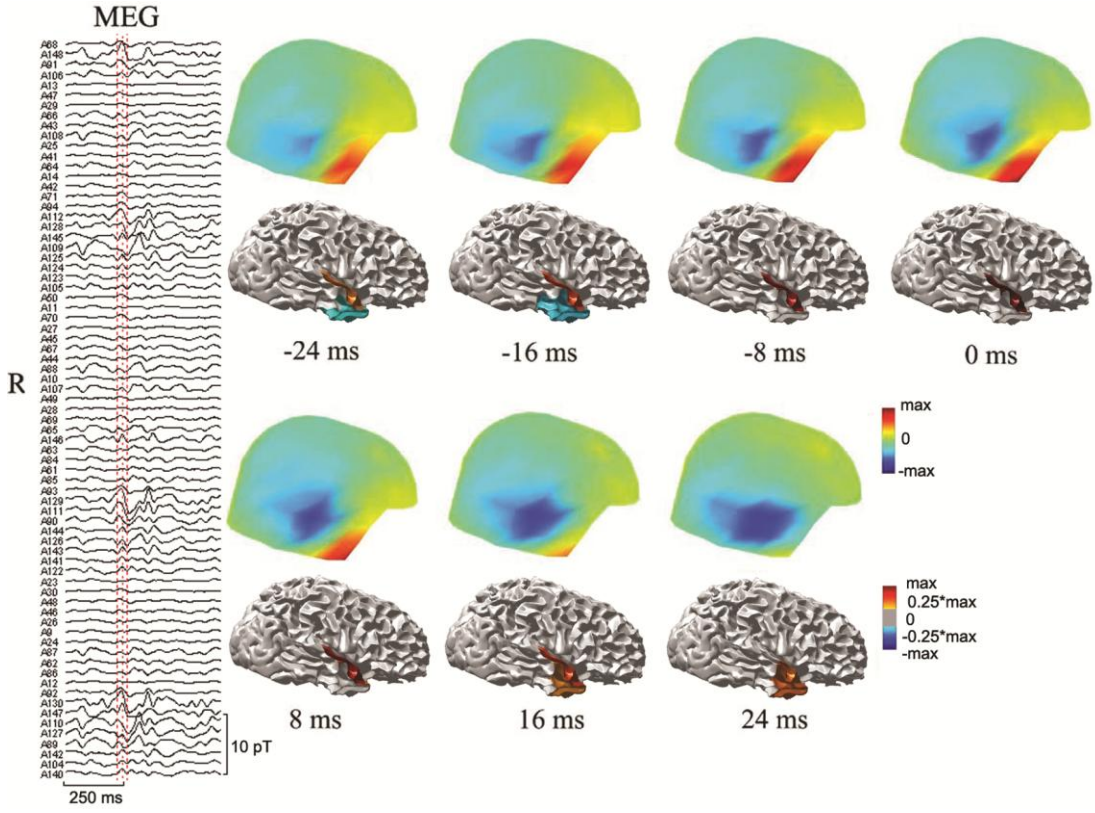

Figure 3.6 Patient 1: an example of local propagation within temporal lobe
Left: IIS MEG waveforms from the right hemisphere. Right: magnetic fields and reconstructed CCD maps from -24 ms to 24 ms.

Figure 3.7 illustrates an example of dynamic connection of cortical sources from Patient 2. The active source (RP2 area) is initially developed on the right lateral fissure at -32 ms. At -16 ms, it slowly propagated to the anterior inferior frontal lobe (RF1) in the same hemisphere and finally localized to the RF1 area at 0 ms. Its strength increased to reach the maximum between 0 ms and 8 ms. From 8 ms to 24 ms, the source started to oscillate back to the adjunct area between frontal and parietal lobes (RP2 area).

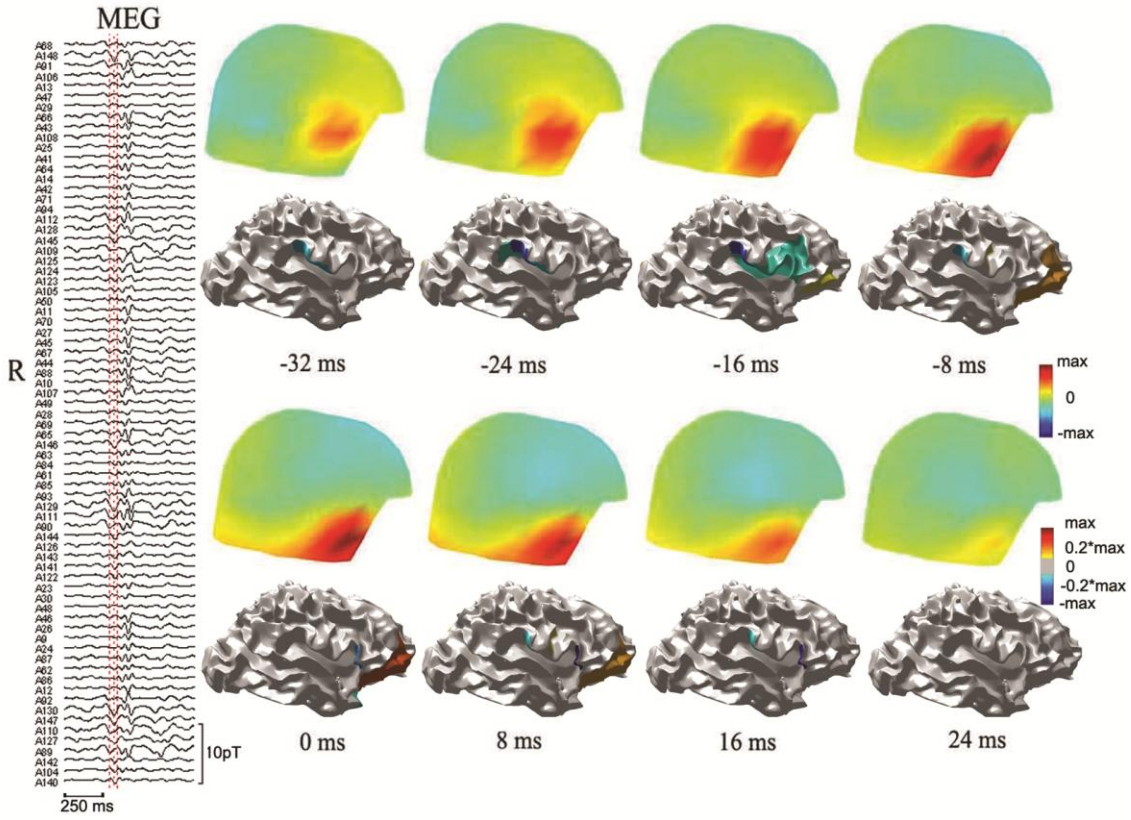

Figure 3.7 Patient 2: an example of propagation within the same hemisphere
Left: IIS MEG waveform from the right hemisphere. Right: magnetic fields and reconstructed CCD maps from -32 ms to 24 ms.

Figures 3.8-3.10 present three different propagation patterns in Patient 3. Figure 3.8 shows an example of propagation within adjacent areas. From -32 ms to -8 ms, a source (LP1) localized to the Wernicke's area first appeared as outward currents and slowly changed to inward currents. It is further enhanced between -8 ms to 0 ms and

weakened afterward. At the same time, the Broca's area (LF1) was activated at -8 ms after the activation of LP1, which is then increased and decreased from 8 ms to 24 ms. The timing difference between LP1 and LF1 suggests the local propagation among them. Figure 3.9 illustrates an example of cross-hemispheric propagation in symmetric cortical structure. A source on the left lateral fissure (both LF1 and LP1) appeared at -32 ms and its strength was enhanced from -8 ms to 24 ms. Another weaker source on the right lateral fissure, symmetric to LF1 and LP1, is seen between 32 ms and 40 ms when the activation on the left was significantly weakened. Figure 3.10 displays an example for early cross-hemisphere propagation during the IIS rising phase. A source on the left temporal lobe starting from -40 ms induced another source on the contralateral site at -32 ms. After -16 ms, while the source on the left remained stable, the source on the right exhibited an on-and-off pattern.

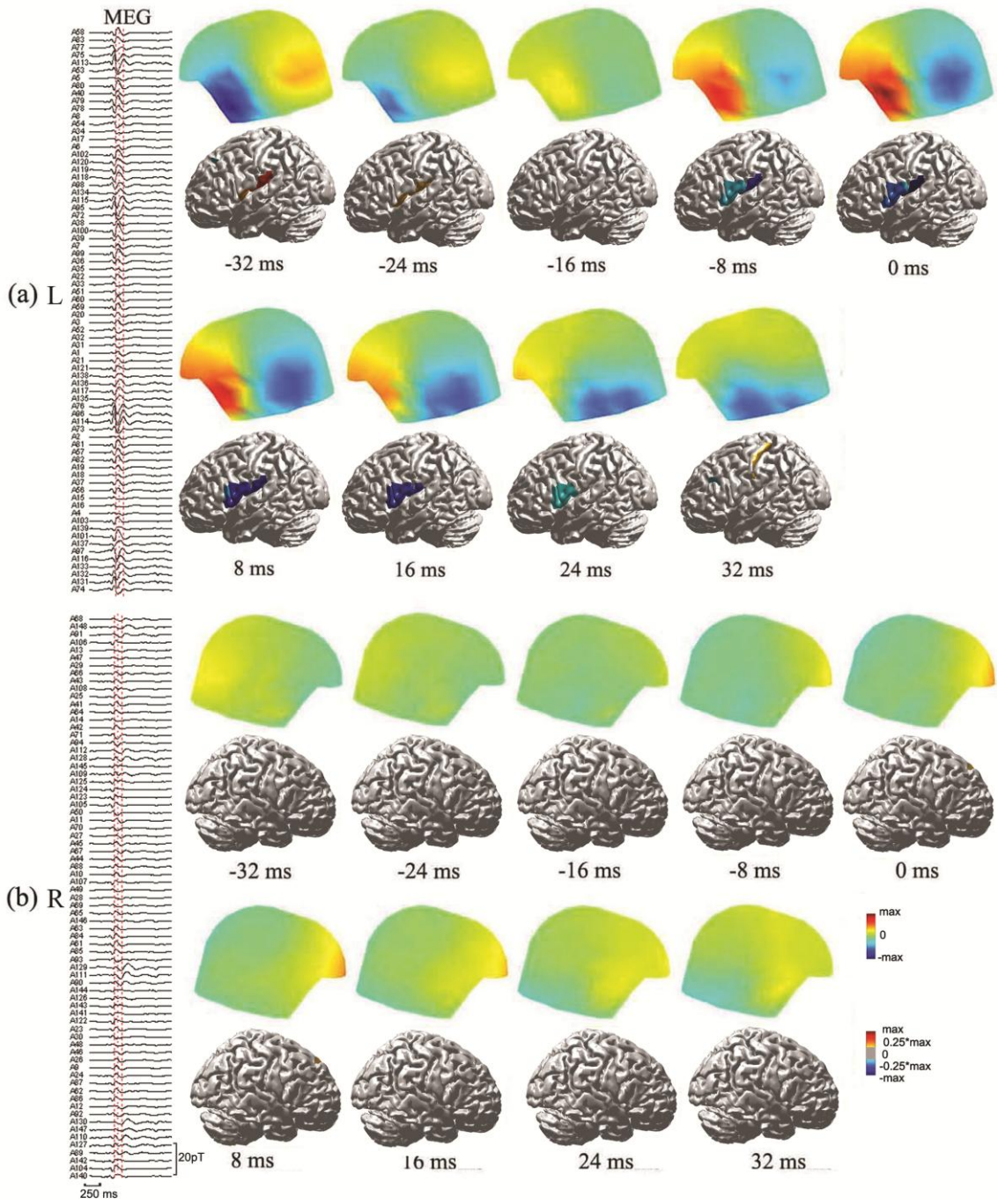

Figure 3.8 Patient 3: an example of in-hemisphere propagation
(a) IIS MEG waveforms from the left hemisphere, corresponding left views of magnetic fields, and reconstructed CCD maps from -32 ms to 32 ms. (b) Right views of same data in (a).

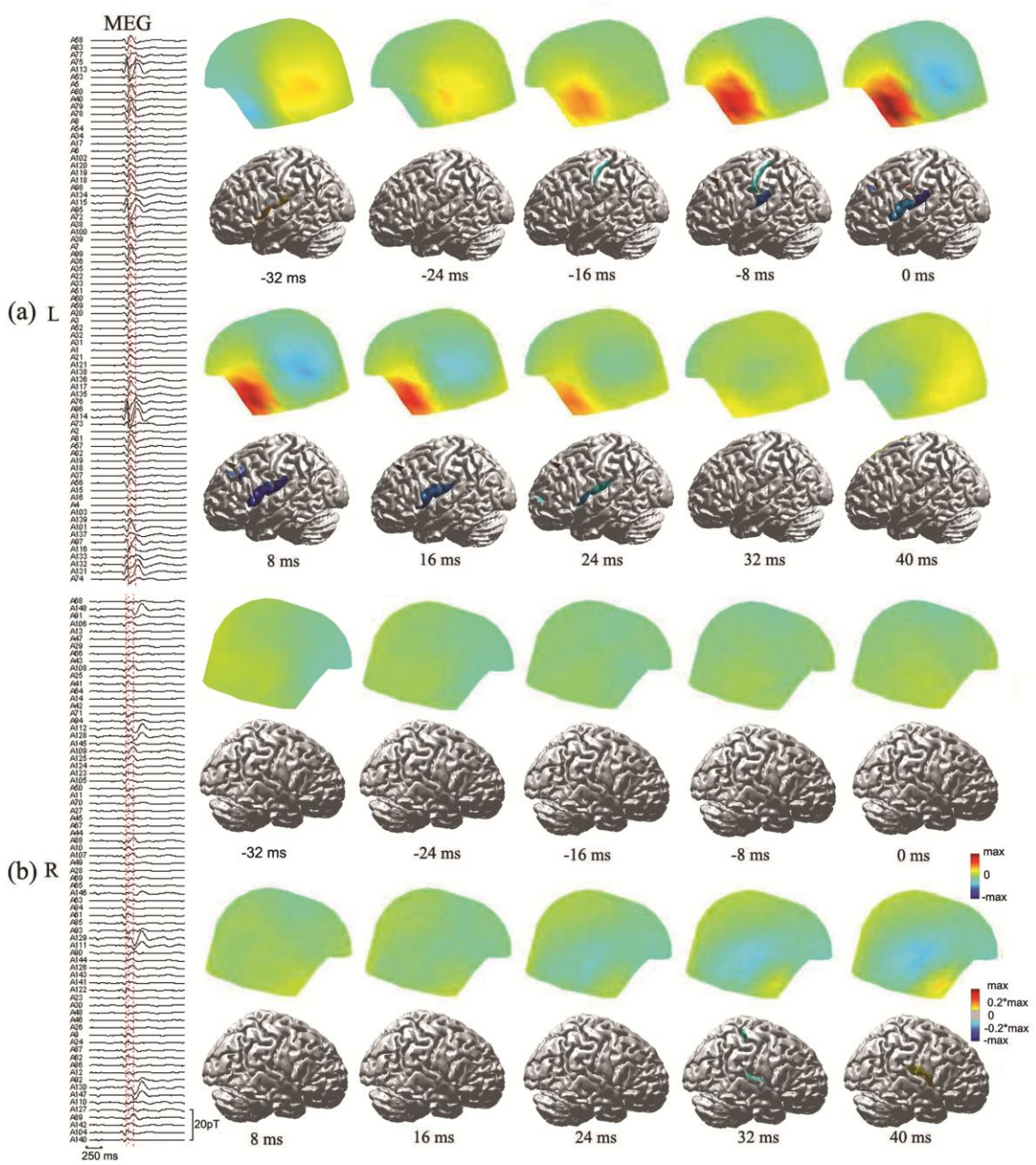

Figure 3.9 Patient 3: an example of slow cross-hemisphere propagation

(a) IIS MEG waveforms from the left hemisphere, corresponding left views of magnetic fields, and reconstructed CCD maps from -32 ms to 40 ms. (b) Right views of same data in (a).

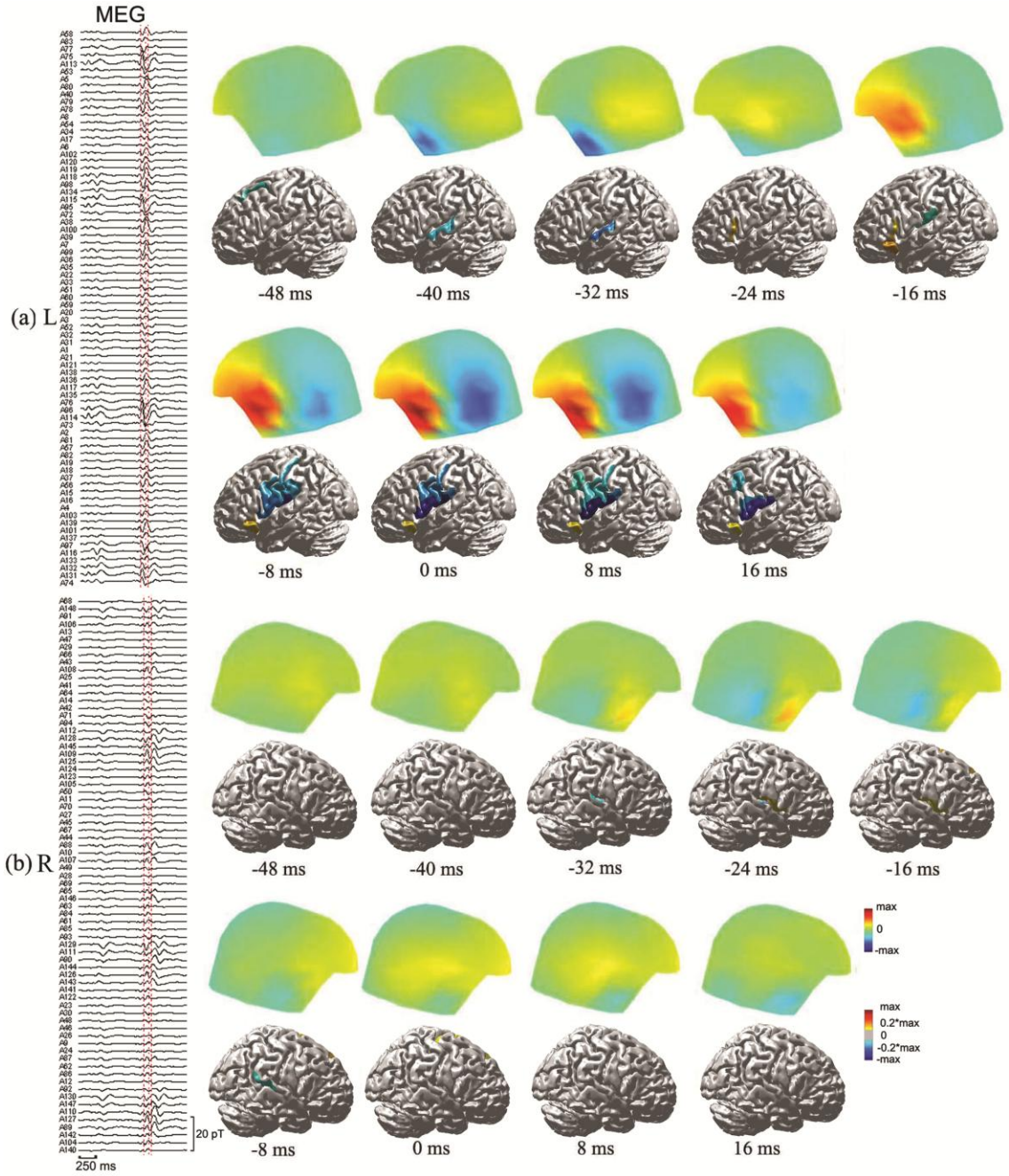

Figure 3.10 Patient 3: An example of fast cross-hemisphere propagation
(a) IIS MEG waveforms from the left hemisphere, corresponding left views of magnetic fields, and reconstructed CCD maps from -48 ms to 16 ms. (b) Right views of same data in (a).

3.4.5 Comparison of surface MEGs and cortical source maps

The active sources identified in CCD maps exhibit enhanced spatial resolution in identifying IZs as compared with scalp magnetic fields. For example, three CCD maps, each from one of the three patients, are illustrated in Figure 3.11. Each example suggests multiple cortical activations, which cannot be revealed by inspecting scalp MEGs. Furthermore, multiple cortical activations are present in most IISs: 21 out of 24 in Patient 1, 53 out of 55 in Patient 2, and 28 out of 29 in Patient 3. The enhanced spatial definition of cortical sources with CCD maps makes the inspection of temporal source dynamics within multiple activation areas more straightforward as illustrated in Figures 3.6-3.10.

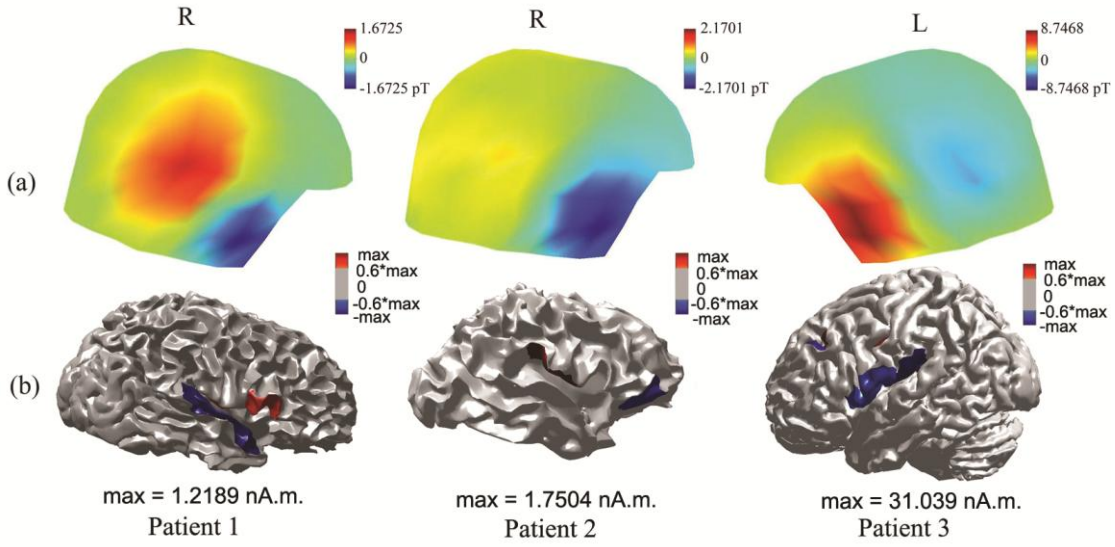

Figure 3.11 Comparison of magnetic fields and V-SSI sources
(a) Surface magnetic fields. (b) Reconstructed CCD maps.

3.5 Discussion and Summary

In this chapter, the variation based sparse source imaging method was applied to noninvasively identify irritative zones from interictal MEG data. Reconstructed cortical current densities from MEG interictal spikes revealed extended brain activations (Figures 3.1-3.11), which is consistent with previous observations that interictal spikes and seizures are generated by synchronously activated cortex over large areas (Tao et al., 2005; Ebersole and Hawes-Ebersole, 2007). It was demonstrated that cortical sources estimated from V-SSI are able to infer multiple brain activations and indicate their own extents at the same time (Figure 3.11), suggesting a much enhanced spatial resolution as compared to scalp magnetic fields. With these capabilities, the V-SSI approach is attractive in estimating the irritative zones with both location and extent information.

The V-SSI approach demonstrates a high spatial consistency in reconstructing spatial characteristics of epileptic sources. In 101 out of 108 IISs from three patients, sources that are consistent with MRI lesions, resections areas or clinical diagnosis were identified. In each patient, consistent sources were also identified from multiple IISs (Table 3.2). In Patient 1 with focal cortical dysplasia, reconstructed epileptic sources are mainly located on the right lateral sulcus, consistent with the location of MRI lesions (Figure 3.2(c-d)). Spatial consistency of epileptic sources in focal cortical dysplasia has been reported previously (Bautista et al., 2003). In Patient 2, distributed sources across multiple cortices are consistent, in terms of spatial coverage, with distributed multiple cortical tubers in MRI data (Figure 3.3(b-c)). Furthermore, in both Patients 1 and 2, neighboring areas of MRI lesions were identified as being involved in the generation of

IISs since brain tissues surrounding MRI visible lesions can be epileptogenic with high probability (Rosenow and Lüders, 2001). In Patient 3, involvement of Broca's and Wernicke's areas in the generation of IISs is well known in Landau-Kleffner syndrome (Landau and Kleffner, 1957; Rotenberg and Pearl, 2003).

The spatial comparisons were performed using quantitative approaches, such as statistical measures (active frequency and detection rate) to evaluate potential IZs and co-registration and visualization of multimodal data (MEG sources and MRI) in the same coordinates (Figures 3.2-3.4). With the quantitative measures, it also became possible to address which time segments in the IISs are more suitable for localizing epileptic sources. Some previous clustering methods used entire spikes to estimate location and extent of IZs (Shirashi et al., 2005). Some studies prefer results at spike peaks (Merlet and Gotman, 1999; Tanaka et al., 2009) due to high SNRs in the data. Many other studies observed that spike peaks may be poorly related to IZs because of propagation and thus concluded that the rising phase of spikes should provide more useful localizing information about the origins of epileptic discharges (Kaiboriboon et al., 2010). The results here from 108 IISs indicate that identification of sources suggesting possible IZs is more likely using MEG data from IIS rising phases (85.1% concordant results with pre-surgical evaluation over three patients) than data from IIS peaks (only 65.8% concordant results) (Table 3.2).

Moreover, V-SSI demonstrates a high temporal consistency in estimating temporal dynamics of epileptic sources, which is indicated by the continuity in changes of source extents and strengths over entire IISs (Figures 3.5-3.10). It has been shown (Ou et al., 2009) that time courses of sources obtained by concatenating instant inverse

source maps sequentially (especially with ℓ_1-norm regularization, such as SSI) usually exhibits discontinuities. Results from the V-SSI approach, otherwise, show much more consistency and continuity in source temporal dynamics (Figures 3.5-3.10). This is because of the implementation of variation as a spatial smoother, which stabilizes inverse solutions from being too sensitive to small changes from time to time. Moreover, explicit consideration of temporal continuity in EEG/MEG inverse solutions can further improve the performance in reconstructing source time courses (Huang et al., 2006; Ou et al., 2009; Gramfort et al., 2011).

In summary, I validated the V-SSI technique in clinical MEG data obtained from epilepsy in this chapter. It is suggested that the V-SSI technique has strong capability in estimating location and extent of irritative zones using interictal MEG spikes. Imaging data from three epilepsy patients successfully indicated irritative zones that are collaboratively supported by independent data from pre-surgical evaluations and post-surgery outcomes. Reconstructions of consistent and reliable source dynamics of interictal spikes provide valuable information about the development and evolvement of epileptic activity, and the inspection of such temporal information can significantly contribute to the understanding of clinical epilepsy.

Chapter 4: Wavelet Based Sparse Source Imaging

Although the ℓ_1-norm regularization implemented with variation transform, i.e. V-SSI, has yielded advancements in estimating extended epileptic sources in Chapter 3, one question remains is whether the cortical current density is sparse enough in the variation transform domain, or if can we find another sparse transform such that the cortical current density that can be even more compressible. It is well known that wavelets are a powerful tool for compressing signals or images (Mallat, 2009). Wavelet coefficients for many natural signals are mostly zero or negligibly small, which leads to sparse or compressible signal representations in the wavelet domain. This fact makes the wavelet transform promising to sparsely represent cortical current densities, which can be incorporated into ℓ_1-norm regularization methods to improve the performance of SSI. However, since the structure of the cortical surface is highly convoluted and irregular, wavelets defined on regular shaped spaces cannot be directly adopted to compress the cortical current density. Modified wavelets have been developed on arbitrary spaces in computer graphic and geometry applications, including Spherical wavelets (Schröder and Sweldens, 1995), irregular wavelets (Valette and Prost, 2004), and blending of linear and constant (BLaC) wavelets (Bonneau et al., 1996). Basis functions constructed from these wavelets can be numerically defined on triangular elements over irregular surfaces, which are supported either on triangular vertices (e.g. spherical and irregular wavelets) or faces (e.g. BLaC).

In this chapter, the highly convoluted cortical surface mesh is iteratively compressed to create a multi-resolution model. Given the multi-resolution model as the space for defining wavelet functions, a face-based wavelet is then developed by

designing scaling and wavelet basis functions at different resolution levels. The compressibility of cortical current densities using the face-based wavelet is tested on multiple randomly located sources and compared to a vertex-based wavelet, i.e. spherical wavelets (Schröder and Sweldens, 1995). Utilizing its compressibility, a novel sparse source imaging method is developed by integrating the proposed face-based wavelet with ℓ_1-norm regularization. Monte-Carlo simulations are conducted to evaluate the performance of the proposed approach with comparison to a vertex-based wavelet method. MEG data from a language task are also adopted to evaluate the feasibility of the wavelet based sparse source imaging technique. The wavelet based sparse source imaging algorithm was developed by me and a post-doc fellow, Ke Liao, in our Lab, and this algorithm has already been published in Physics in Medicine and Biology in 2012 (Liao et al., 2012). Some of the results presented in this chapter have been included in the proceedings of the IEEE EMBS conference in 2013 (Ding et al., 2013b) and the proceedings of the IEEE NER conference in 2013 (Zhu et al., 2013a).

4.1 The Face-based Surface Wavelet

4.1.1 Multi-resolution Model

In order to define the wavelet transform on the cortical surface, a multi-resolution cortical model is constructed by iteratively compressing the highly convoluted cortical structure to create a series of spaces for multi-resolution wavelet analysis (Valette and Prost, 2004). The compression procedure is accomplished by hierarchically merging multiple triangles on a fine level into one triangle on a coarse level. An instance of a multi-resolution cortical model is given in Figure 4.1.

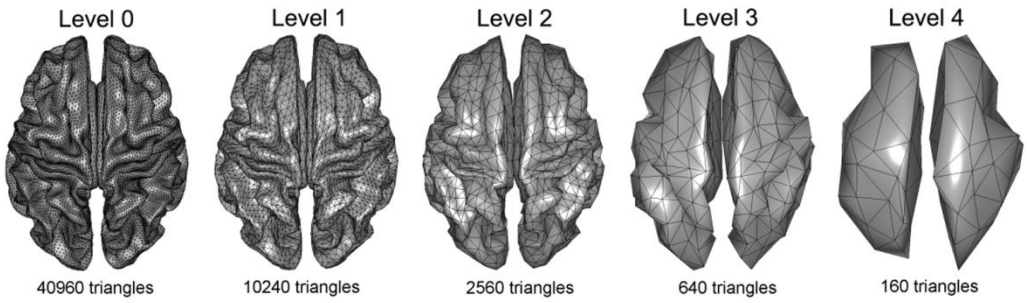

Figure 4.1 One example of a multi-resolution model

A group of merging patterns, including four triangles to one triangle (4-to-1), three triangles to one triangle (3-to-1), two triangles to one triangle (2-to-1), and one triangle to one triangle (1-to-1), are maintained as code books (Valette and Prost 2004). Merging of triangles starts by selecting an arbitrary triangle at the finest level mesh (i.e. the original cortical mesh) as the seed and the first merging occurs at the seed triangle and its three neighbored triangles using the 4-to-1 merging pattern. During this merging process, three vertices that are shared by the seed triangle and its neighbors are removed, noted as "child vertices", while the other three are kept, noted as "parent vertices". By connecting "parent vertices", these four triangles are merged into a new triangle. Similar merging processes then spread from finished merging sets to surrounding triangles by selecting proper merging patterns from code books defined above. The 4-to-1 merging pattern has the priority in the merging process since it has the highest merging rate. Merging patterns that can be used for surrounding triangles are dependent on removed "child vertices" and remaining "parent vertices" in the previous steps and cannot always be 4-to-1 patterns. Under such conditions, 3-to-1, 2-to-1, or 1-to-1 merging patterns from code books are selected with decreasing priorities. This merging process is progressively repeated until all triangles on the fine level are

covered and a new mesh at the coarse level is created. The new mesh is then treated as the fine mesh to create the next coarse mesh and the entire procedure is iteratively applied to create a multi-resolution model.

4.1.2 Face-based Wavelet Transform

Given the multi-resolution cortical model, the scaling function φ_i^m supported on the *i*th triangle (denoted as T_i^m) at level *m*, is designed as one on triangle T_i^m and zeros otherwise. Then, scaling functions φ_j^{m+1} (*j* is the index of scaling functions) and wavelet functions ${\psi_k}^{m+1}$ (*k* is the index of wavelet functions) at the coarse level *m*+1 are computed from the linear combination of the scaling functions at level *m* weighted by synthesis coefficients $p_{i,j}^m$ and $q_{i,k}^m$ (Bonneau et al., 1996)

$$\varphi_j^{m+1} = \sum_i p_{i,j}^m \varphi_i^m, \qquad \psi_k^{m+1} = \sum_i q_{i,k}^m \varphi_i^m. \tag{4.1}$$

Similarly, scaling functions φ_i^m at level *m* can be decomposed into the linear combinations of scaling functions φ_j^{m+1} and wavelet functions ${\psi_k}^{m+1}$ at coarse level *m*+1 weighted by analyses coefficients $a_{i,j}^m$ and $b_{i,k}^m$ (Bonneau et al., 1996) according to

$$\varphi_i^m = \sum_j a_{j,i}^m \varphi_j^{m+1} + \sum_k b_{k,i}^m \psi_k^{m+1}. \tag{4.2}$$

Since both scaling and wavelet functions are supported on surface triangles, this approach is named face-based wavelets, to be distinguished from other vertex-based wavelets, e.g., spherical wavelets (Schröder and Sweldens 1995).

For convenience, let $\mathbf{A}^m$, $\mathbf{B}^m$ denote analysis matrices containing analyses coefficients $a_{i,j}^m$ and $b_{i,k}^m$. Details on how to calculate these analyses coefficients and

construct analysis matrices can be found in Appendix A. Given the analyses matrices, functions x^m defined on a fine level *m* can be compressed into scaling coefficients x^{m+1} and wavelet coefficients y^{m+1} on a coarse level *m+1*:

$$\begin{cases} x^{m+1} = \mathbf{A}^m x^m, \\ y^{m+1} = \mathbf{B}^m x^m. \end{cases} \tag{4.3}$$

The wavelet transform matrix $\mathbf{W}_m$ at level *m* is thus straightforward to be derived by iteratively performing analysis procedures (Liao et al., 2012):

$$\mathbf{W}_m = \begin{bmatrix} (\mathbf{G}^m)^{1/2}\mathbf{A}^{m-1}\mathbf{A}^{m-2}\cdots\mathbf{A}^0 \\ \mathbf{B}^{m-1}\mathbf{A}^{m-2}\cdots\mathbf{A}^0 \\ \vdots \\ \mathbf{B}^1\mathbf{A}^0 \\ \mathbf{B}^0 \end{bmatrix}, \tag{4.4}$$

where $\mathbf{G}^m$ is the Gram-Schmidt matrix (Bonneau et al., 1996), i.e. a diagonal matrix with its diagonal elements being areas of triangles on the cortical mesh at level *m*. The superscript 0 denotes the cortical surface at the finest resolution (i.e. the CCD model).

4.1.3 Wavelet-based Sparse Source Imaging

Given the wavelet transform designed on the CCD model, the wavelet-based sparse source imaging (W-SSI) algorithm can be easily derived by modifying the model term $L(\bar{s})$ in Equation (2.2) as the ℓ_1-norm of the wavelet coefficients to obtain the optimization problem:

$$\min \left\| \mathbf{W}_m \bar{s} \right\|_1 \quad \text{subject to} \quad \left\| \vec{\phi} - \mathbf{A}\bar{s} \right\|_2 < \beta, \tag{4.5}$$

where *m* denotes the compression level for the face-based wavelet. Similar to Equation (3.3), the convex optimization problem in Equation (4.5) can be recast as a SOCP (Lobo

et al., 1998) and solved by a Matlab package named SeDuMi (Sturm, 1999), resulting in the equivalent problem

$$\min_{\vec{s}} \sum_{k=1}^{N} g_k \text{ subject to } \vec{n} = \vec{\phi} - \mathbf{A}\vec{s} \text{ ; } \|\vec{n}\|_2 \le \beta \left\| \sum_{l=1}^{N} w_{kl} s_l \right\|_2 \le g_k \quad k = 1, 2, \cdots, N, \tag{4.6}$$

where w_{kl} are elements in the wavelet transform matrix $\mathbf{W}_m$. Intermediate parameters g_k (non-negative) are introduced as upper bounds for the ℓ_1-norms of the wavelet coefficients. N is the number of triangles in the CCD model. The estimation of the regularization parameter β is as the same as in Section 3.1.

4.2 Performance Analysis Using Simulated Data

4.2.1 Simulation Protocol

The CCD model of the cortical surface is obtained by segmenting structural MRI data from an averaged subject in FreeSurfer's sample data set (http://surfer.nmr.mgh.harvard.edu) and a multi-resolution model is then constructed with four compression levels as shown in Figure 4.1. Seed triangles on the CCD model are randomly selected and gradually merged with neighboring triangles to grow extended patches that simulate cortical sources with certain extents. Dipole moments within each simulated source patch are computed as the multiplication of triangular area and dipole moment density (i.e. 100pAm/mm^2). Simulations were conducted 200 times in order to cover most parts of the brain. To investigate compressibility of these cortical patch sources using the proposed face-based wavelets, sources synthesized from wavelet coefficients thresholded to reach 10% coefficient ratio (CR) (which is defined as the ratio between the number of non-zero coefficients after thresholding and the number of active elements in the original source domain) were evaluated by metrics of

area under receiver operating characteristic (ROC) curves, i.e. AUC (Metz et al., 1973), and relative minimum square error (RMSE) (Grova et al., 2006). Detailed equations for computing AUC and RMSE can be found in Appendix B. Complexities of brain activities involving simultaneous activations were also considered in simulations with different numbers of cortical sources (i.e., 1, 2, 3, 5 and 10).

To evaluate the performance of W-SSI, MEG measurements were simulated based on a 148-channel MEG system as generated by two simultaneous activations (i.e. two randomly located cortical patch sources as discussed above). A three-compartment BE model was built to model three major tissues (the scalp, skull, and brain) of different conductivity (0.33/Ω.m, 0.0165/Ω.m, and 0.33/Ω.m) (Lai et al., 2005) for the calculation of the forward problem (Baillet et al., 2001). MEG measurements were then contaminated by Gaussian white noise with signal to noise ratio (SNR) as 20dB. The performance of the ℓ_1-norm regularization using the face-based wavelet is compared to the ℓ_1-norm regularization using vertex-based wavelets, i.e. Spherical wavelet, in recovering EEG/MEG sources at multiple compression levels (from one to three). Performance was assessed using metrics of AUC from detection theory (Metz et al., 1973), spatial dispersion (SD) (Molins et al., 2008) and distance of localization error (DLE) (Molins et al., 2008). Detailed formulae for SD and DLE can be found in Appendix B.

4.2.2 Synthesis Performance

Figure 4.2 shows the synthesis performance of the face-based wavelet method at different compression levels using different numbers of sources (1, 2, 3, 5 and 10) with the same CR (10%). As indicated in the AUC metric (Figure 4.2(a)), the two-level,

three-level, and four-level wavelet compressions have high synthesis accuracies at about 0.95 after thresholding across all conditions with different numbers of sources. The one-level compression has the worst AUC values, which are still around 0.7, even in the case of 10 simultaneously active and randomly located sources. The overall performance indicated by the RMSE metric (Figure 4.2(b)) shows that, for different numbers of sources, three-level and four-level compression yielded the smallest RMSE values. Examples with three simulated cortical sources are provided in Figure 4.2(c) for visual inspections of synthesized sources at different compression levels. The spatial

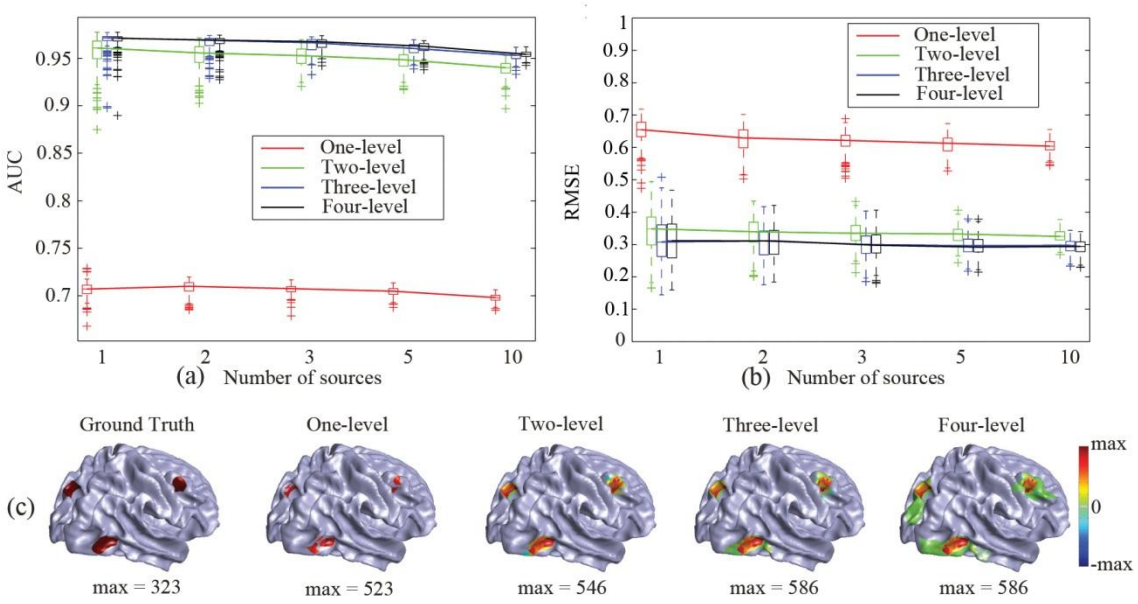

Figure 4.2 Synthetic performance of the face-based wavelet analysis
Performance of the face-based wavelet analysis at different compression levels with different number of sources (1, 2, 3, 5 and 10). (a) AUC. (b) RMSE. (c) An example of three sources and its synthesized results at levels one to four.

of the sources from the one-level compression is smaller than the simulated ones, while sources from the three-level and four-level compressions are smoothed, which explains their higher AUC values since the AUC metric favors smooth distributions.

4.2.3 Vertex-based vs. Face-based Wavelets

Figure 4.3 compares the performance of ℓ_1-norm regularization methods with the proposed face-based wavelet and the vertex-based Spherical wavelet in inverse source reconstructions. Reconstructed cortical current densities are displayed with thresholding 20% of individual maxima. Although the face-based wavelet indicates worse AUC values than the vertex-based wavelet at the two-level and three-level

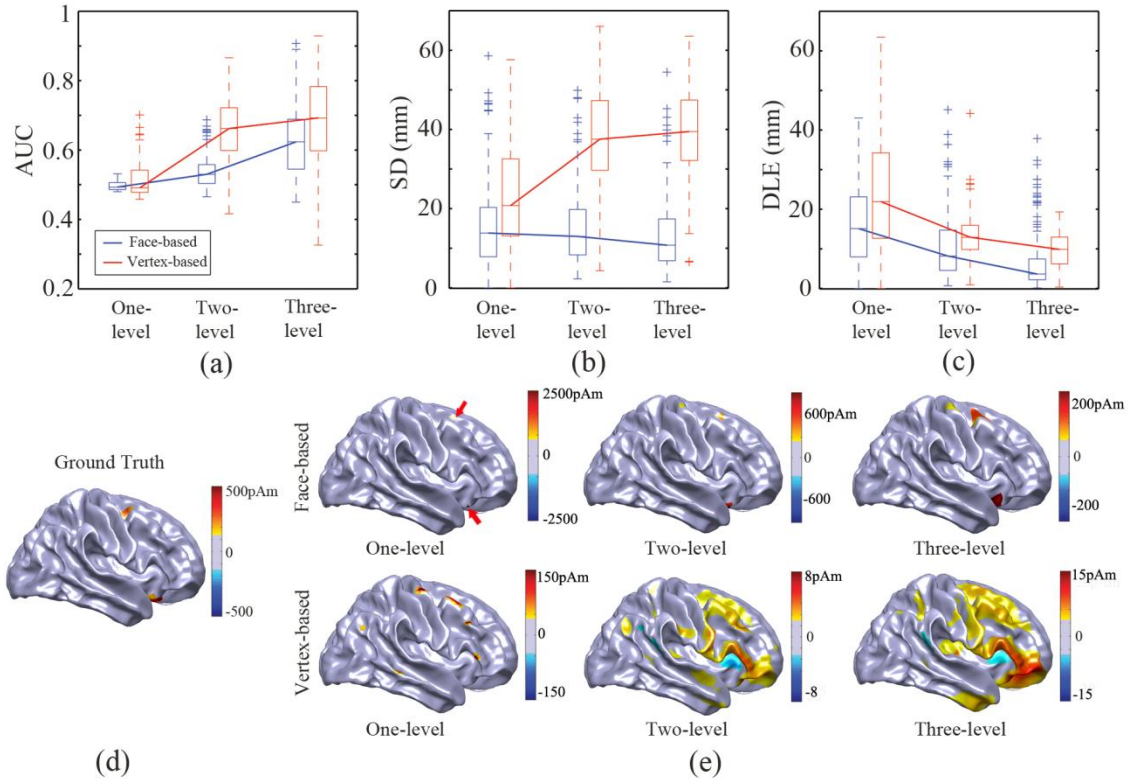

Figure 4.3 Inverse performances of face-based and vertex-based wavelet methods
(a) AUC. (b) SD. (c) DLE. (d) An example of two non-uniform sources. (e) Estimated sources in (d) using two methods at levels one to three.

compressions, it has significantly lower DLE values indicating fewer localization errors and significantly lower SD values with fewer errors in estimating source extents. The reason for the relatively high AUC values from the vertex-based wavelet is that the AUC metric favors smooth distributions (Figure 4.2). It is evidenced by the given

example in Figure 4.3(e) that the ℓ_1-norm regularization with the vertex-based wavelet produces much smoother results as compared with the ℓ_1-norm regularization using the face-based wavelet. Visual inspection shows that the reconstructed sources from the vertex-based wavelet are actually worse than those obtained from the face-based wavelet.

4.3 Performance Analysis Using Experimental Data

4.3.1 Language Data

To test the performance with experimental data, the ℓ_1-norm regularization method with the proposed face-based wavelet was tested with MEG recordings while a subject performed a language task. One epilepsy patient performed an auditory word recognition task with the same protocol as Doss et al. (2009) during pre-surgical evaluation at United Hospital, St. Paul, MN. The language task used a continuous recognition memory paradigm (Breier et al., 1998; Papanicolaou et al., 2004). It consisted of 90 abstract English nouns, with 30 of them as targets and the remaining 60 words as distractors. The target words were presented once before MEG recordings and the patient was instructed to remember as many of them as possible. During MEG recording sessions, target words were mixed with distractors and presented randomly, and the patient was asked to lift their index finger when a target word was detected. MEG recordings were acquired using the same 148-channel MEG system as in Section 3.2. After applying the band-pass filter of 0.1-20Hz and baseline correction using pre-stimulus data, epochs were averaged to produce the event-related field (ERF). Sources were analyzed using both spherical wavelets and face-based wavelets during a time

window of 200-300ms post-stimulus, which was reported to be associated with early auditory and language processing (Breier et al., 1998).

Reconstructed cortical current sources underlying the MEG data from the language task are shown in Figure 4.4. Magnetic scalp maps at 232ms post-stimulus indicate that possible current sources originate from both hemispheres but are more dominant on the right side. Cortical current sources were reconstructed from magnetic fields using spherical wavelet (vertex-based) and face-based wavelets via ℓ_1-norm regularizations. The display threshold for cortical sources was set as 10% of individual maxima. Dominant activities were observed in the right superior and medial temporal

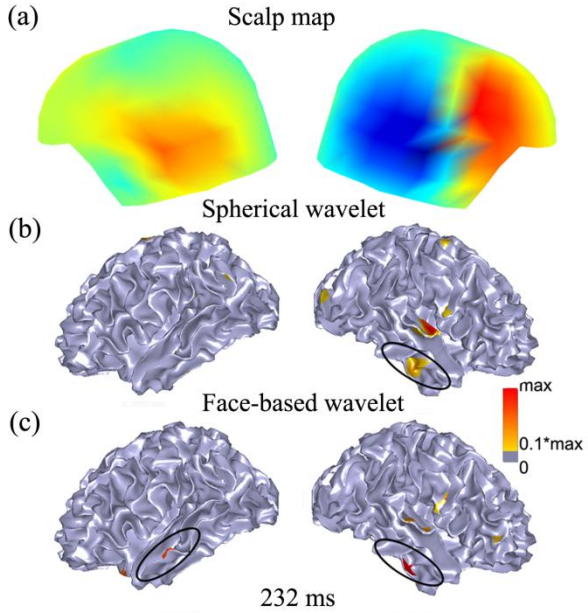

Figure 4.4 Comparison of face-based and vertex-based wavelet methods in language data

(a) MEG scalp map. (b), (c) Sources from spherical and face-based wavelet at the analysis level of three.

regions in both methods, while the left medial temporal activations were only observed in the face-based wavelet method. The temporo-parietal activation and bilateral medial temporal activations are supported by the literature (Breier et al., 1998) for the

auditory induced early language processing around 200-300ms, which are believed to be associated with decoding of phonological and sematic components of words.

4.3.2 Epilepsy Data

The proposed wavelet-based sparse source imaging was further applied to identify the irritative zones for three epilepsy patients. Interictal MEG recordings were visually inspected by experienced doctors from MEG/MSI center at Minnesota Epilepsy Group, St. Paul, MN to select epileptic interictal spikes. MRI lesions were also identified and marked by the doctors. Band-pass filtering of 3-30 Hz was performed and IISs without obvious artifacts (e.g. heartbeats, muscle movements or eye blinks) were selected for source analysis using the W-SSI technique.

Patient 1 (Table 3.1) had extensive cortical development disorder in the right temporo-parietal areas. Multiple heterotopias identified on the MRI were located in the right posterior temporal and parietal regions (Figure 4.5(b)). A total of 23 IISs were selected for source analysis. As shown by one IIS shown in Figure 4.5(a, c), MEG scalp maps implied a possible origin from the right temporal lobe, and their corresponding sources from W-SSI show a focal activation on the junction region between the right superior temporal and parietal areas during the interval from -12ms to 12ms around the spike peak (0ms). The posterior temporal sources were observed in all 23 IISs, which were located within the surrounding areas of MRI lesions marked by the doctor (Figure 4.5(b)). Moreover, taking advantage of the high temporal resolution of MEG, dynamic changes of cortical sources with an interval of 6ms indicate an increase of source strengths before the IIS peak and a decrease after the peak, which is also consistent with the strength changes in the MEG scalp maps. It is also worth noting that weak

activations observed at 0ms and 12ms imply that epileptic activities may spread to extensive areas close to or far away from the origins.

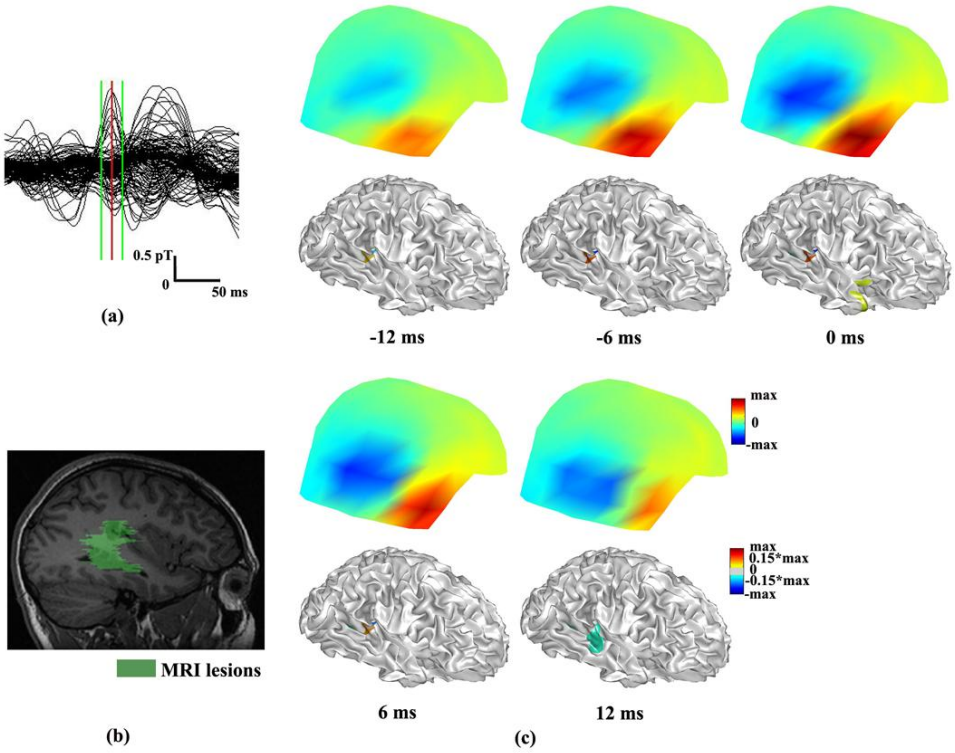

Figure 4.5 Reconstructed epileptic sources in Patient 1
(a) One example of MEG interictal spikes. The red line indicates the spike peak at 0 ms and the two green lines indicate the time interval from -12ms to 12ms. (b) MRI lesions (in green). (c) MEG scalp maps and cortical sources estimated from the W-SSI technique.

Due to the low quality of MRI in Patient 2, the segmentation of cortical surface was not satisfactory for performing the wavelet compressions at multiple resolutions. The W-SSI approach was thus applied to MEG IISs collected from Patient 4. This patient (28 years old, male) was diagnosed with left mesial temporal sclerosis (MTS) and suffered from daily multiple complex partial seizures. After a left temporal lobectomy, the patient was seizure free. Figure 4.6(b) is the post-operative MRI showing resected areas on the left temporal lobe. A total of 17 IISs were selected for

performing source analysis using W-SSI. Underlying one IIS from this patient, MEG scalp maps show a focus on the left temporal lobe, and estimated cortical sources from W-SSI indicate activations on the left middle temporal gyrus from -16ms to 16ms. Estimated sources from other IISs were also observed within the left middle temporal gyrus or at its surrounding areas. It is observed that the left middle temporal gyrus is included in the resection areas indicated by the post-operative MRI in Figure 4.6(b). The strengths of cortical sources increase first before reaching the IIS peak and then decrease after the peak.

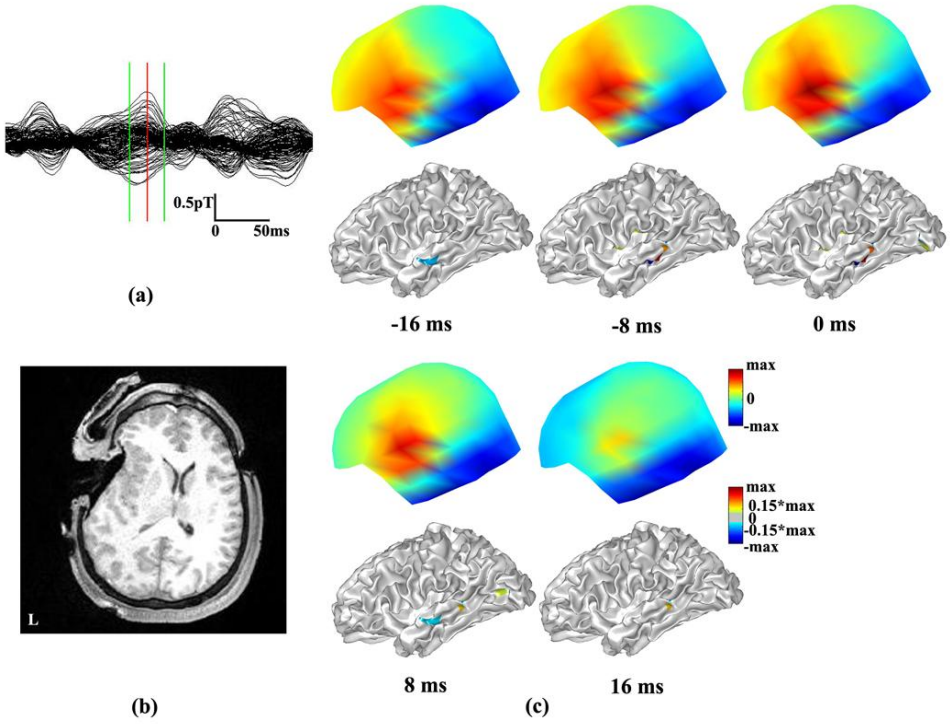

Figure 4.6 Reconstructed epileptic sources in Patient 4
(a) One example of MEG interictal spikes. The red line indicates the spike peak at 0 ms and the two green lines indicate the time interval from -16ms to 16ms. (b) Post-operative MRI. (c) MEG scalp maps and cortical sources estimated from W-SSI.

Patient 3 (Table 3.1) was diagnosed as Landau-Kleffne syndrome (Table 3.1). No MRI lesion was found for this patient. Large MEG amplitudes were observed in all

29 selected IISs. One example of an IIS is shown in Figure 4.7(a). MEG scalp maps from one IIS indicate activations on the left frontal and temporal regions (Figure 4.7(b)). The left frontal and temporal sources were found in all 29 IISs. A series of estimated cortical sources from W-SSI with an 8ms interval shows that activations started from the left posterior of temporal gyrus (close to the auditory cortex) at -8ms to the inferior frontal gyrus (part of language cortex) at 24ms. It is noted that rather than peri-sylvian sources, two other activation sites with relatively weak strengths were observed at the anterior central gyrus.

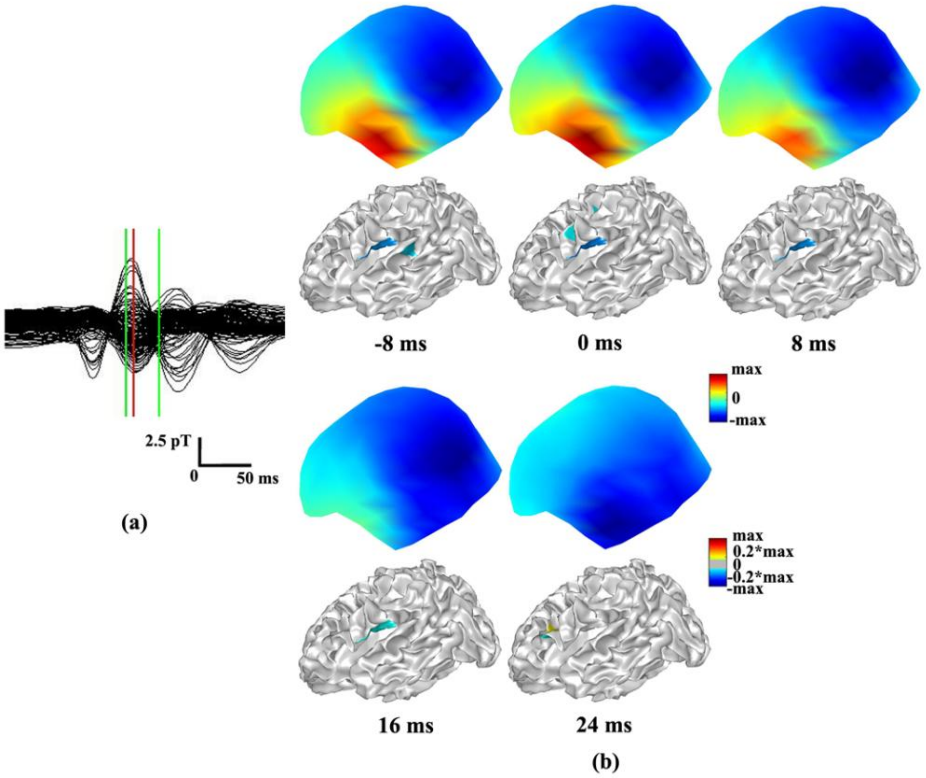

Figure 4.7 Reconstructed epileptic sources in Patient 3
(a) One example of MEG interictal spikes. The red line indicates the spike peak at 0 ms and the two green lines indicate the time interval from -8ms to 24ms. (b) MEG scalp maps and cortical sources from W-SSI.

4.4 Discussion and Summary

In this chapter, I proposed a novel face-based wavelet approach to provide a sparse representation of cortical current densities. Simulation results demonstrated that the proposed face-based wavelet transform is capable of compressing cortical current densities into a few nonzero coefficients without a significant reduction in the synthetic accuracy. Compressions with multiple resolutions can be achieved by applying the face-based wavelets at different analysis levels (e.g. one to four levels). Synthetic accuracy of the one-level wavelet analysis is relatively low, with an AUC of around 0.7, while the performance improves when increasing the analysis level from one to two. However, the improvement from the two-level analysis to the four-level analysis is very limited. At levels of three and four, syntheses from coefficients with 10% CR achieve the highest performance as measured by AUC of around 0.95 and a RMSE around 0.3 (Figure 4.2(a)). Comparing performance at the same analysis level, the flat trends of median values of both AUC and RMSE across different numbers of sources imply that the synthetic accuracy is not sensitive to the number of brain activation sites.

With excellent compression ability, the proposed face-based wavelet is then implemented within the ℓ_1-norm regularization framework to solve the EEG/MEG inverse source reconstruction problems. Simulation results with two randomly located sources suggest that the inverse solver integrated with the proposed face-based wavelets has better performance than the inverse solver integrated with the vertex-based wavelets in terms of source localization accuracy (evaluated by SD and DLE) and source extent estimation accuracy (evaluated by SD) (Figure 4.3(a-c)). The relatively higher AUC values from the vertex-based wavelet are due to smoothed reconstructions, as visualized

from examples given in Figure 4.3(e). When increasing the number of wavelets analysis levels, all metrics (AUC, SD and DLE) indicate improved performance for the face-based wavelet method, while increased SD values in the vertex-based method imply more severe blurredness in the inverse solutions.

In the analysis of experimental data from a language task, the ℓ_1-norm regularization with the face-based wavelets further demonstrates their ability in reconstructing multiple simultaneous brain activation sites by successfully detecting bilateral symmetrical medial temporal activation, while the ℓ_1-norm regularization with the vertex-based wavelets failed to detect the left medial temporal source. The ℓ_1-norm regularization with the proposed novel face-based wavelets will benefit the identification of eloquent cortical areas corresponding to higher cognitive functions, e.g. language processing, which usually involve multiple brain regions (Breier et al., 1998).

In the analysis of epilepsy data from three partial epilepsy patients, reconstructed sources by W-SSI from interictal MEG spikes were compared to clinical routine pre-surgical evaluations and resection areas when possible. In Patient 1, W-SSI indicated possible epileptic sources from neighboring cortices close to the MRI lesions (Figure 4.5(b)), since brain tissues surrounding visible lesions are usually also epileptogenic (Rosenow and Lüder, 2001). In Patient 4, epileptic sources estimated by W-SSI were quite consistent with resected brain tissues in the temporal lobectomy in terms of location, while the extent seems to be smaller (Figure 4.6(b)). It is usually the case that typical temporal lobectomies may include extensive resections up to 6.5cm (Wiebe et al., 2001). Although there were no visible MRI lesions for Patient 3, W-SSI was able to detect epileptic origins from perisylvian regions. Similar peri-sylvian

generators in LKS patients were identified in Chapter 3 (Figures 3.8-3.10). The involvement of auditory and language cortices during epileptic discharges may explain the language ability loss in LKS patients (Rotenberg and Pearl, 2003). Examples of IISs in Patient 1 and Patient 4 both indicated an increase of source strengths before reaching the peak and a decrease after the peak (Figures 4.5(c), 4.6(c)). The strength change of cortical sources during IISs has also been observed in intracranial recordings (Doss et al., 2009). Activations at areas surrounding or away from the primary focus were observed at the spike peak in both Patient 1 and 3 (Figures 4.5(c), 4.7(b)), which implies that cortical activity underlying spike peaks may have already spread and thus are not ideal for estimating the origins of epileptic discharges. The propagation pattern from auditory cortex to language cortex in Patient 3 indicates that the epileptic activities for LKS patients may firstly interfere with the auditory processing and then language comprehension areas (Wiebe et al., 2001).

In summary, I developed a wavelet-based sparse source imaging method for application to epilepsy data. A feasible sparse representation of cortical current activities was achieved using the proposed face-based surface wavelets. By integrating the surface wavelets with the ℓ_1-norm regularization, a novel wavelet based sparse source imaging (W-SSI) was developed. It was demonstrated that the W-SSI technique can achieve improved reconstruction accuracy of source locations and extents in both simulations and real experimental recordings. The W-SSI technique is thus promising to inspect complex brain activations of significant importance in estimating eloquent cortices and epileptogenic zones for epilepsy surgery.

Chapter 5: Sparse Source Imaging Using Multiple Transforms

The variation transform introduced in Chapter 3 is used to compress cortical current densities by computing differences between two neighboring currents. If we treat the variation transform as a first-order derivative, then Laplace transform may be interpreted as a second-order derivative, which also can be used as a transform domain where current densities can be compressed (Chang et al., 2010). However, since the minimization of both variation and the second-order derivative do not limit the global energy of inverse solutions, ℓ_1-norm regularizations with these transforms must incorporate additional priors to constrain the global energy. The face-based wavelet transform introduced in Chapter 4 is an efficient tool for compressing current densities on highly convoluted cortical surfaces, i.e. CCD models (Chang et al., 2010; Liao et al., 2012). It has been further indicated that the ℓ_1-norm regularization using the face-based wavelets has better accuracy in recovering sources than the vertex-based wavelets, i.e. spherical wavelets (Chang et al., 2010). Furthermore, it has been suggested that adaptive estimation of source extents of both focal and extended sources is possible by controlling the level of wavelet compression (Chang et al., 2010), which is, however, challenging without *a priori* knowledge about the size of the sources.

In this chapter, a new sparse source imaging method, variation and wavelet based SSI (VW-SSI), is proposed using multiple penalties in ℓ_1-norm that force sparseness in both the variation and wavelet domains. This approach aims to address the limitation in the variation-based method since the wavelet penalty term constrains the global energy, and to stabilize the issue of selecting the wavelet compression level with the variation penalty term. With the hybrid sparseness constraints integrated, it is

expected that SSI techniques can achieve better accuracy in estimating source locations and extents, even in data with low signal-to-noise ratio (SNR). The performance of the proposed method is evaluated in simulated and experimental MEG data. In simulation, neural activation levels of various extents are randomly located. The VW-SSI inverse solutions are assessed using multiple metrics on the accuracy of both locations and extents, as compared with other SSIs and ℓ_2-norm methods. The sensitivity of VW-SSI to SNR, wavelet compression level, and hyper-parameter for multiple penalty terms are studied. Experimental MEG data collected from both language and motor tasks in an epilepsy patient are analyzed to evaluate and compare all methods in reconstructing distributed neural activations. The proposed ℓ_1-norm regularization method based on multiple transform sparseness and its validation results have been published in NeuroImage in 2013 (Zhu et al., 2013b).

5.1 Variation and Wavelet Based Sparse Source Imaging

The proposed VW-SSI method integrates both variation and wavelet transforms in the ℓ_1-norm regularization and results in the optimization problem

$$\min \left\| \mathbf{V}\bar{s} \right\|_1 + \lambda \left\| \mathbf{W}_m \bar{s} \right\|_1 \quad \text{subject to} \quad \left\| \vec{\phi} - \mathbf{A}\bar{s} \right\|_2 < \beta, \tag{5.1}$$

where λ>0 is the hyper-parameter to balance the variation and wavelet penalties. The notations $\bar{s}$, $\vec{\phi}$, **A**, and β are as same as in Equations (2.1)-(2.2). **V** denotes the variation transform matrix, which is defined in Equation (3.1). $\mathbf{W}_{\mathrm{m}}$ is the surface based wavelet transform matrix at level *m*, which is defined in Equation (4.4).

By introducing intermediate variables, Equation (5.1) is readily cast as a second-order cone program (SOCP) (Lobo et al., 1998) according to

$$\min_{\vec{s}} \sum_{i=1}^{P} f_i + \lambda \sum_{k=1}^{N} g_k \qquad \text{subject to } \vec{n} = \vec{\phi} - \mathbf{A}\vec{s}\ ;\ \|\vec{n}\|_2 \le \beta\ ;$$

$$\left\| \sum_{j=1}^{N} v_{ij} s_j \right\|_2 \le f_i \quad i = 1, 2, \cdots, P\ ; \left\| \sum_{l=1}^{N} w_{kl} s_l \right\|_2 \le g_k \quad k = 1, 2, \cdots, N, \tag{5.2}$$

where v_{ij} and w_{kl} are elements in **V** and **W**, respectively. Sums of elements f_i, g_k (non-negative) in vectors $\vec{f}$, $\vec{g}$ serve as upper bounds for the ℓ_1-norms of the variation and wavelet coefficients. A Matlab package SeDuMi (Sturm, 1999) was used to solve the SOCP problem in Equation (5.2).

5.2 Performance Analysis Using Simulated Data

5.2.1 Simulation Protocol

An averaged structural MRI from FreeSurfer (http://surfer.nmr.mgh.harvard.edu) was used to build the CCD model and head volume conductor model for simulations. The cortical surface was segmented at the interface of the gray and white matter and tessellated into 40,960 triangles, each of 3.23±1.14mm^2 (mean±SD) using FreeSurfer (Dale et al., 1999). A BEM model was used as the realistic head volume conductor, consisting of the scalp, skull and brain with conductivities of 0.33/Ω.m, 0.0165/Ω.m, and 0.33/Ω.m (Lai et al., 2005), respectively.

To perform the wavelet based algorithms (W-SSI and VW-SSI), the original cortical mesh with 40960 triangles was iteratively compressed into four coarse meshes with 10240, 2560, 640, and 160 triangles, respectively, to form a multi-resolution model. Cortical current densities ($\vec{s}$) as functions defined on the finest level can thus be analyzed by applying the face-based wavelet transform.

To mimic brain activations from synchronized neuronal populations

(Hämäläinen et al., 1993), cortical patch sources were formed using region growing technique by randomly selecting a seed triangle and iteratively merging its neighbors. The extent degree *x* is defined as an indicator of the size of patch source that include *x* iterations of merging neighboring triangles. Patch sources were simulated with varied source extents (extent degrees 3, 5, 7, 9, 11 with corresponding extents 2.34±0.38cm^2, 7.68±1.06cm^2, 16.11±2.10cm^2, 27.47±3.49cm^2, 41.21±5.23cm^2). Cortical current densities ($\vec{s}$) were simulated with varied numbers of patch sources (i.e. 1, 2, 3, 5) and each cortical current density with the same number of sources was repeated 200 times, in which sources were randomly selected. The dipole amplitude at each triangle was simulated as a multiplication of its triangular area with the dipole moment density of 100pAm/mm^2 (Jerbi et al., 2004). MEG signals were computed by first solving the forward problem using the BE volume conductor model (Mosher et al., 1999) based on a 148-magnetometer MEG system and then multiplying **A** by $\vec{s}$. MEG signals were contaminated with Gaussian white noise and the SNR was scaled to different levels (i.e. 20, 15, 10, and 5dB) as

$$SNR = 20\log_{10}\frac{\left\|\mathbf{A}\vec{s}\right\|_2}{\sqrt{M}\,\sigma_{noise}}, \tag{5.3}$$

where M=148 is the number of sensors and σ_{noise} is the standard deviation of the noise.

The sensitivity of VW-SSI to the hyper-parameter λ and the level of wavelet compression in both W-SSI and VW-SSI were investigated. The performance of VW-SSI was compared to other techniques using both ℓ_2-norm regularizations (MNE, wMNE) and cortical LORETA (cLORETA), and ℓ_1-norm regularizations (SSI, V-SSI, and W-SSI). The implementation of ℓ_2-norm regularization approaches adopted a similar constrained optimization problem as in Equation (2.2):

$\min\left\|\mathbf{H}\vec{s}\right\|_2$ subject to $\left\|\vec{\phi}-\mathbf{A}\vec{s}\right\|_2<\beta$, where $\mathbf{H}$ is an identity matrix in MNE (Hämäläinen and Ilmoniemi, 1994), a depth-weighted matrix in wMNE (Dale and Sereno, 1993), and the multiplication of a depth-weighted matrix and a Laplacian matrix in cLORETA (Pascual-Marqui et al., 1994). The selection of the regularization parameter β is the same as in Equation (2.2). The same four metrics used in Section 4.2.1 (AUC, DLE, SD and RMSE) were used to evaluate the performances of all methods from different aspects. The AUC metric, measuring the sensitivity and specificity of detection of simulated cortical sources, evaluates the accuracy of the source locations and extents. DLE and SD were adopted to assess reconstruction accuracies of source locations and extents, separately. RMSE computed total errors from source amplitudes, locations, and extents. Detailed formulae of these four metrics can be found in Appendix B. The values of these metrics were statistically compared among conditions using a non-parametric paired t-test with bootstrap resampling (Efron and Tibshirani, 1993) with the significance level of $p<0.05$.

5.2.2 Influence of the Hyper-parameter λ

Since a hyper-parameter λ is introduced to balance the variation and wavelet terms in VW-SSI, it is worth investigating the influence of the hyper-parameter on performance of VW-SSI. It was found that the ℓ_1-norms of the wavelet coefficients were approximately five times as large as the ℓ_1-norms of the variations from 200 simulated cases. The sensitivity of VW-SSI to λ (using $\mathbf{W}_1$) was tested by selecting the hyper-parameter at 10 different values (Figure 5.1(a)) toward the preference of either the wavelet constraint ($\lambda>0.2$) or the variation constraint ($\lambda<0.2$).

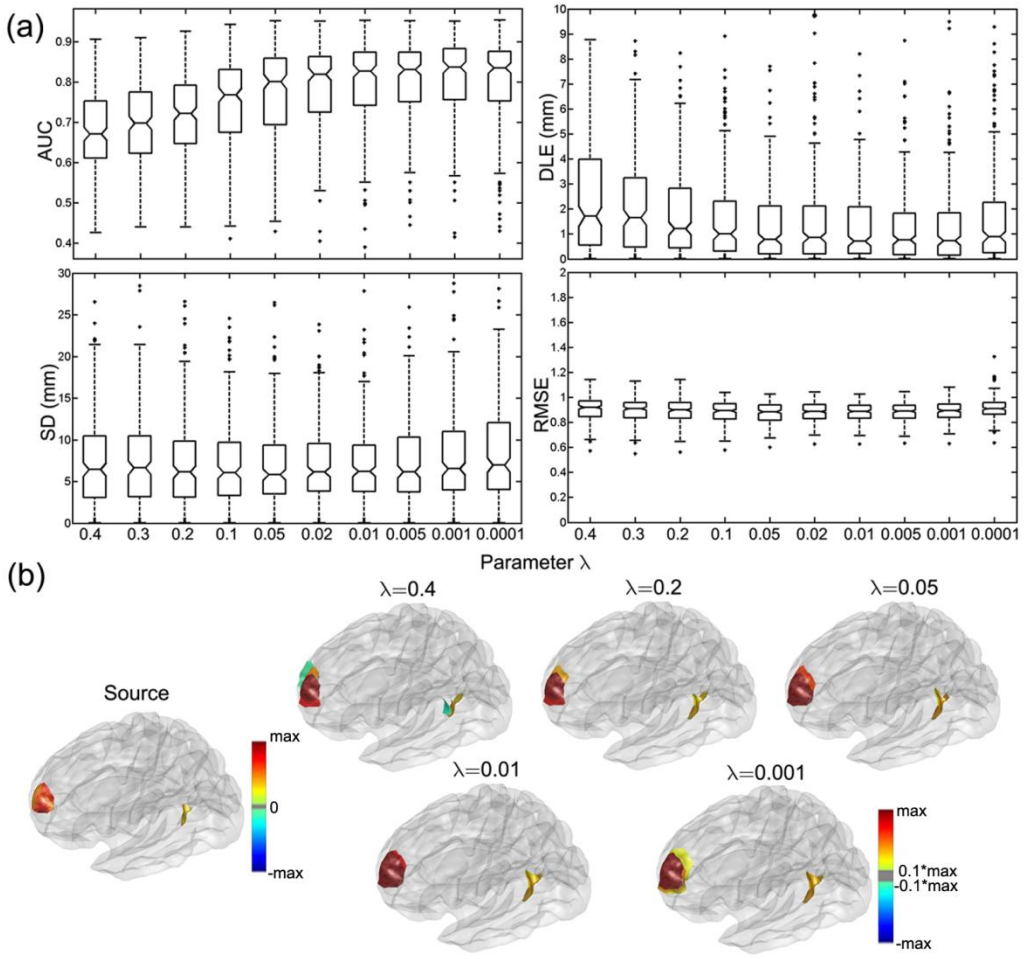

Figure 5.1 Sensitivity of VW-SSI to the hyper-parameter λ.
(a) Notched boxplots of four metrics at different values of λ. The notch indicates the 95% confidence interval on median. (b) An example of simulated source and reconstructions from VW-SSI with different λ. The cortical surfaces were displayed with transparency.

As shown in Figure 5.1(a), the localization accuracy increases (i.e. DLE decreases) for λ values of 0.4 to 0.05, and then shows no significant changes for λ ranging from 0.02 to 0.0001. It was observed that the median estimation accuracy of source extent of VW-SSI, indicated by AUC, increased when placing more weights on the variation constraint (λ from 0.4 to 0.02). The accuracy is also significantly different between λ=0.4 and 0.02 (p<0.001), and shows no significant changes when λ<0.01. When λ continuously decreased from 0.01 to 0.0001, the blurredness starts to degrade

the performance of VW-SSI in estimating source extents, i.e. significantly increased SDs (Bonferroni corrected $p<0.05$). The total estimation errors, indicated by RMSE, suggest no significant changes. In Figure 5.1(b), a selected example indicates that the estimated sources at $\lambda=0.01$ have the most similar location and extent comparing to simulated ones. It was observed that spurious sources show up surrounding the true sources at $\lambda=0.4$ and blurred estimations appear when $\lambda=0.01$ and 0.001, along with the increased SD values in Figure 5.1(a). Taking all metrics into considerations, the hyper-parameter λ was set to 0.01 in the following analyses.

5.2.3 Influence of the Wavelet Compression Level

The influence of the wavelet compression level was investigated in both VW-SSI and W-SSI. It was observed that the performance of W-SSI is more sensitive to the wavelet compression levels than VW-SSI, indicated by significantly increased AUCs (Bonferroni corrected $p<0.001$), and significantly decreased DLEs (Bonferroni corrected $p<0.001$) (Figure 5.2(a)). Through the integration of variation and wavelet constraints, VW-SSI is much less influenced by the wavelet compression level and has much more stable and better performance than W-SSI in all four metrics (i.e. AUC, DLE, SD, and RMSE). The insensitivity of VW-SSI to the wavelet compression level is further visually demonstrated on estimated sources at four levels, which have similar spatial locations and extents (Figure 5.2(b)). These reconstructions are also better than reconstructions from W-SSI, which show over-focused sources with fewer levels of wavelet compressions and blurred sources in more levels of compressions (Figure 5.2(b)), as indicated by the increased SD values (Figure 5.2(a)). Since VW-SSI is insensitive to the compression level, the one-level wavelet compression was adopted in

the following analyses.

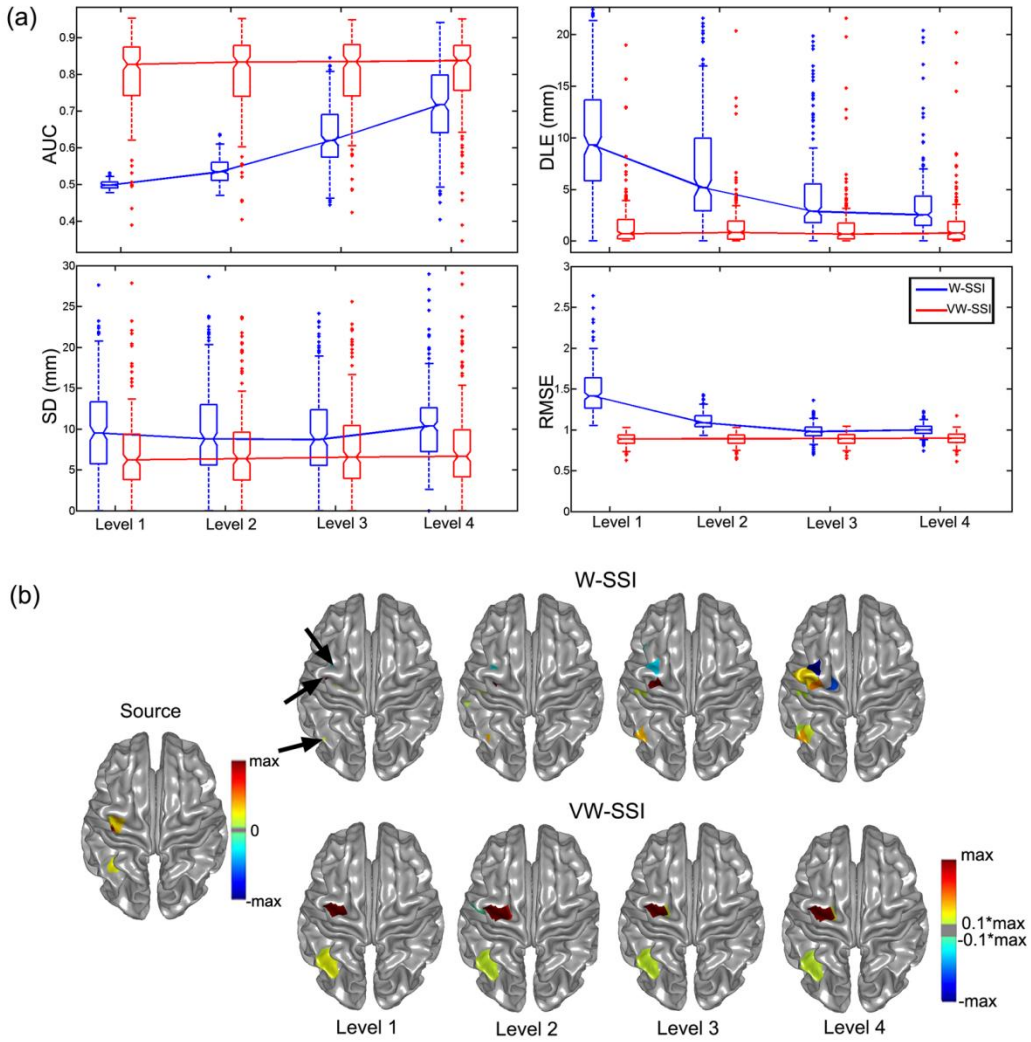

Figure 5.2 Sensitivity of VW-SSI and W-SSI to wavelet compression levels. (a) Notched boxplots of four metrics for W-SSI and VW-SSI with different wavelet compression levels. (b) An example of simulated sources and reconstructions from W-SSI and WV-SSI at the wavelet compression level from one to four.

5.2.4 Comparisons with ℓ_2-norm regularizations

In Figure 5.3(a), compared to classic ℓ_2-norm regularization based approaches (MNE, wMNE, and cLORETA), the proposed VW-SSI method demonstrates significantly better performance than all ℓ_2-norm regularizations (Bonferroni corrected

p<0.01) in all metrics. The relatively high AUC values in MNE and wMNE (medians close to 0.8) are probably because the metric AUC favors blurred source estimations (Liao et al., 2012; Petrov, 2012) and estimated sources from the ℓ_2-norm regularization based approaches are spatially blurred, as suggested by high SD values (Figure 5.3(a)). The median SD values of MNE, wMNE, and cLORETA are about 20mm, 25mm, and 40mm, respectively, while the median SD value of VW-SSI is only about 5mm.

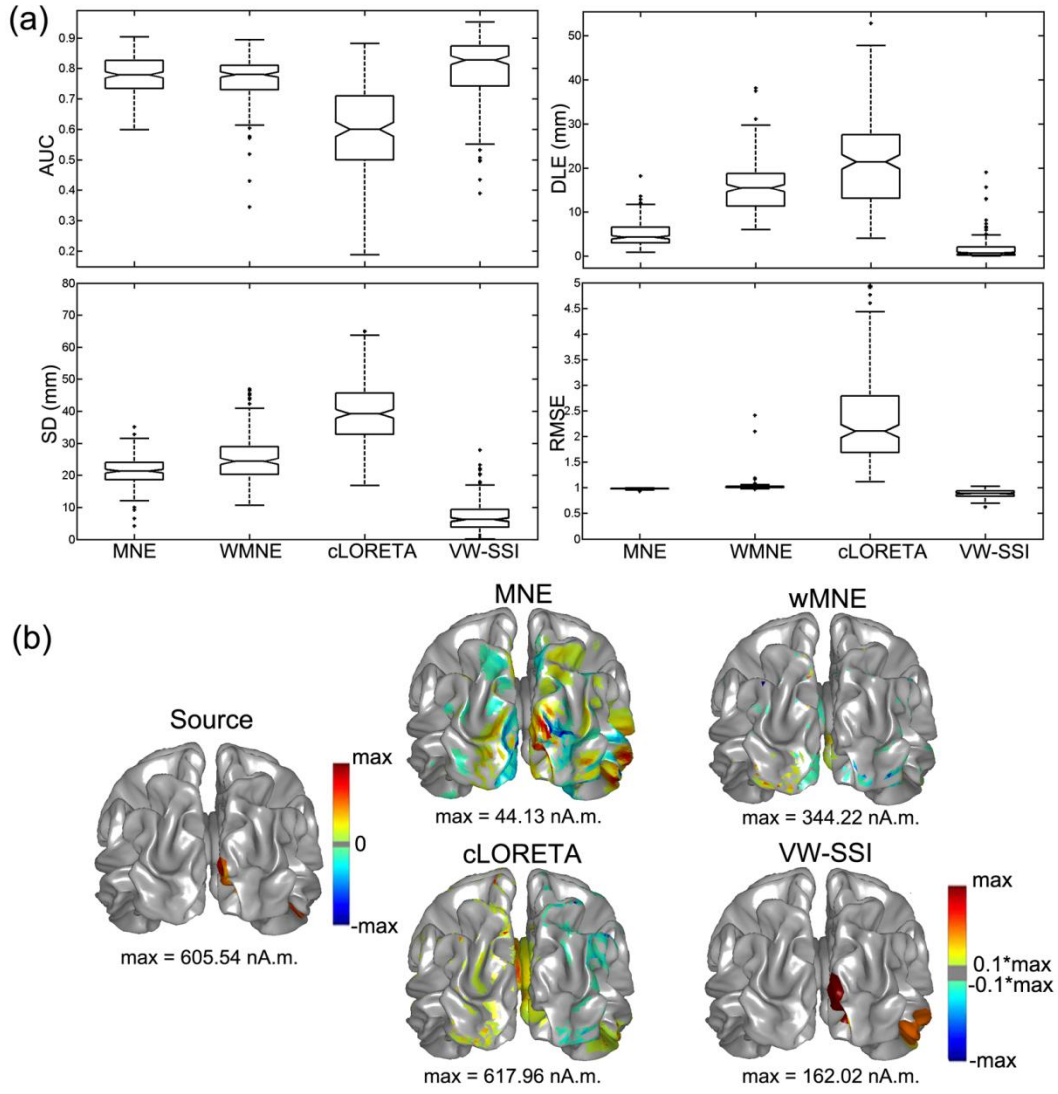

Figure 5.3 Comparison of VW-SSI to ℓ_2-norm regularizations
(a) Notched boxplots of four metrics for MNE, wMNE, cLORETA and VW-SSI. (b) An example of simulated sources and reconstructions from compared methods.

VW-SSI also reveals much less biases in source locations (the median value of DLE is 1mm) than the ℓ_2-norm regularization approaches (5mm in MNE, 15mm in wMNE, and 20mm in cLORETA). While RMSE from VW-SSI is significantly lower than all ℓ_2-norm regularizations (Bonferroni corrected p<0.001), the source strengths are still underestimated (maximal values: 162 nA.m in estimated sources and 606 nA.m in simulated sources). The selected example (Figure 5.3(b)) also shows better performance of VW-SSI compared to MNE, wMNE, and cLORETA. The sources estimated from MNE, wMNE and cLORETA are observed with problems of diffused distributions (in MNE), spurious sources surrounding true sources (in MNE and cLORETA) and even at areas far from the true sources (in cLORETA) and missed sources (in wMNE and cLORETA).

5.2.5 Comparisons to Other ℓ_1-norm regularizations

In Figure 5.4, the performance of VW-SSI is also compared to other ℓ_1-norm methods, i.e. SSI, V-SSI and W-SSI with a level-four compression (denoted as W_4-SSI). VW-SSI shows significantly better performance than SSI and W_4-SSI (Bonferroni corrected p<0.001) in all metrics. It also has significantly lower SD (p<0.001), DLE (p<0.01), and RMSE values (p<0.01) than V-SSI. It is noted that SSI, as compared with the other three ℓ_1-norm methods, has significantly lower AUC values, higher DLE and RMSE values (Bonferroni corrected p<0.001). The selected example (Figure 5.4(b)) also demonstrates the better performance of VW-SSI in estimating both source locations and extents compared to the other three methods. The sources estimated from SSI are only active on a few elements (about 7mm^2), which are over-focused as compared with the simulated ones (about 743mm^2). Spurious sources are observed in

W_4-SSI surrounding the true sources and, in V-SSI, spatially more extended sources are observed, which are all suppressed in VW-SSI.

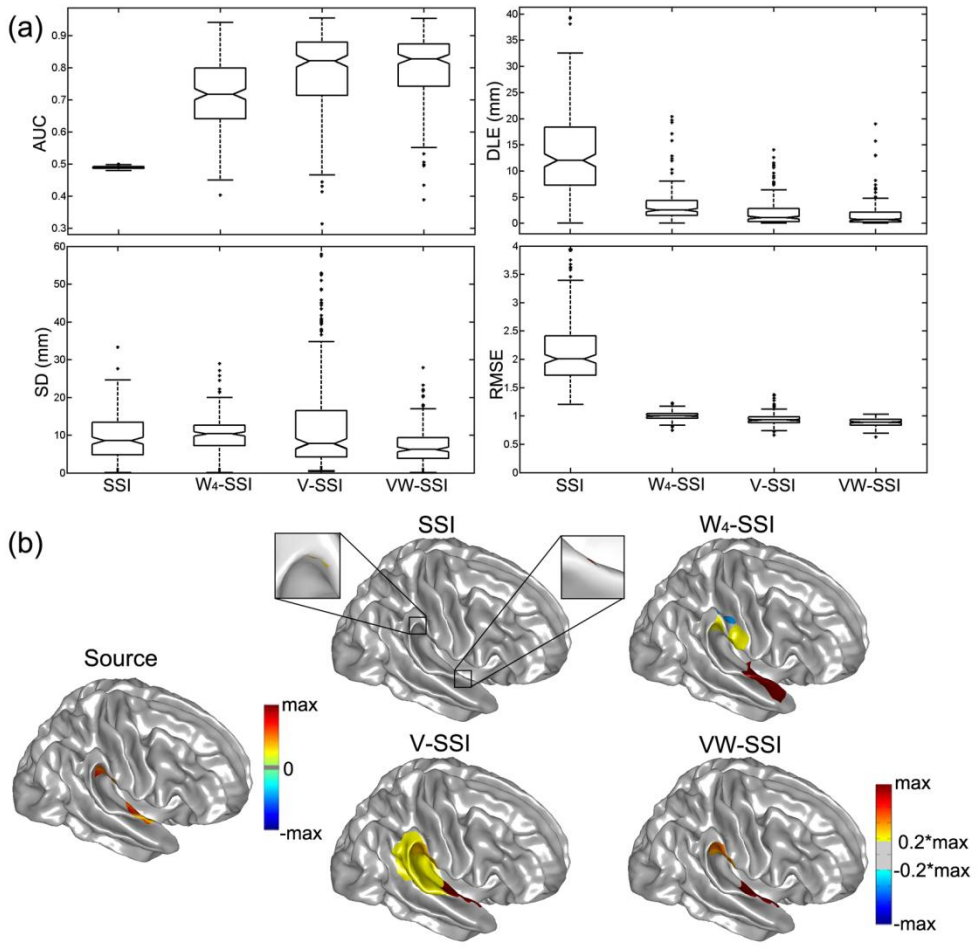

Figure 5.4 Comparison of VW-SSI to other ℓ_1-norm regularizations
(a) Notched boxplots of four metrics for SSI, W4-SSI, V-SSI and VW-SSI. (b) An example of simulated sources and reconstructions from compared methods.

5.2.6 Effects of Source Extent

The performance of VW-SSI was further investigated with varied source extents (two patch sources) and compared with MNE and V-SSI (Figure 5.5(a)). All three methods indicate decreasing trends in AUC medians when the size of the source increases. In contrast, medians of DLE, SD, and RMSE become slightly better in VW-

SSI. It is observed that VW-SSI has significantly better performance (Bonferroni corrected $p<0.05$) than MNE in all four metrics and all source extents. VW-SSI also shows significantly better performance (Bonferroni corrected $p<0.05$) than V-SSI in DLE, SD, and RMSE with all source extents. Each circle in Figure 5.5(b) indicates the relation between true source extent and estimated source extent (thresholded at 20% of individual maxima to reject more background activity in MNE) from each simulation. Linear regression results (Figure 5.5(b)) indicate that VW-SSI provides better preservation of extent contrast in simulated sources with the slope of 0.72 (close to 1) as

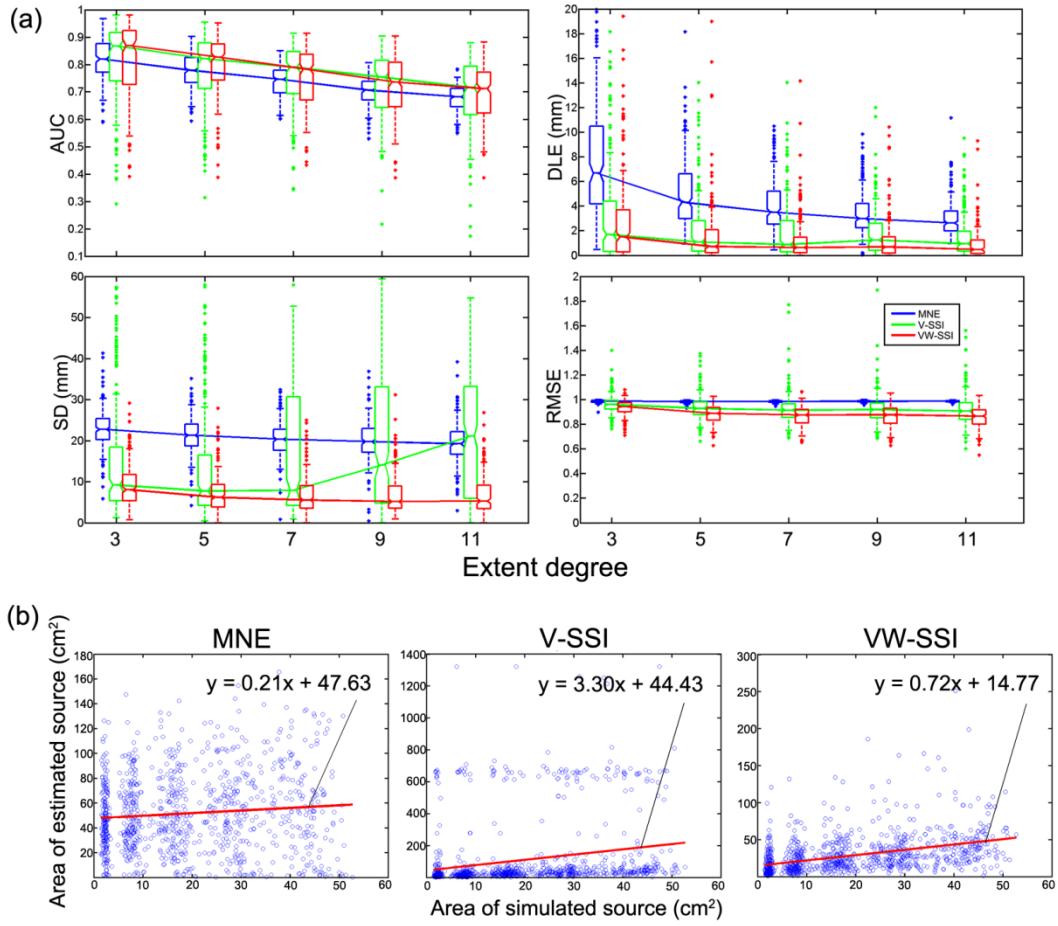

Figure 5.5 Performances with various source extents

(a) Notched boxplots of four metrics for MNE, V-SSI and VW-SSI at different source extents. (b) Linear regressions (red lines) on extent data of simulated sources (x-axis) and extent data of estimated sources (y-axis) from MNE, V-SSI, and VW-SSI. Each circle indicates the result from one of 1000 simulations for five different source extents.

compared to MNE (slope: 0.21), which underestimates extent contrast, and V-SSI (slope: 3.30), which overestimate extent contrast. It is noted that V-SSI has a better extent contrast pattern when estimating sources with extent below 200cm^2. However, its solutions sometime suffer from the unconstrained global power problem, which leads to unreasonable source extent estimations (beyond 600cm^2). Furthermore, the relatively large intercept (~14cm^2) in VW-SSI suggests the existence of a systematic bias, while it is only about one-third of those obtained with MNE and V-SSI.

5.2.7 Effects of Number of Sources

Figure 5.6(a) shows that VW-SSI indicates a decrease in AUC medians and slightly increases medians in the other three metrics when the number of sources increases (extent degree 5). VW-SSI demonstrated significantly better performance than MNE with all numbers of sources (Bonferroni corrected $p<0.01$) in all four metrics, except for AUC with 5 sources. As compared to V-SSI, VW-SSI has better performance with multiple sources, indicated by significantly higher AUCs ($p<0.01$) in simulations with 3 and 5 sources and significantly lower DLEs ($p<0.01$) in simulations with 2, 3, and 5 sources. VW-SSI also showed better performance than V-SSI with significantly lower SDs and RMSEs with all numbers of sources (Bonferroni corrected $p<0.05$). The examples in Figure 5.6(b) suggest that both VW-SSI and V-SSI recover more accurate source locations and extents in the cases with 1, 2, and 3 source(s) than MNE. In the case with 5 sources, V-SSI exhibited worse performance than VW-SSI since spurious sources are observed in V-SSI.

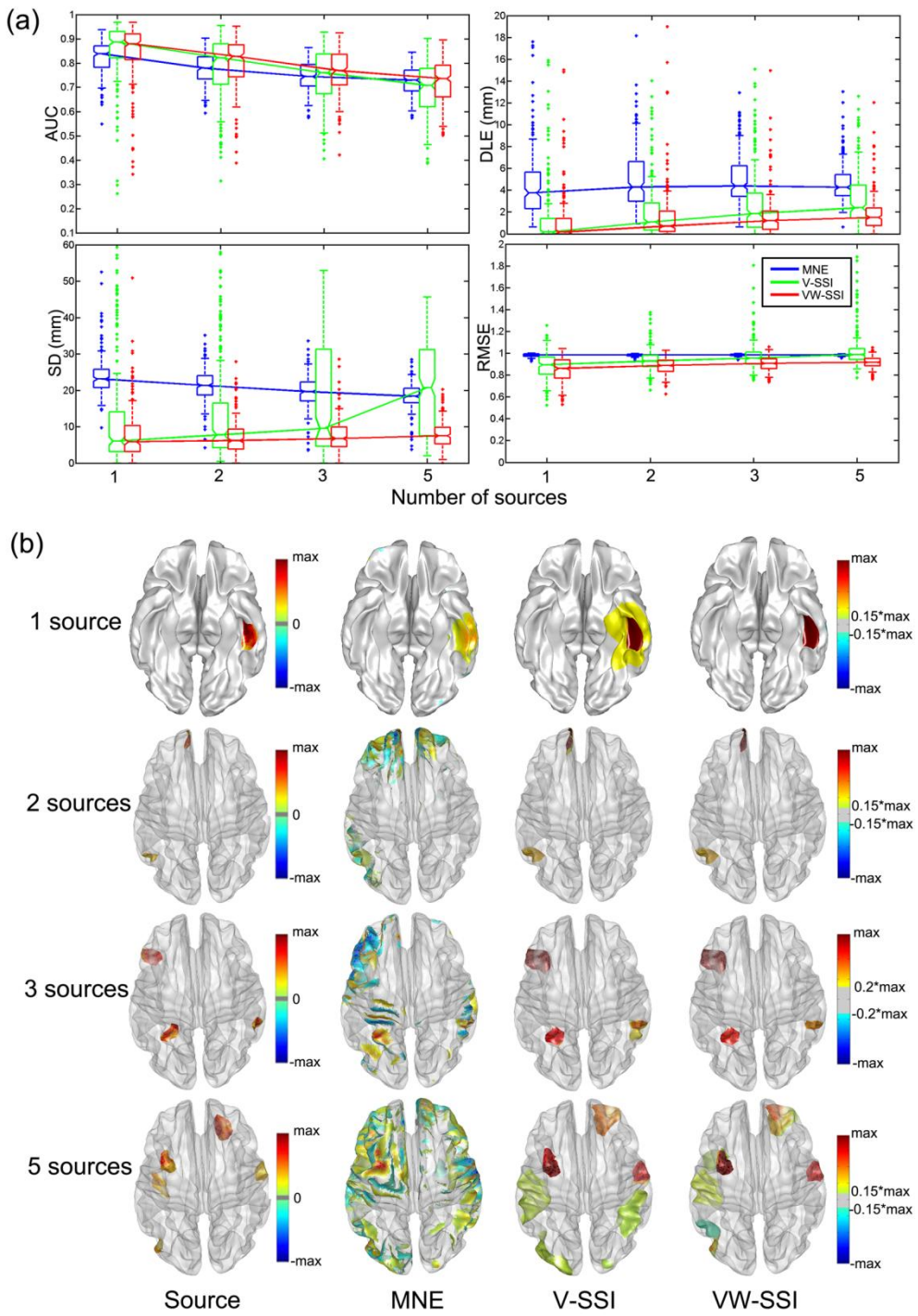

Figure 5.6 Performance with different numbers of sources

(a) Notched boxplots of four metrics for MNE, V-SSI and VW-SSI at different numbers of sources. (b) Examples of simulated sources and reconstructions from compared methods. The cortical surfaces were displayed with transparency when necessary to visualize all sources at the same visual angle.

5.2.8 Sensitivity to SNR

In Figure 5.7, all four metrics at different SNR levels indicate that the performance of W_4-SSI, V-SSI and VW-SSI depends on SNR. Among them, V-SSI gives the highest sensitivity to SNR with a dramatic increase of SD values at both 10dB and 5dB, and decreases in both AUC and DLE as well, which is because the global energy is not limited in V-SSI (Ding, 2009) and becomes severe when SNR is low. While both W_4-SSI and VW-SSI reveal similar degrading patterns in performance as SNR decreases, VW-SSI always delivers significantly better performances (Bonferroni corrected $p<0.01$) than W_4-SSI in all metrics at all SNR levels. In the examples in Figure 5.8(b), spurious sources (black circles) observed in W_4-SSI and blurred distributions observed in V-SSI at low SNRs (e.g. 5dB) are sufficiently suppressed by VW-SSI.

5.3 Performance Analysis Using Experimental Data

5.3.1 Experiment Protocol

Experimental MEG data for a language task and a motor task were collected from one patient with medically refractory epilepsy, who underwent pre-surgical evaluation at Minnesota Epilepsy Group, St. Paul, MN. The study protocol was approved by the Institutional Review Boards of University of Oklahoma Health Science Center, OK and United Hospital, St. Paul, MN. The language task used the same protocol as in Section 4.3.1. The motor task was designed as a self-paced finger tapping task to push a button with the index finger every one to two second(s). The MEG data were acquired using a whole head 148-channel magnetometer array (the same system as in Section 3.2.1) at a sampling rate of 254.31Hz in the language task and 290.64Hz in

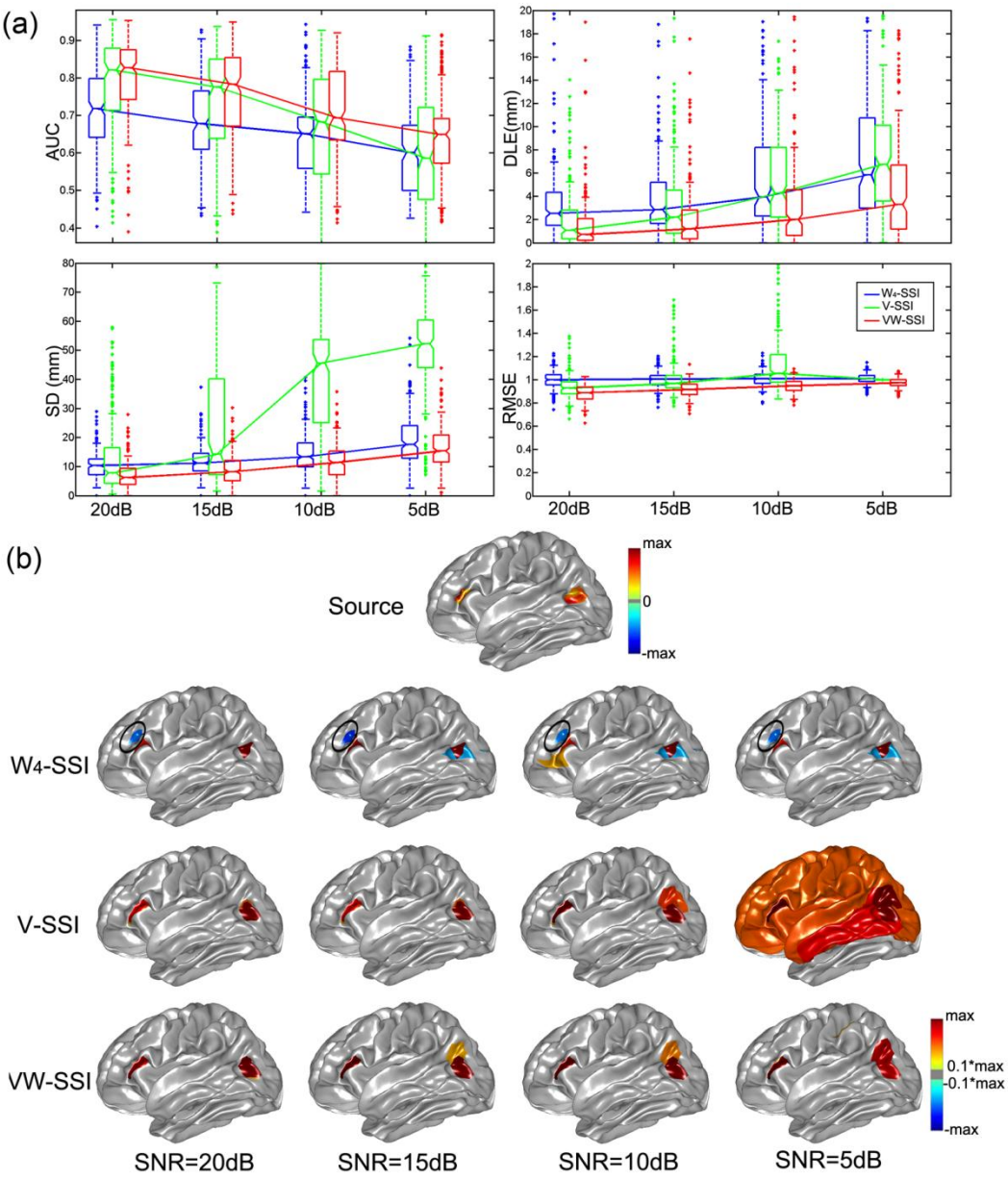

Figure 5.7 Performances at different SNR levels

(a) Notched boxplots of four metrics for W_4-SSI, V-SSI and VW-SSI at different SNR levels. (b) An example of simulated sources and estimated sources from compared methods at different SNR levels.

the motor task. MEG epochs were extracted with a window of -150ms to 1000ms with respect to the onset of word stimuli in the language task and a window of -45ms to 300ms with respect to the onset of movement cues. Band-pass filters of 0.1 to 20Hz in the language task and 2 to 20Hz in the motor task were applied. The pre-stimulus data are used as intervals to perform baseline correction in both data sets. Independent component analysis (ICA) was performed to reject artifacts related to eye blinks, muscle movements, and heartbeats. Event-related fields (ERFs) are obtained by averaging remaining 120 epochs for the language task and 191 epochs for the motor task after artifact removal. Individual BE head models and CCD models were built from the patient's T1-weigthed MRI data using the same protocol as in simulation. Co-registration between the CCD models, BE models, and MEG sensors was conducted by aligning fiducial points (left and right pre-auricular points and nasion) and further refined by fitting digitized head points to the BE models.

5.3.2 The Language Task

In the language task, the estimated sources from VW-SSI (Figure 5.8) locate on the right superior temporal cortex within the coverage of Brodmann areas (BAs) 41 and 42 at a latency of 94ms, which suggests the early sensory response in the primary auditory cortices around 100ms (Zouridakis et al., 1998). At a latency of 232ms, the estimated sources from VW-SSI appeared on the bilaterally medial temporal cortices, suggesting the late language process occurred between 200ms and 300ms post-stimulus, associated with the decoding of phonological and semantic components of words (Breier et al., 1998; Frye et al., 2009). The sources estimated with MNE and wMNE were scattered on multiple brain areas including the right temporal, right anterior

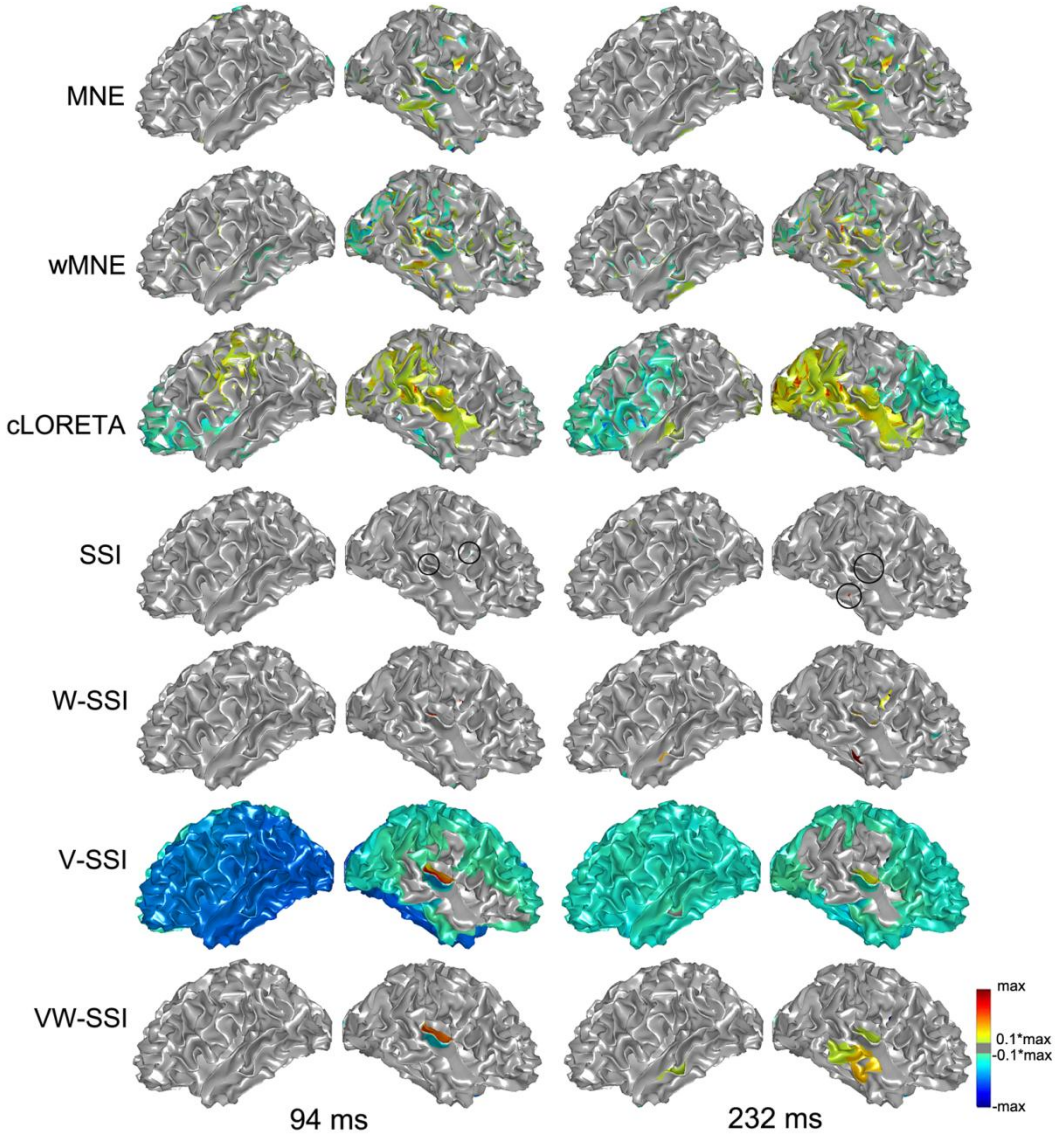

Figure 5.8 Estimated sources in a language task
Estimated sources of early auditory response and late language processing from MNE, wMNE, cLORETA, SSI, V-SSI, W-SSI and VW-SSI at 94 ms and 232 ms, respectively, after the onset of stimulus.

parietal, and left temporal cortices similarly at both latencies. cLORETA produces more smoothed sources covering similar brain areas than MNE and wMNE. More importantly, their estimated sources at different timings (i.e. 94ms and 232ms) did not reveal observable distinctions among the early sensory response and the late language processing. The estimated sources from V-SSI indicated similar reconstructions on BAs

41, 42 at 94ms, while the estimations are suffered from unconstrained global powers and become worse at 232ms. SSI and W-SSI produced more compact estimations on the temporal cortices at both times. However, both SSI and W-SSI indicated spurious extra-temporal activations and their temporal sources at 232ms more toward the inferior part of the temporal lobe.

5.3.2 The Motor Task

In the finger tapping task, the estimated sources from VW-SSI (Figure 5.9) indicate outward currents on the anterior bank of the central sulcus (the primary motor cortex, M1) at 45ms and outward currents on the posterior bank of the central sulcus (the primary somatosensory cortex, S1) at 151ms, which is well consistent with the generators of motor field (0~100ms) from M1 and post-movement motor field (>120ms) from S1 (Gerloff et al., 1998; Pollok et al., 2003). The sources estimated from MNE, wMNE, cLORETA and V-SSI are diffused (V-SSI also suffers from unconstrained global powers) and not able to distinguish activations from M1 and S1. The sources estimated from SSI and W-SSI is confined on S1 at both 45ms and 151ms with currents changing from inward to outward.

5.4 Discussion and Summary

In this chapter, the sparse source imaging technique was extended to enforce sparseness in multiple transform domains simultaneously for the first time. The proposed ℓ_1-norm regularization implemented with variation and face-based wavelet transforms showed better accuracy in estimating source locations and extents than the commonly used ℓ_2-norm regularization approaches (i.e. MNE, wMNE and cLORETA) and other ℓ_1-norm regularizations with a single transform (i.e. SSI, V-SSI and W-SSI).

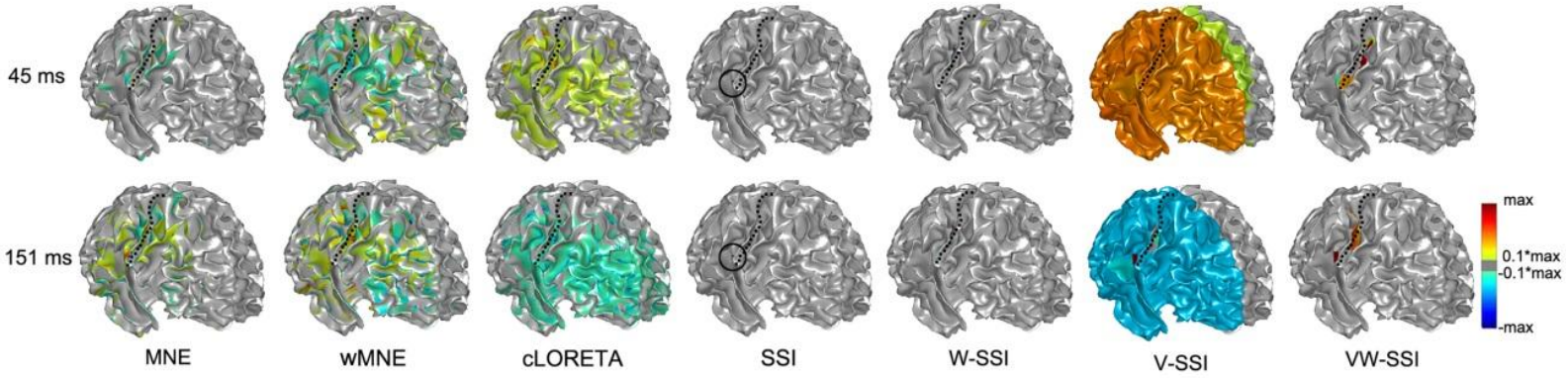

Figure 5.9 Estimated sources in a motor task

Estimated sources of the motor task from MNE, wMNE, cLORETA, SSI, V-SSI, W-SSI and VW-SSI at 45 ms and 151 ms after the onset of stimulus. Black dashed line: central sulcus.

The ℓ_2-norm regularization approaches based on distributed source models (Dale and Sereno, 1993; Hämäläinen and Ilmoniemi, 1994; Pascual-Marqui et al., 1994) have been widely used to recover distributed brain sources. Their inverse solutions are spatially diffused, as suggested by the quantitative measures obtained in simulations (AUC and SD data in Figure 5.3) and in agreement with the prior research (Grova et al., 2006; Vega-Hernández et al., 2008). Due to the blurredness, their estimated sources were easily mislocalized (see the DLE measure in Figures 5.3(a), 5.5(a), 5.7(a)). Due to the lack of consideration of spatial continuity (in MNE and wMNE), ℓ_2-norm inverse solutions suffer from the spatial discontinuity problem in source distributions (Figures 5.3(b), 5.6(b)), making it difficult to separate multiple sources and estimate their extents (Figure 5.6(b)). On the other hand, the ℓ_1-norm inverse solutions (i.e. SSI) obtained by enforcing sparseness in the original source domain (Tibshirani, 1996; Uutela et al., 1999), suffered from the over-focality problem (Chang et al., 2010). V-SSI and W-SSI, enforcing sparseness in transform domains, showed better performance in recovering source extents, as suggested by the data obtained here (AUC and SD data in Figure 5.4(a)) and the literature (Ding, 2009; Chang et al., 2010; Liao et al., 2012). However, the performance of W-SSI was highly dependent on the compression scheme (e.g. spherical wavelets vs. face-based wavelets) (Liao et al., 2012) and the compression level, as suggested in Figure 5.2 and supported in the literature (Chang et al., 2010). Due to the unconstrained global power, inverse solutions in V-SSI can potentially have uncontrolled global activity (Figures, 5.7(b), 5.8(b), 5.9(b)). The VW-SSI method takes the advantages of both V-SSI (its capability in recovering source boundaries and thus source extents) and W-SSI (its capability in compressing sources for better sparse

reconstructions), which results in significant improvements in estimating source locations (e.g. better DLE) and extents (i.e. better AUC and SD) than the ℓ_2-norm and other ℓ_1-norm regularization methods. It is also noted that VW-SSI has significantly better performance in preserving extent contrast among sources of different sizes than other ℓ_2-norm and ℓ_1-norm methods (Figure 5.5(b)). However, a systematic bias (the intercept from the linear regression in Figure 5.5(b)) in estimating source extents still exists in VW-SSI, which indicates the overestimation of source extents, as reflected by underestimated source strengths (Figure 5.3(b)). Such a constant bias can be further reduced if multimodal data (i.e. EEG and MEG) are integrated (Ding and Yuan, 2013a).

The combination of variation and wavelet penalties in VW-SSI was also demonstrated, providing the robust performance on influential factors, such as wavelet compression level and noise. While the performance of W-SSI largely depends on the compression level, the performance of VW-SSI is not significantly influenced by this factor, which is achieved with the use of the variation penalty (Figure 5.2). The simulation results with varied SNRs further indicate that VW-SSI is less sensitive to noise than V-SSI (Figure 5.7).

In a language task, VW-SSI successfully recovered the dynamic neural activations (Figure 5.8) from early auditory response (Zouridakis et al., 1998) to late language processing (Breier et al., 1998; Frye et al., 2009). From the spatial locations and extents of these sources, neural activations due to auditory responses (over superior temporal cortex) and language processes (over medial temporal cortex) were well distinguished in VW-SSI inverse solutions. All of the other methods were unable to recover these neural activation patterns, except W-SSI, which recovered several patterns

as seen in VW-SSI with degradations. Due to the ill-posed nature of EEG/MEG inverse problems, it has been deemed challenging to recover cortical sources across a sulcus (Ou et al., 2009) since sources on the pre-bank and post-bank of a sulcus can generate similar surface EEG/MEG signals by just flipping source orientations. In Figure 5.9, VW-SSI demonstrates the capability in distinguishing neural activations from the pre-bank and post-bank of the central sulcus in a motor task, which has been well studied using fMRI (Jäncke et al., 2000). Meanwhile, all other methods investigated failed to recover such nearby sources. The capability of VW-SSI in detecting multiple functional brain activation sites from either remote area (e.g. symmetrical areas on two hemispheres) or adjacent areas (e.g. pre- and post-bank of the central sulcus) is valuable in understanding brain functions and also in identifying eloquent cortices to perform brain surgery for epilepsy patients.

It is important to note that one limitation of using multiple penalties in a regularization problem is how to decide the value of the hyper-parameter. While some strategies have been developed for ℓ_2-norm regularizations (Vega-Hernández et al., 2008), there are few studies addressing such an issue in ℓ_1-norm regularizations. The simulation results obtained here suggest that the proposed method is quite robust to the hyper-parameter in a wide range of values. The experimental results also indicate stable performance of VW-SSI with the hyper-parameter value selected based on simulation results. Nevertheless, more studies, especially those about criteria on automatically selecting the parameter, will be needed, particularly when there are other complicating factors, such as wavelet compression level.

In summary, I developed a new sparse source imaging method that combines the use of multiple transforms in ℓ_1-norm regularization to better estimate cortical source locations and extents. Compared to ℓ_2-norm regularizations, the proposed method, VW-SSI, demonstrates significantly improved capability in reconstructing multiple extended cortical sources with less spatial blurredness and less localization error. With the use of transform sparseness, VW-SSI overcomes the over-focused problem in classic SSI methods. With the use of two transformations, VW-SSI further provides improved performance in estimating MEG source locations and extents than other SSI methods with a single transformation. The experimental results indicate that VW-SSI can successfully estimate neural sources (and their spatial coverage) located in nearby areas that are responsible for different functions (e.g. temporal cortical sources for auditory and language processing, and sources on the pre-bank and post-bank of the central sulcus). Precise estimation of cortical source locations and extents from EEG/MEG is clinically significant for identifying the location and extent of epileptic brain tissues and eloquent cortices to perform surgery treatment for partial epilepsy patients.

Chapter 6: Discussion and Conclusion

This chapter discusses and summarizes the work presented in this dissertation from several angles. The utilization of transform sparseness in ℓ_1-norm regularization is discussed from the aspect of compressive sensing (CS) theory and the benefits of pursuing transform sparseness are supported by evidence from source reconstruction results using variation based sparse source imaging (V-SSI) and wavelet based sparse source imaging (W-SSI) techniques. The feasibility of using multiple penalties in ℓ_1-norm regularization is also discussed by comparing it to ℓ_1-norm regularization with a single penalty term. These discussions are followed by descriptions of current limitations of the work presented in this dissertation and possible future work. The chapter ends with general conclusions for the whole dissertation.

6.1 Transform Sparseness

CS theory suggests that the sparser a signal is, the more accurately the reconstruction can be achieved via ℓ_1-norm regularization (Candès et al., 2006; Candès and Romberg, 2007). However, synchronous cortical activation with an area of at least $6cm^2$ is required for detectable potentials on the scalp (Cooper et al., 1965), which implies that the cortical current sources might not be sparse enough to satisfy the CS theory in the original signal domain. This has also been proven from the over-focused reconstructions by ℓ_1-norm regularization via enforcing sparseness in the original source domain (Figures 3.1, 5.4, 5.8, 5.9). For example, reconstructed sources by the classic sparse source imaging (SSI) technique in Figure 3.1 indicate brain activation with an area of around $0.1cm^2$, which is much less than the required $6cm^2$ for generating scalp

detectable signals. The usage of sparse representations of cortical current densities is thus expected to improve the performance of ℓ_1-norm regularization.

In Chapter 3, variations between neighboring currents were adopted as a sparse representation of the cortical current density. Previous ECoG or fMRI studies have already shown that functional brain activation and epileptic sources for partial epilepsy patients are usually confined within certain areas (Jäncke et al., 2000; Tao et al., 2005). By computing variations on those confined brain activations, large variations are likely to occur on the boundaries between active and inactive areas. By enforcing sparseness of the variations, ℓ_1-norm regularization is expected to reconstruct non-zero values only on the boundaries. Although small variations inside brain activation are ignored, the proposed approach attempts to preserve the active/inactive boundaries to better estimate the source extent, which is of significant clinical importance to tailor resection areas in the surgical planning for partial epilepsy patients.

In Chapter 4, face-based wavelets were designed to sparsely represent the cortical current density. Simulation results in Figure 4.2(a) show that the face-based wavelets (compression levels 3 and 4) have excellent compression capability to represent the cortical current density with a small number of coefficients (compression ratio=10%) without significant reductions in synthetic accuracies (AUC of around 0.95 and RMSE of around 0.3). It was also demonstrated that the compression capability of the face-based wavelets is not sensitive to the number of sources (varied from 1 to 10) (Figure 4.2(a)). Reconstructed results on simulated MEG further indicated better performance of the proposed wavelet-based sparse source imaging using the face-based wavelet in detecting locations and extents for multiple sources as compared to the

wavelet-based sparse source imaging using the vertex-based wavelet method (Figure 4.3).

It was demonstrated that the implementation of sparse representations of the cortical current density, variations or face-based wavelet coefficient, in the ℓ_1-norm regularization successfully avoids the over-focality of classic SSI. With the property of preserving source boundaries, V-SSI is able to reconstruct cortical sources from focal to extended (Figure 5.5). However, reconstructed sources by V-SSI tend to be spatially blurred when the activation area extends to larger than 20cm^2 or more than three brain activations are present (Figure 5.6(a)), which introduces bias in estimating source extent as well as distinguishing different sources. Since synthetic performance of the face-based wavelets indicate the cortical current density is sparser at higher compression levels, the performance of W-SSI at compression level 4 has significant better performance than at other lower levels (Figure 5.2). W-SSI provides an advantage of detecting multiple simultaneous activations (Figures 4.4, 5.8), which makes it attractive in studying the higher cognitive brain function that usually involves more than one brain activations (Breier et al., 1998; Frye et al., 2009), as well as in estimating epileptogenic zones for epilepsy patients with multiple lesions (Patient 2 in Chapter 3).

6.2 Single Penalty vs. Multiple Penalties

Although the ℓ_1-norm regularization implemented with a single transform (V-SSI or W-SSI) yielded better performance than the classic SSI, they have their own advantages and disadvantages in estimating source locations and extents. One contribution of the present dissertation is to propose a multi-penalty scheme to integrate more than one transform into the ℓ_1-norm regularization. Multiple penalties have been

used in regularization for years to select preferred solutions for achieving either smoothness or sparseness (Tibshirani et al., 2005; Zou and Hastie, 2005; Vega-Hernández et al., 2008; Hebiri and van de Geer, 2011; Haufe et al., 2008; Chang et al., 2010). Ridge fused (Vega-Hernández et al., 2008) combines two ℓ_2-norm penalties used in MNE and LORETA to achieve controlled blurredness in inverse solutions. Methods such as Elastic Net (Zou and Hastie, 2005), Elastic Net-L (Vega-Hernández et al., 2008), and smooth LASSO (Hebiri and van de Geer, 2011), have been developed to compensate the smoothness from the ℓ_2-norm penalty using the ℓ_1-norm penalty. Other methods, such as LASSO Fused (Tibshirani et al., 2005), Focal vector field reconstruction (Haufe et al., 2008), and compressive neuromagnetic tomography (Chang et al., 2010) apply sparseness in the original source domain as SSI and, at the same time, constrain local smoothness using either successive differences or spatial transforms. In this dissertation, sparseness was enforced simultaneously in two transform domains (i.e. variation and wavelet domains) for the first time.

The proposed method demonstrated better accuracy in recovering the source location and extent, as well as improved performance compared with other regularizations using single penalties (Figure 5.4). By introducing the variation penalty, the dependence of the face-based wavelets on the compression level was significantly reduced in VW-SSI (Figure 5.2). By introducing the wavelet penalty to constrain the global energy, the spatial blurredness previously observed in V-SSI with extensive sources (Figure 5.5(a)) and multiple sources (Figure 5.6(a)) was also reduced in VW-SSI. The benefit of combining variation and wavelet penalties was also demonstrated by robust performance in terms of influential factors, such as the extent of sources (Figure

5.5), the number of sources (Figure 5.6) and measurement noise (Figure 5.7). The improved performance in reconstruction accuracies by combining more than one transform into the sparse source imaging framework (i.e. ℓ_1-norm regularization) will ultimately hold benefit for the estimation of cortical sources, especially the source extent, as well as for identifying functional brain areas and regions of epileptic brain tissues for surgery.

6.3 Recovering Sources with Extent Information

With the ultimate goal of using EEG/MEG inverse solutions to recover cortical sources with exact locations, extents, and amplitudes, most available methods focus on locations, such as localization of dipole sources (Wood, 1982; Stefan et al., 2003) and extended sources (Chowdhury et al., 2013). It has been demonstrated that brain sources from the same cortical area with different extents generate different patterns in surface electromagnetic signals (Ding and Yuan, 2013a). The goal of the methods proposed in this dissertation is to achieve better estimation of source extents, beyond source localization, which is of significance for applications in clinical practice (Engel, 1993; Wiebe, et al., 2001; Spencer and Huh, 2008) and neuroscience research (Hillyard, 1993; Dhond et al., 2001). For example, the identification of eloquent brain areas of functional importance and/or epileptogenic zones and the decision on whether they are overlapping are essential for the pre-surgical planning of brain surgery in epilepsy (Plummer et al., 2008; Brodbeck et al., 2011), which all need critical extent information besides locations.

Although the conventional ℓ_2-norm regularization method (MNE) provides a relatively high detection accuracy (AUC of around 0.8) in simulations (Figures 5.3,

5.5), its problems of spatial blurredness (indicated by high SD) and mislocalization (indicated by high DLE) imply that it might not be a suitable tool to estimate the location and extent of epileptic sources for surgical planning. The over-focality in classic SSI solutions has already been demonstrated in Figures 3.1, 5.4, 5.8, and 5.9. This is the main reason that classic SSI is not suitable for estimating epileptic sources underlying interictal spikes, which are known to be extended (Tao et al., 2005). With the application of sparse transforms, SSI, V-SSI, W-SSI and VW-SSI are all able to recover extended brain activations and infer their extents. However, both simulation and experimental results indicate V-SSI sometimes suffers from unconstrained global energy, resulting in unrealistic brain activations with extensive coverage of almost one hemisphere (Figures 5.5, 5.7-5.9), especially when the SNR is low (Figure 5.7). Those unrealistic reconstructions have not been observed in VW-SSI because of the introduction of an extra wavelet penalty as the global energy control (Figure 5.5, 5.7-5.9). The source extent estimated by W-SSI highly depends on the selection of compression levels (Figures 4.3, 5.2). For cortical sources with extent larger than $6cm^2$, W-SSI with compression level 4 yields a better performance than at the other lower levels (Figure 5.2), but still not as good as the combination method, i.e. VW-SSI. In short, the proposed SSI methods, i.e. V-SSI, W-SSI and VW-SSI, are promising tools for recovering extended brain activations with not only location information but also extent information, and among them VW-SSI has the best ability in estimating the source extent.

6.4 Applications in Epilepsy

Although the proposed sparse source imaging techniques (V-SSI, W-SSI and

VW-SSI) have good recovering abilities for spatially extended sources in simulations, their feasibility in real applications, such as the identification of epileptogenic zones for partial epilepsy patients or estimation of significant brain areas corresponding to brain functions (e.g. auditory, language or motor), still need to be evaluated.

In this dissertation, V-SSI was applied to 108 interictal MEG spikes from three medically refractory epilepsy patients. Quantitative comparisons between irritative zones (IZs) estimated by V-SSI and clinical validations (e.g. clinical diagnosis, MRI lesions, and resection area if applicable) showed high spatial consistency: 21 out of 24 IISs for Patient 1, 53 out of 55 IISs for patient 2, and 28 out of 29 IISs for Patient 3 (Table 3.2). Qualitative observation of reconstructed sources using W-SSI also demonstrated locations consistent with clinical diagnosis, MRI lesions, or surgical resections for the three patients. For Patients 1 and 3, both V-SSI and W-SSI were applied to estimate epileptic sources from multiple IISs. In Patient 1, locations of epileptic sources identified by V-SSI and W-SSI were similar, but sources estimated from W-SSI were less extended than those obtained with V-SSI. For Patient 3, who is diagnosed with Landau-Kleffner syndrome (LKS), perisylvian activations were observed with both methods (Figures 3.4, 4.7). The results are consistent with findings in other references (Paetau et al., 1999; Rotenberg and Pearl, 2003). Only V-SSI was applied to the data from Patient 2, due to the bad segmentation of cortical surface that is not sufficient for the application of face-based wavelets. Multiple epileptic sources identified on the right hemisphere were all consistent with the MRI lesions and resection areas, while one epileptic source on the left was a little forward as compared to the MRI lesions (Figure 3.3). It is suggested that V-SSI was able to detect multiple

epileptic sources, but the estimation for bilateral sources might not be accurate. W-SSI was applied to another epilepsy patient (Patient 4) to estimate epileptic sources underlying IISs. Estimated epileptic sources by W-SSI were consistent with the resections in terms of location, but less extensive (Figure 4.6). All four epilepsy patients are candidates for surgical treatment at the Minnesota Epilepsy Group, St. Paul, MN. The spatial consistency between the estimated epileptic sources by using SSI techniques and clinical validations suggest a promising application of SSI methods to assist in pre-surgical planning for partial epilepsy patients. Of course, more patients and more possible validations, such as fMRI or ECoG, are needed for further evaluations in the future.

The VW-SSI method was applied to experimental MEG recordings in a language and a motor task from an epilepsy patient in order to identify eloquent cortices related to important brain functions. In the auditory recognition language task, VW-SSI successfully detected the neural activations on the superior temporal cortex, corresponding to the early auditory response (Zouridakis et al., 1998), and bilateral activations on the medial temporal cortices (Figure 5.8), corresponding to late language processing (Breier et al., 1998; Frye et al., 2009). In the motor task, two neural activations on spatially closed cortical structures, i.e. the pre-bank and post-bank of the central sulcus, were well distinguished in the reconstruction results of VW-SSI, while other compared methods all fail to detect them (Figure 5.9).

In addition to the location and extent of epileptic sources, the concatenated cortical sources reveal dynamics of interical epileptic activities, which provide important information about epilepsy, such as propagation. The propagation to

neighboring areas (Figures 3.6, 3.10) has been reported previously (Rosenow and Lüders, 2001; Knowlton and Shih, 2004), and the possible reason is that brain tissues adjacent to lesions may have less pathological severity that remains invisible in MRI. Failure to remove MRI-invisible lesion can lead to persistent seizure after surgery (Hirabayashi et al., 1993). MEG sources and their dynamics can help identify such MRI-invisible but potential epileptogenic areas. Cross-hemisphere propagation within symmetric anatomic structures was observed in all patients, and two examples were shown for Patient 3: one with relatively slow speed (40 ms delay) (Figure 3.9) and another one with faster speed (10 ms delay) (Figure 3.10). These are consistent with cross-hemispheric propagations reported in another study (Bast et al., 2005). With combined spatial and temporal information for cortical sources, it is thus possible to distinguish primary sources (initiating epileptic activity) from secondary sources (due to propagation) in the identification of epileptogenic zones prior to surgical resection (Ding et al., 2007).

6.5 Limitations and Future Work

Although ℓ_1-norm regularization with transform sparseness has improved reconstruction accuracy for EEG/MEG sources, it is also worth noting that sparseness (or transform sparseness) only does not guarantee exact solutions for EEG/MEG inverse problems. Incoherence between basis functions for domains used to explore sparseness and basis functions for EEG/MEG measurement systems is also important (Donoho, 2006). The present results only suggest the benefit of using transform sparseness and the study of incoherent measurements that might further improve the performance of sparse source imaging techniques.

It is also noted that the present study in Chapters 4 and 5 only provides qualitative evaluation of the recovering accuracy in experimental data for W-SSI and VW-SSI. Moreover, while the comparison between MEG sources from V-SSI and MRI lesions is quantitative in terms of locations, it is still qualitative in terms of extents. Further quantitative evaluation would be needed in the future involving other independent measurements, such as fMRI (Sharon et al., 2007) or ECoG (Ding et al., 2007). More epilepsy patients are also needed to evaluate the feasibility of the sparse source imaging techniques in identification of epileptogenic zones. Furthermore, MEG has lower sensitivity to radial sources and thus estimated source extents might be biased due to missing radial components. Since EEG is sensitive to radial sources, estimation using combined MEG and EEG data is expected to have improved performance (Ding and Yuan, 2013a).

6.6 Conclusion

In summary, a sparse source imaging framework was proposed to solve the underdetermined EEG/MEG inverse problem by enforcing sparseness in one or multiple transform domains. Feasible transforms (variation transform and face-based wavelet transform) were designed to efficiently compress cortical activities on the highly irregular cortical surfaces and then implemented into ℓ_1-norm regularizations. The successful detection of irritative zones from interictal spikes activities using the variation based sparse cortical current density (V-SSI) technique demonstrated the capability of V-SSI in inferring extended cortical sources with not only the location but also the extent information. Reconstructions of consistent and reliable source dynamics of interictal spikes also provided valuable information about the development and evolvement of

epileptic activity. Simulation and experimental results from the face-based wavelet sparse source imaging (W-SSI) also indicated an improved reconstruction accuracy of source locations and extents. The sparse source imaging framework was also extended to use multiple transform sparseness simultaneously. The proposed variation and wavelet based sparse source imaging (VW-SSI) further improved the reconstruction accuracy with constrained global energy and provided more robustness through selection of wavelet levels and noise in simulations. Spatial resolution has also been improved by VW-SSI for noninvasive source imaging, illustrated by its ability to distinguish spatially nearby cortical sources evoked for auditory and language functions, while other source imaging methods fail to detect the phenomena. The sparse source imaging technique is promising to serve as a noninvasive tool in assisting pre-surgical planning for partial epilepsy patients.

References

10-20 system (EEG). In *Wikipedia*. Retrieved from http://en.wikipedia.org/wiki/10-20_system_(EEG)

Adde, G., Clerc, M., and Keriven, R. 2005. Imaging methods for MEG/EEG inverse Problem. *Int J Bioelectromag* 7: 111-114.

Adjouadi, M., Cabrerizo, M., Ayala, M., et al. 2005. Detection of interictal spikes and artifactual data through orthogonal transformations. *J Clin Neurophysiol* 22: 53-64.

Allison, T., McCarthy, G., Wood, C., Darcey, T., Spencer, D., and Williamson, P. 1989. Human cortical potentials evoked by stimulation of the median nerve. II. Cyto-architectonic areas generating short-latency activity. *J Neurophysiol* 62: 694-710.

Asano, E., Juhász, C., Shah, A., Sood, S., and Chugani, H.T. 2009. Role of subdural electrocorticography in prediction of long-term seizure outcome in epilepsy surgery. *Brain* 132:1038-1047.

Baillet, S., Mosher, J., and Leahy, R. 2001. Electromagnetic brain mapping. *IEEE Signal Proc Mag* 18: 14-30.

Baillet, S., and Garnero, L. 1997. A Bayesian Approach to Introducing Anatomo-Functional Priors in the EEG/MEG Inverse Problem. *IEEE T Bio-Med Eng* 44: 374-385.

Bast, T., Boppel, T., Rupp, A., et al. 2006. Noninvasive source localization of interictal EEG spikes: effects of signal-to-noise ratio and averaging. *J Clin Neurophysiol* 23: 487-497.

Bast, T., Ramantani, G., Boppel, T., et al. 2005. Source analysis of interictal spikes in polymicrogyria: Loss of relevant cortical fissures requires simultaneous EEG to avoid MEG misinterpretation. *NeuroImage* 25: 1232-1241.

Bautista, J.F., Foldvary-Schaefer, N., Bingaman, W.E., and Lüders, H.O. 2003. Focal cortical dysplasia and intractable epilepsy in adults: clinical, EEG, imaging, and surgical features. *Epilepsy Res* 55: 131-136.

Bonneau, G.P., Hahmann, S., and Nielson, G.M. 1996. BLaC-wavelets: a multiresolution analysis with non-nested spaces. *Visualization '96. Proceedings*: 43-48.

Boyd, S., and Vandenberghe, L. 2004. *Convex Optimization*. United Kingdom: Cambridge University Press.

Breier, J.I., Simos, P.G., Zouridakis, G., and Papanicolaou, A.C. 1998. Relative timing of neuronal activity in distinct temporal lobe areas during a recognition memory task for words. *J Clin Exp Neuropsychol* 20:782-790.

Brodbeck, V., Spinelli, L., Lascano, A., Wissmeier, M., Vargas, M., Vulliemoz, S., and

Pollo, C., et al. 2011. Electroencephalographic source imaging: a prospective study of 152 operated epileptic patients. Brain 134: 2887-2897.

Candès, E., and Romberg, J. 2007. Sparsity and incoherence in compressive sampling. *Inverse Probl* 23:969-985.

Candès, E., Romberg, J., and Tao, T. 2006. Stable signal recovery from incomplete and inaccurate measurements. *Commun Pur Appl Math* 59:1207-1223.

Chang, W., Nummenmaa, A., Hsieh, J., and Lin, F. 2010. Spatially sparse source cluster modeling by compressive neuromagnetic tomography. *NeuroImage* 53:146-160.

Chowdhury, R.A., Lina, J.M., Kobayashi, E., and Grova, C. 2013. MEG source localization of spatially extended generators of epileptic activity: comparing entropic and hierarchical Bayesian approaches. *PLoS One* 8: e55969.

Cohen, D. 1972. Magnetoencephalography: detection of the brain's electrical activity with a superconducting magnetometer. *Science* 175: 664-666.

Cohen, D., and Cuffin, B.N. 1983. Demonstration of useful differences between the magnetoencephalogram and electroencephalogram. *Electroencephalogr Clin Neurophysiol* 56: 38-51.

Cooper, R., Winter, A.L., Crow, H.J., and Walter, W.G. 1965. Comparison of subcortical, cortical and scalp activity using chronically indwelling electrodes in man. *Electroencephalogr and Clin Neurophysiol* 18:217-228.

Cottereau, B., Jerbi, K., and Baillet, S. 2007. Multiresolution imaging of MEG cortical sources using an explicit piecewise model. *NeuroImage* 38: 439-451.

Dale, A.M., and Sereno, M.I. 1993. Improved localization of cortical activity by combining EEG and MEG with MRI cortical surface reconstruction. *J Cogn Neurosci* 5: 162-176.

Dale, A.M., Fischl, B., and Sereno, M.I. 1999. Cortical surface-based analysis. *Neuroimage* 9: 179-194.

Darvas, F., Pantazis, D., Kucukaltun-Yildirim, E., and Leahy, R.M. 2004. Mapping human brain function with MEG and EEG: methods and validation. *NeuroImage* 23: S289-S299.

de Munck, J., Van Dijk, B., and Spekreijse, H. 1988. Mathematic dipoles are adequate to describe realistic generators of human brain activity. *IEEE T Biomed Eng* 35: 960-966.

Dhond, R.P., Buckner, R.L., Dale, A.M., Marinkovic, K., and Halgren, E. 2001. Spatiotemporal maps of brain activity underlying word generation and their modification during repetition priming. *J Neurosci* 21: 3564-3571.

Ding, L., and He, B. 2008. Sparse source imaging in electroencephalography with accurate field modeling. *Hum Brain Mapp* 29: 1053-1067.

Ding, L., and Yuan, H. 2013a. Simultaneous EEG and MEG source reconstruction in sparse electromagnetic source imaging. *Hum Brain Mapp* 34: 775-795.

Ding, L. 2009. Reconstructing cortical current density by exploring sparseness in the transform domain. *Phys in Med Biol* 54: 2683-2697.

Ding, L., Ni, Y., Sweeney, J., and He, B. 2011. Sparse cortical current density imaging in motor potentials induced by finger movement. *J Neural Eng* 8:036008.

Ding, L., Wilke, C., Xu, B., Xu, X., van Drongelene, W., Kohrman, M., and He, B. 2007. EEG source imaging: correlate source locations and extents with ECoG and surgical resections in epilepsy patients. *J Clin Neurophysiol* 24: 130-136.

Ding, L., Worrell, G.A., Lagerlund, T.D., and He B. 2006. 3D source localization of interictal spikes in epilepsy patients with MRI lesions. Phys Med Biol 51: 4047-4062.

Ding, L., Zhu, M., Liao, K. 2013b. Wavelet based sparse source imaging technique. *Conf Proc IEEE Eng Med Biol Soc* 2013: 5418-5421.

Donoho, D.L. 2006. Compressed Sensing. *IEEE Trans Inf Theory* 52: 1289-1306.

Doss, R.C., Zhang, W., Risse, G.L., and Dickens, D.L. 2009. Lateralizing language with magnetic source imaging: Validation based on the Wada test. *Epilepsia* 50:2242-2248.

Ebersole, J.S., and Hawes-Ebersole, S. 2007. Clinical application of dipole models in the localization of epileptiform activity. *J Clin Neurophysiol* 24: 120–129.

Ebersole, J.S. 1994. Non-invasive localization of the epileptogenic focus by EEG dipole modeling. *Acta Neurol Scand* 154: S20-S28.

Efron, B., and Tibshirani, R. 1993. An introduction to bootstrap. *Number 57 in Monographs on Statistics and Applied Probability*. Chapman and Hall/CRC.

Engel, J.J. 1993. Update on surgical treatment of the epilepsies. Neurology 43: 1612-1617.

Frye, R.E., Rezaie, R., and Papanicolaou, A.C. 2009. Functional neuroimaging of language using magnetoencephalography. *Phys Life Rev* 6: 1-10.

Fuchs, M., Wagner, M., and Kastner, J. 2001. Boundary element method volume conductor models for EEG source reconstruction. *Clin Neurophysiol* 112: 1400-1407.

Fuchs, M., Wagner, M., Köhler, T., and Wischmann, H.A. 1999. Linear and nonlinear current density reconstructions. *J Clin Neurophysiol* 16: 267-295.

Fuchs, M., Wagner, M., Wischmann, H.A., et al. 1998. Improving source

reconstructions by combining bioelectric and biomagnetic data. *Electroenceph Clin Neurophysiol* 107:93-111.

Gerloff, C., Uenishi, N., Nagamine, T., Kunieda, T., Hallett, M., and Shibasaki, H. 1998. Cortical activation during fast repetitive finger movements in humans: steady-state movement-related magnetic fields and their cortical generators. *Electroencephalogr Clin Neurophysiol* 109: 444-453.

Gorodnitsky, I.F., and Rao, B.D. 1997. Sparse signal reconstruction from limited data using FOCUSS: a re-weighted minimum norm algorithm. *IEEE T Signal Proces* 45: 600-615.

Gramfort, A., Papadopoulo, T., Baillet, S., and Clerc, M. 2011. Tracking cortical activity from M/EEG using graph cuts with spatiotemporal constraints. *NeuroImage* 54: 1930-1941.

Grech, R., Cassar, T., Muscat, J., et al. 2008. Review on solving the inverse problem in EEG source analysis. *J Neuroeng Rehabil* 5: 25.

Grova, C., Daunizeau, J., Lina, J.M., Bénar, C.G., Benali, H., and Gotman, J. 2006. Evaluation of EEG localization methods using realistic simulations of interictal spikes. *Neuroimage* 29:734-753.

Haas, L.F. 2003. Hans Berger (1873-1941), Richard Caton (1842-1926), and electroencephalography. *J Neurol Neurosur Ps* 74: 9.

Hämäläinen, M.S., and Ilmoniemi, R.J. 1994. Interpreting measured magnetic fields of the brain: minimum norm estimates. *Med Biol Eng Comput* 32: 35-42.

Hämäläinen, M.S., and Sarvas, J. 1989. Realistic conductivity geometry model of the human head for interpretation of neuromagnetic data. *IEEE Trans Biomed Eng* 36: 165-171.

Hämäläinen, M.S., Hari, R., llmoniemi, R.J., Knuutila, J., and Lounasmaa, O.V. 1993. Magnetoencephalography - theory, instrumentation, and applications to noninvasive studies of the working human brain. *Rev Mod Phys* 65: 413-497.

Han, J., Kim, J.S., Chung, C.K., and Park, K.S. 2007. Evaluation of smoothing in an iterative l p -norm minimization algorithm for surface-based source localization of MEG. *Phys Med Biol* 52:4791.

Haufe, S., Nikulin, V.V., Ziehe, A., Müller, K.R., and Nolte, G. 2008. Combining sparsity and rotational invariance in EEG/MEG source reconstruction. *NeuroImage* 42: 726-738.

He, B., Wang, Y., and Wu, D. 1999. Estimating cortical potentials from scalp EEG's in a realistically shaped inhomogeneous head model by means of the boundary element method. *IEEE T Biomed Eng* 46:1264-1268.

Hebiri, M., and van de Geer, S. 2011. The Smooth-Lasso and other ℓ1+ℓ2-penalized methods. *Electron J Statist* 5: 1184-1226.

Hillyard, S. 1993. Electrical and magnetic brain recordings: contributions to cognitive neuroscience. *Curr Opin Neurobiol* 3: 217-224.

Hirabayashi, S., Binnie, C.D., Janota, I., and Polkey, C.E. 1993. Surgical treatment of epilepsy due to cortical dysplasia: clinical and EEG findings. *J Neurol Neurosurg Psychiatry* 56: 765-770.

Hoerl, A.E., and Kennard, R.W. 1970. Ridge regression: biased estimation for nonorthogonal problems. *Technometrics* 12:55-67.

Huang, M.X., Dale, A.M., Song T., et al. 2006. Vector-based spatial-temporal minimum ℓ1-norm solution for MEG. *Neuroimage* 31: 1025-1037.

Iaizzo, P.A. 2013. Introduction to Neurophysiology. In He, B. (Ed.). *Neural Engineering*, Springer, 1-86.

Jäncke, L., Loose, R., Lutz, K., Specht, K. and Shah, N.J. 2000. Cortical activations during paced finger-tapping applying visual and auditory pacing stimuli. *Cogn Brain Res* 10: 51-66.

Jerbi, K., Baillet, S., Mosher, J.C., Nolte, G., Garnero, L., and Leahy, R.M. 2004. Localization of realistic cortical activity in MEG using current multipoles. *NeuroImage* 22: 779-793.

Kaiboriboon, K., Nagarajan, S., Mantle, M., and Kirsch, H.E. 2010. Interical MEG/MSI in intractable mesial temporal lobe epilepsy: Spike yield and characterization. *Clin Neurophysiol* 121: 325-331.

Knowlton, R.C., and Shih, J. 2004. Magnetoencephalography in epilepsy. *Epilepsia* 45: 61-71.

Kobayashi, K., Yoshinaga, H., Ohtsuka, Y., and Gotman. J. 2005. Dipole modeling of epileptic spikes can be accurate or misleading. *Epilepsia* 46:397-408.

Kuruvilla, A., and Flink, R. 2003. Intraoperative electrocorticography in epilepsy surgery: useful or not? *Seizure* 12: 577-584.

Lai, Y., van Drongelen, W., Ding, L., Hecox, K.E., Towle, V.L., Frim, D.M., and He, B. 2005. Estimation of in vivo human brain-to-skull conductivity ratio from simultaneous extra- and intra-cranial electrical potential recordings. *Clin Neurophysiol* 116: 456-465.

Landau, W.M., Kleffner, R. 1957. Syndrome of acquired aphasia with convulsive disorder in children. *Neurology* 7: 520-530.

Liao, K., Zhu, M., Ding, L., Valette, S., Zhang, W., and Dickens, D. 2012. Sparse representation of cortical current density maps using wavelets. *Phys Med Biol* 57: 6881-6901.

Lobo, M.S., Vandenberghe L., Boyd S., and Lebret H. 1998. Applications of second-order cone programming. *Linear Algebra Appl* 284: 193-228.

Mallat, S. 2009. *A wavelet tour of signal processing: the sparse way*. Burlinton, MA: Academic Press.

Malmivuo, J., and Plonsey, R., 1995. *Bioelectromagnetism: Principles and applciations of bioelectric and biomagnetic fields*. New York, NY: Oxford University Press.

Matsuura, K., and Okabe, Y. 1995. Selective minimum-norm solution of the biomagnetic inverse problem. *IEEE Trans Biomed Eng* 42: 608-615.

Merlet, I., and Gotman, J. 1999. Reliability of dipole models of epileptic spikes. *Clin Neurophysiol* 110: 1013-1028.

Metz, C.E., Goodenough D.J., and Rossmann K. 1973. Evaluation of Receiver Operating Characteristic Curve Data in Terms of Information Theory, with Applications in Radiography. *Radiology* 109: 297-303.

Molins, A., Stufflebeam, S.M., Brown, E.N., and Hämäläinen, M.S. 2008. Quantification of the benefit from integrating MEG and EEG data in minimum $\ell 2$-norm estimation. *NeuroImage* 42:1069-1077.

Morozov, A.V. 1966. On the solution of functional equations by the method of regularization. *Sov Math Dokl* 7: 414-417.

Mosher, J.C., Leahy, R.M., and Lewis, P.S. 1999. EEG and MEG: Forward solutions for inverse methods. *IEEE Trans Biomed Eng* 46: 245-259.

Nesterov, Y., and Nemirovski, A. 1994. *Interior-point polynomial algorithms in convex programming*. SIAM studies in applied mathematics.

Nunez, P.L. 1981. *Electric field of the brain*. London: Oxford University Press.

Oishi, M., Otsubo, H., Kameyama, S., Morota, N., Masuda, H., Kitayama, M., and Tanaka, R. 2002. Epileptic spikes: magnetoencephalography versus simultaneous electrocorticography. *Epilepsia* 43: 1390-1395.

Ou, W., Hämäläinen, M.S., and Golland, P. 2009. A distributed spatio-temporal EEG/MEG inverse solver. *NeuroImage* 44: 932-946.

Paetau, R., Granstrom, M.L., Blomstedt, G., Jousmaki, V., Korkman, M., Liukkonen, E. 1999. Magnetoencephalography in presurgical evaluation of children with the Landau-Kleffner syndrome. *Epilepsia* 40: 326-335.

Papanicolaou, A.C., Simos, P.G., Castillo, E.M., Breier, J.I., Sarkari, S., Pataraia, E., Billingsley, R.L., et al. 2004. Magnetoencephalography: a noninvasive alternative to the Wada procedure. *J Neurosurg* 100: 867-876.

Pascual-Marqui, R.D. 1999. Review of methods for solving the EEG inverse problem. *Int J Bioelectromagn* 1: 75-86.

Pascual-Marqui, R.D., Michel, C.M., and Lehmann, D. 1994. Low resolution electromagnetic tomography: a new method for localizing electrical activity in the brain. *Int J Psychophysiol* 18:49-65.

Petrov, Y. 2012. Harmony: EEG/MEG linear inverse source reconstruction in the anatomical basis of spherical harmonics. *PLoS One* 7: e44439.

Phillips, C., Rugg, M.D., and Friston, K.J. 2002. Anatomically Informed Basis Functions for EEG Source Localization: Combining Functional and Anatomical Constraints. *NeuroImage* 16: 678-695.

Plummer, C., Harvey, A., and Cook, M. 2008. EEG source localization in focal epilepsy: Where are we now? *Epilepsia* 49: 201-218.

Pollok, B., Müller, K., Aschersleben, G., Schmitz, F., Schnitzler, A., and Prinz, W. 2003. Cortical activations associated with auditorily paced finger tapping. *Neuroreport* 14: 247-250.

Ramon, C., Schimpf, P.H., Haueisen, J. 2006. Influence of head models on EEG simulations and inverse source localizations. *Biomed Eng Online* 5: 10-23.

Rosenow, F., and Lüders, H. 2001. Presurgical evaluation of epilepsy. *Brain* 124: 1683-1700.

Rotenberg, J., and Pearl, P.L. 2003. Landau–Kleffner syndrome. *Arch Neurol* 60: 1019-1021.

Schröder, P., and Sweldens, W. 1995. Spherical wavelets: Efficiently representing functions on the sphere. *Computer Graphics Proceedings* 161-172.

Sharon, D., Hämäläinen, M., Tootell, R., Halgren, E., and Belliveau, J. 2007. The advantage of combining MEG and EEG: comparison to fMRI in focally-stimulated visual cortex. *NeuroImage* 36: 1225-1235.

Sharbrough, F., Chatrian, G-E, Lesser, R.P., Lüders, H., Nuwer, M., and Picton, T.W. 1991. American Electroencephalographic Society Guidelines for Standard Electrode Position Nomenclature. *J* Clin Neurophysiol 8: 200-202.

Shattuck, D.W., and Leahy, R.M. 2002. Brainsuite: an automated cortical surface identification tool. *Med Image Anal* 8: 129-142.

Silva, C., Maltez, J.C., Trindate, E., Arriaga, A., and Ducla-Soares, E. 2004. Evaluation of L1 and L2 minimum norm performances on EEG localizations. *Clin Neurophysiol* 115: 1657-1668.

Spencer, S., and Huh, L. 2008. Outcomes of epilepsy surgery in adults and children. Lancet Neurol 7: 525-537.

Stefan, H., Hummel, C., Scheler, G., et al. 2003. Magnetic brain source imaging of focal epileptic activity: a synopsis of 455 cases. *Brain* 126: 2396-2405.

Sturm, J.F. 1999. Using SeDuMi 1.02, a Matlab toolbox for optimization over symmetric cones. *Optim Meth Softw* 11: 625-653.

Tanaka, N., Cole, A.J., von Pechmann, D., et al. 2009. Dynamic statistical parametric mapping for analyzing ictal magnetoencephalographic spikes in patients with intractable frontal lobe epilepsy. *Epilepsy Res* 85: 279-286.

Tao, J.X., Ray, A., Hawes-Ebersole, S., Ebersole, J.S. 2005. Intracranial EEG substrates of scalp EEG interictal spikes. *Epilepsia* 46: 669–676.

Tibshirani, R. 1996. Regression shrinkage and selection via the Lasso. *J R Stat Soc Series B Stat Methodol* 58: 267-288.

Tibshirani, R., Saunders, M., Rosset, S., Zhu, J., and Knight, K. 2005. Sparsity and smoothness via the fused lasso. *J R Stat Soc Series B Stat Methodol* 67: 91-108.

Trujillo-Barreto, N.J., Aubert-Vázquez, E., and Penny, W.D. 2008. Bayesian M/EEG source reconstruction with spatio-temporal priors. *NeuroImage* 39: 318-335.

Uutela, K., Hämäläinen, M.S., and Somersalo, E. 1999. Visualization of magnetoencephalographic data using minimum current estimates. *Neuroimage* 3S: 168.

Valette, S., and Prost, R. 2004. Wavelet-based progressive compression scheme for triangle meshes: wavemesh. *IEEE T Vis Comput Graph* 10: 123-129.

Vallaghè, S., and Clerc, M. 2009. A global sensitivity analysis of three- and four-layer EEG conductivity models. *IEEE T Bio-Med Eng* 56: 988-995.

van den Broek, S., Reinders, F., Donderwinkel, M., and Peters, M. 1998. Volume conduction effects in EEG and MEG. *Electroencephalogr Clin Neurophysiol* 106: 522-534.

Vega-Hernández, M., Martinez-Montes, E., Sanches-Bornot, J.M., Lage-Castellanos, A., and Valdes-Sosa, P.A. 2008. Penalized least squares methods for solving the EEG inverse problem. *Stat Sin*18: 1535-1551.

Wiebe, S., Blume, W.T., Girvin, J.P., and Eliasziw, M. 2001. A Randomized, Controlled Trial of Surgery for Temporal-Lobe Epilepsy. *New Engl J Med* 345: 311-

318.

Wipf, D., and Nagarajan, S. 2009. A unified Bayesian framework for MEG/EEG source imaging. *Neuroimage* 44: 947-966.

World Health Organization. 2012. Epilepsy fact sheets. Retrieved from http://www.who.int/mediacentre/factsheets/fs999/en/index.html

Wolters, C.H. 2007. The finite element method in EEG/MEG source analysis. *SIAM News*. Retrieved from http://www.mathaware.org/mam/07/FEM.pdf

Wood, C.C. 1982. Application of dipole localization methods to source identification of human evoked potentials. *Ann N Y Acad Sci* 388:139-155.

Xu P, Tian Y, Chen H, Yao D. Lp Norm Iterative Sparse Solution for EEG Source Localization. Biomedical Engineering, IEEE Transactions on 2007;54:400-409.

Zhu, M., Zhang, W., Dickens, D.L., and Ding, L. 2013a. Wavelet-based sparse source imaging in localizing epileptic source for partial epilepsy," International IEEE/EMBS Conference on Neural Engineering (NER), 2013.

Zhu, M., Zhang, W., Dickens, D.L., and Ding, L. 2013b. Reconstructing spatially extended brain sources via enforcing multiple transform sparseness. *NeuroImage*, in press.

Zhu, M., Zhang, W., Dickens, D.L., King, J.A., and Ding, L. 2013c. Sparse MEG source imaging for reconstructing dynamic sources of interictal spikes in partial epilepsy. *J Clin Neurophysiol* 30: 313-328.

Zou, H., and Hastie, T. 2005. Regularization and variable selection via the elastic net. *J R Stat Soc Series B Stat Methodol* 67: 301-320.

Zouridakis, G., Simos, P.G., and Papanicolaou, A.C. 1998. Multiple bilaterally asymmetric cortical sources account for the auditory N1m component. *Brain Topogr* 10: 183-189.

Appendix A: Analysis Matrices for Face-based Wavelets

Let T_i^m denote a set of triangles on the mesh at the finer level *m* that merge to the j^{th} triangle at the coarser level *m+1*. Each entry a_{ji}^m in the analysis matrix A^m is computed as the proportion of triangular area of intersection between T_j^{m+1} and T_i^m to the area of T_j^{m+1}:

$$a_{ji}^m = \frac{area(T_j^{m+1} \bigcap T_i^m)}{area(T_j^{m+1})}, \tag{A.1}$$

The analysis matrix B^m is designed to have the property of semi-orthogonality in basis functions (Bonneau et al., 1996) and is obtained by solving the following set of equations (see details in Liao et al., 2012):

$$\begin{cases} A^m (G^m)^{-1} (B^m)^T = \mathbf{0}, \\ B^m (G^m)^{-1} (B^m)^T = \mathbf{I}. \end{cases} \tag{A.2}$$

where G^m is the Gram-Schmidt matrix, i.e. a diagonal matrix with its diagonal elements being areas of triangles at level *m*.

Appendix B: Evaluation Metrics

The AUC metric is derived from ROC analysis, which is a graphic plot of the true positive rate (TPR) against false positive rate (FPR) at various values of the threshold α. This may be expressed as

$$TPR(\alpha) = TP(\alpha) / (TP(\alpha) + FN(\alpha)) ; FPR(\alpha) = FP(\alpha) / (TN(\alpha) + FP(\alpha)), \quad \text{(B.1)}$$

where $TP(\alpha)$ and $FP(\alpha)$ are the numbers of active elements in estimations inside or outside simulated source patches. $FN(\alpha)$ and $TN(\alpha)$ are the numbers of inactive elements inside or outside simulated source patches. To reduce bias in estimating AUC because of unbalanced numbers of active (~100) and inactive elements (~10^4) in EEG/MEG inverse problems, a procedure (Grova et al., 2006), which randomly samples (50 times) inactive elements to the same number as active elements from both close fields and far fields of simulated sources, is used.

The SD metric (Molins et al., 2008; Chang et al., 2010) is defined as

$$SD = \sqrt{\frac{\sum_{k=1}^{N}\sum_{i\in I_k} d_{ki}^2 \left\|\hat{s}_i\right\|_2^2}{\sum_{i=1}^{n}\left\|\hat{s}_i\right\|_2^2}}, I_k = \left\{ i \mid k = \arg\min_{k'}\{d_{k'i}\}\right\}, 1 \le i \le n, 1 \le k \le N, 1 \le k' \le N, \quad \text{(B.2)}$$

where $\hat{s}_i$ is the amplitude of *i*th dipole in the estimated current density and d_{ki} defines the distance from the *k*th dipole inside the simulated current density (consisting of multiple simulated patch sources) to the *i*th dipole in the estimated current density. I_k is the index set of dipoles in the estimated current density, which are spatially closest to the *k*th dipole in the simulated current density. *N* and n denote the number of dipoles in the simulated current density and the number of dipoles in the estimated current density,

respectively.

The DLE metric (Molins et al., 2008; Chang et al., 2010) is defined as the average distance between the location of each dipole (*k*th) in the simulated current density to the maxima of its closest dipoles (from I_k) in the estimated current density:

$$DLE = \frac{1}{N_J}\sum_{k\in J} DLE_k\ ,\quad J = \left\{k \mid I_k \notin \varnothing\right\},\quad DLE_k = \left\{d_{ki} \mid i = \arg\max_{i'}(\left\|\hat{s}_{i'}\right\|_2), i' \in I_k\right\} \qquad \text{(B.3)}$$

where N_J is the number of elements in set *J*. The definitions of *i*, *k*, I_k and $\hat{s}_i$ are same as in equation (B.1).

The relative mean square error (RMSE) (Grova et al., 2006) is defined as

$$RMSE = \frac{\sum_{i=1}^{N}\left\|\hat{s}_i - s_i\right\|_2^2}{\sum_{i=1}^{N}\left\|s_i\right\|_2^2}, \qquad \text{(B.4)}$$

where s_i is the amplitude of *i*th dipole in simulated sources.

SPRINGER LICENSE
TERMS AND CONDITIONS

Dec 09, 2013

This is a License Agreement between Min Zhu ("You") and Springer ("Springer") provided by Copyright Clearance Center ("CCC"). The license consists of your order details, the terms and conditions provided by Springer, and the payment terms and conditions.

All payments must be made in full to CCC. For payment instructions, please see information listed at the bottom of this form.

License Number 3284630813341
License date Dec 09, 2013
Licensed content publisher Springer
Licensed content publication Springer eBook
Licensed content title Introduction to Neurophysiology
Licensed content author Paul A. Iaizzo
Licensed content date Jan 1, 2013
Type of Use Thesis/Dissertation
Portion Figures
Author of this Springer article No
Order reference number 120
Title of your thesis / dissertation
EEG/MEG sparse source imaging and its application in epilepsy
Expected completion date Dec 2013
Estimated size(pages) 130
Total 0.00 USD
Terms and Conditions

Introduction

The publisher for this copyrighted material is Springer Science + Business Media. By clicking "accept" in connection with completing this licensing transaction, you agree that the following terms and conditions apply to this transaction (along with the Billing and Payment terms and conditions established by Copyright Clearance Center, Inc. ("CCC"), at the time that you opened your Rightslink account and that are available at any time at http://myaccount.copyright.com).

Limited License

With reference to your request to reprint in your thesis material on which Springer Science and Business Media control the copyright, permission is granted, free of charge, for the use indicated in your enquiry.

Licenses are for one-time use only with a maximum distribution equal to the number that you identified in the licensing process.

This License includes use in an electronic form, provided its password protected or on the university’s intranet or repository, including UMI (according to the definition at the Sherpa website: http://www.sherpa.ac.uk/romeo/). For any other electronic use, please contact Springer at

(permissions.dordrecht@springer.com or
permissions.heidelberg@springer.com).

The material can only be used for the purpose of defending your thesis, and with a maximum of 100 extra copies in paper.

Although Springer holds copyright to the material and is entitled to negotiate on rights, this license is only valid, subject to a courtesy information to the author (address is given with the article/chapter) and provided it concerns original material which does not carry references to other sources (if material in question appears with credit to another source, authorization from that source is required as well).

Permission free of charge on this occasion does not prejudice any rights we might have to charge for reproduction of our copyrighted material in the future.

Altering/Modifying Material: Not Permitted
You may not alter or modify the material in any manner. Abbreviations, additions, deletions and/or any other alterations shall be made only with prior written authorization of the author(s) and/or Springer Science + Business Media. (Please contact Springer at (permissions.dordrecht@springer.com or permissions.heidelberg@springer.com)

Reservation of Rights
Springer Science + Business Media reserves all rights not specifically granted in the combination of (i) the license details provided by you and accepted in the course of this licensing transaction, (ii) these terms and conditions and (iii) CCC's Billing and Payment terms and conditions.

Copyright Notice:Disclaimer
You must include the following copyright and permission notice in connection with any reproduction of the licensed material: "Springer and the original publisher /journal title, volume, year of publication, page, chapter/article title, name(s) of author(s), figure number (s), original copyright notice) is given to the publication in which the material was originally published, by adding; with kind permission from Springer Science and Business Media"

Warranties: None

Example 1: Springer Science + Business Media makes no representations or warranties with respect to the licensed material.

Example 2: Springer Science + Business Media makes no representations or warranties with respect to the licensed material and adopts on its own behalf the limitations and disclaimers established by CCC on its behalf in its Billing and Payment terms and conditions for this licensing transaction.

Indemnity
You hereby indemnify and agree to hold harmless Springer Science + Business Media and CCC, and their respective officers, directors, employees and agents, from and against any and all claims arising out of your use of the licensed material other than as specifically authorized pursuant to this license.

No Transfer of License
This license is personal to you and may not be sublicensed, assigned, or transferred by you to any other person without Springer Science + Business Media's written permission.

No Amendment Except in Writing
This license may not be amended except in a writing signed by both parties (or, in the case of Springer Science + Business Media, by CCC on Springer Science + Business Media's behalf).

Objection to Contrary Terms
Springer Science + Business Media hereby objects to any terms contained in any purchase order, acknowledgment, check endorsement or other writing prepared by you, which terms are inconsistent with these terms and conditions or CCC's Billing and Payment terms and conditions. These terms and conditions, together with CCC's Billing and Payment terms and conditions (which are incorporated herein), comprise the entire agreement between you and Springer Science + Business Media (and CCC) concerning this licensing transaction. In the event of any conflict between your obligations established by these terms and conditions and those established by CCC's Billing and Payment terms and conditions, these terms and conditions shall control.

Jurisdiction
All disputes that may arise in connection with this present License, or the breach thereof, shall be settled exclusively by arbitration, to be held in The Netherlands, in accordance with Dutch law, and to be conducted under the Rules of the 'Netherlands Arbitrage Instituut' (Netherlands Institute of Arbitration).***OR:***

All disputes that may arise in connection with this present License, or the breach thereof, shall be settled exclusively by arbitration, to be held in the Federal Republic of Germany, in accordance with German law.

Other terms and conditions:

v1.3

If you would like to pay for this license now, please remit this license along with your payment made payable to "COPYRIGHT CLEARANCE CENTER" otherwise you will be invoiced within 48 hours of the license date. Payment should be in the form of a check or money order referencing your account number and this invoice number RLNK501177378.
Once you receive your invoice for this order, you may pay your invoice by credit card.

Please follow instructions provided at that time.
Make Payment To:
Copyright Clearance Center
Dept 001
P.O. Box 843006
Boston, MA 02284-3006

For suggestions or comments regarding this order, contact RightsLink Customer Support: customercare@copyright.com or +1-877-622-5543 (toll free in the US) or +1-978-646-2777.

Gratis licenses (referencing $0 in the Total field) are free. Please retain this printable license for your reference. No payment is required.